

A076065

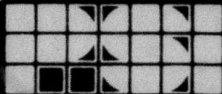
PSI TR-108

12

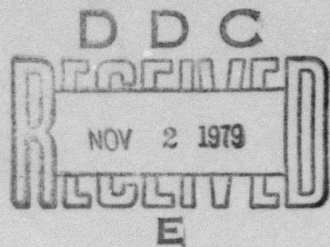
PULSED LASER PROPULSION

LEVEL FINAL REPORT

P.E. Nebolsine, A.N. Pirri, J.S. Goela and G.A. Simons



February 1978



Prepared for

DEFENSE ADVANCED RESEARCH PROJECTS AGENCY

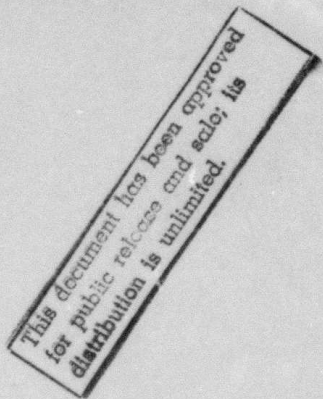
Arlington, VA 22209
ARPA Order 3176

DDC FILE COPY

Monitored by

OFFICE OF NAVAL RESEARCH

Department of the Navy
Arlington, VA 22217
Contract No. N00014-76-C-0738



The views and conclusions contained in this document are those of the authors and should not be interpreted as necessarily representing the official policies, either expressed or implied, of the Defense Advanced Research Projects Agency or the U.S. Government.

PHYSICAL SCIENCES INC.

30 COMMERCE WAY, WOBURN, MASS. 01801

79 11 02 055

UNCLASSIFIED

SECURITY CLASSIFICATION OF THIS PAGE (When Data Entered)

DD FORM 1473 JAN 73 EDITION OF 1 NOV 68 IS OBSOLETE

UNCLASSIFIED

~~SECURITY CLASSIFICATION OF THIS PAGE (When Data Entered)~~

UNCLASSIFIED

SECURITY CLASSIFICATION OF THIS PAGE(When Data Entered)

The model predicts laser parameters necessary to achieve high specific impulses, i.e., 600 to 1000 sec. Scaling laws for high thrust - high specific impulse rocket systems are discussed.

Experiments using pulsed CO₂ TEA lasers were performed with conical and parabolic nozzles. At one atmospheric background pressure a maximum specific impulse of 900 ± 400 sec was obtained with an energy conversion efficiency (exhaust energy/laser energy of) $\sim 50\%$. At 10^{-4} atmospheric background pressure, a specific impulse of 500 ± 100 sec. was obtained with a self-focusing parabolic nozzle.

UNCLASSIFIED

SECURITY CLASSIFICATION OF THIS PAGE(When Data Entered)

FOREWORD

ARPA Order No.: 3176

Contract No.: N00014-76-C-0738

Principal Investigator: A. N. Pirri and P. E. Nebolsine
and Phone No.: (617) 933-8500

Name of Contractor: Physical Sciences Inc.

Effective Date of Contract: March 1, 1976

Contract Expiration Date: September 30, 1977

Amount of Contract: \$199,969.00

Scientific Officer: Albert D. Wood
c/o Physical Sciences Division
Office of Naval Research
800 N. Quincy Street
Arlington, Virginia 22217

Short Title of Work: Pulsed Laser Propulsion

Accession For	
NTIS GRA&I	<input checked="" type="checkbox"/>
DDC TAB	<input type="checkbox"/>
Unannounced	<input type="checkbox"/>
Justification _____	
By _____	
Distribution/ _____	
Availability Codes _____	
Dist	Avail and/or special
A	

ACKNOWLEDGEMENT

**The authors would like to acknowledge Edward McCracken and
Henry Murphy for their assistance in performing the experiments.**

ABSTRACT

A fluid mechanical model is developed to assess the performance in both finite background pressure and vacuum environments of a rocket that is propelled by the absorption of radiant energy from a remotely stationed, repetitively pulsed laser. The model describes the gaseous propellant flow within a conical nozzle that is subjected to a series of point energy depositions at the apex of the cone. An equivalence between conical and parabolic nozzles is discussed for finite background pressure operation. The model specifies laser parameters necessary to achieve high specific impulses, i.e., 600 to 1000 sec. Scaling laws for high thrust - high specific impulse rocket systems are discussed.

Experiments using pulsed CO₂ TEA lasers were performed with conical and parabolic nozzles. At one atmospheric background pressure, a maximum specific impulse of 900 ± 400 sec was obtained with an energy conversion efficiency (exhaust energy/laser of energy) ~ 50%. At 10⁻⁴ atmospheric background pressure, a specific impulse of 500 ± 100 sec was obtained with a self-focusing parabolic nozzle.

TABLE OF CONTENTS

<u>Section</u>		<u>Page</u>
	ABSTRACT	iii
1.	INTRODUCTION	1
2.	THEORETICAL UPDATE	7
	2. 1 Review of Model for Vacuum Operation	7
	2. 2 Finite Back Pressure Operation	11
	2. 3 Equivalence Between Conical and Parabolic Nozzles at Finite p_∞	17
3.	EXPERIMENT DESIGN AND ASSEMBLY	21
	3. 1 Nozzle Design	21
	3. 1. 1 Conical Nozzle	21
	3. 1. 2 Parabolic Nozzle	21
	3. 2 Plenum Chamber Design	24
	3. 3 Diaphragm Design and Operation	28
	3. 4 Optical Train	30
	3. 5 Laser System and Delay Generator	33
	3. 6 Vacuum Chamber	36
4.	EXPERIMENTAL RESULTS	39
	4. 1 Propellant Flow Through the Nozzle	39
	4. 2 Conical Nozzle Experiments	40

TABLE OF CONTENTS
(Cont.)

<u>Section</u>		<u>Page</u>
	4. 3 Parabolic Nozzle Experiments	48
	4. 3. 1 Parabolic Experiments at One Atmosphere	48
	4. 3. 2 Parabolic Experiments at 1/5 Atmosphere	51
	4. 3. 3 Parabolic Experiments at 10^{-4} Atmosphere	53
	4. 4 Pressure Transducer Data Interpretation	61
5.	SCALING LAWS FOR EXPERIMENTS AT INCREASED LASER ENERGY	71
	5. 1 Laser Energy and REP Rate Requirements	71
	5. 2 Pulse Length Requirements	76
6.	SUMMARY AND CONCLUSIONS	83
	REFERENCES	85
	APPENDIX	89

LIST OF ILLUSTRATIONS

<u>Figure</u>		<u>Page</u>
1. 1a	Single Pulse Propulsion Concept as Introduced in Ref. 4.	4
1. 1b	Multiple Pulse Propulsion Concept and Equivalent Conical Nozzle.	4
2. 1	Schematic of Repetitively Pulsed Laser Powered Thruster Concept.	8
2. 2	Laser Energy Requirements: Vacuum Operation.	9
2. 3	Laser Energy Requirements.	10
2. 4	Conical Nozzle - Prepulse Propellant Flow at Finite Back Pressure.	12
2. 5	Parabolic Nozzle Equivalent to Conical Nozzle.	18
3. 1	Schematic of Conical Nozzle and Plenum Assembly.	23
3. 2	Parabolic Nozzle.	25
3. 3	Location of Shock Catcher.	27
3. 4	Schematic for Measuring Diaphragm Opening Time.	31
3. 5	Oscilloscope Trace.	32
3. 6	Trace of Pyroelectric Detector Output.	35
4. 1	Experimental Schematic, Conical Nozzle, $P_{\infty} = 1 \text{ atm.}$	42
4. 2	Pendulum Movement, Impulse and Coupling Coefficient Data.	44

LIST OF ILLUSTRATIONS
(Cont.)

<u>Figure</u>		<u>Page</u>
4. 3	Two Pulse Data with Conical Nozzle - One Atmosphere Background Pressure.	46
4. 4	Impulse Histogram.	50
4. 5	Impulse Data Histogram.	52
4. 6a	Representative Pressure Transducer Trace.	54
4. 6b	Representative Pressure Transducer Trace.	54
4. 7	Oscilloscope Trace.	56
4. 8	I_{sp} vs. Background Pressure with Parabolic Nozzle.	60
4. 9	Oscilloscope Trace.	62
4. 10	Deduced Blast Wave Energy.	67
4. 11	Deduced Helium Density.	68
4. 12	Deduced Gas Velocity.	69
5. 1	Laser Energy Requirements - 1 atm Operation.	72
5. 2	Laser Energy Requirements - 10^{-1} atm Operation.	73
5. 3	Laser Energy Requirements - 10^{-2} atm Operation.	74
5. 4	Laser Energy Requirements - Vacuum Operation.	75
5. 5	"Universal" Design - Sea Level to Vacuum.	77

LIST OF ILLUSTRATIONS
(Cont.)

<u>Figure</u>		<u>Page</u>
5. 6	Required Pulse Duration @ 1 atm.	78
5. 7	Design for 1 KJ Operation @ 1 atm.	80
5. 8	Design for 10 KJ Operation @ 1 atm.	81
A. 1	Double Spark Velocity Diagnostic.	90
A. 2	Perpendicular Electrode Configuration.	92
A. 3	Electronic Schematic for Triggering Spark Gap.	94
A. 4	Electronic Schematic for Switching Voltage on Gap.	95
A. 5	x - t Diagram for Single Pulse in He.	98
A. 6	The Particle Velocity Distributions Behind Spherical Blast Wave of Various Shock Strengths η , $\gamma = 1.4$.	103
A. 7	Open Shutter.	106
A. 8	Oscilloscope Trace.	108
A. 9	x - t Diagram for Single Pulse in Air.	109

1. INTRODUCTION

In recent years several authors¹⁻¹⁰ have discussed and analyzed the possibility of beamed laser energy for rocket propulsion, often with specific reference to the application of high power, ground-based lasers. The concept is deceptively simple: provide a high energy density for propulsion without the encumbrance of a massive on-board power supply by absorbing radiation from a remotely stationed high-power laser. Since the radiation absorbing propellant may be high temperature plasma, the specific impulse can be very large, i.e., > 1000 sec. The achievable thrust is limited by the available laser power, and with a remote energy source, larger payload/vehicle weight ratios are possible compared to chemical propulsion rockets.

The multiple pulsed laser rocket propulsion experiments described in this report are an outgrowth of single pulse and CW experiments. These past experiments, described in Ref. 4, measured the specific impulse and thrust/laser power that was obtained with existing laser systems. Steady-state simulation experiments were performed in a vacuum chamber with solid propellants, and pulsed laser propulsion along with the laser-powered pulse jet concept was introduced.⁴ A steady-state or CW laser propulsion system is a system whose thrust remains constant in time while the laser beam continuously provides the energy source for converting propellant mass to exhaust kinetic energy. It was found in Ref. 4 that a high ratio of thrust to laser power can be obtained by simply using the laser to vaporize a solid surface. However, in order to obtain high specific impulse it is necessary to add energy to the vapor in a stable manner. The heating of a gas by external radiation downstream of a nozzle throat was found to be inherently unstable when the gas is initially

weakly ionized and absorbs radiation via inverse Bremsstrahlung. The stability of laser-heated flows both upstream and downstream of a nozzle throat is not adequately understood and is a very complex issue.⁷ However, it appears that stable heating of a propellant in a steady-state manner may best be accomplished by heating the gas upstream of a throat such that the beam direction and the propellant flow direction are the same.⁷ This would require a laser window in the absorption chamber that will tolerate transmission of significant laser intensities along with high pressures for long periods of time.

The alternative approach to CW laser propulsion that circumvents the stability problem is to utilize a pulsed laser as described in this report and our previous theoretical study.⁸ The techniques for obtaining large thrust and specific impulse with a pulsed laser are an outgrowth of various experimental and theoretical problems in laser effects.¹¹⁻¹⁵ When a high power pulsed laser is focused to a high irradiance in a gas or on a solid surface, a high temperature, high pressure plasma, which propagates up the laser beam, is initiated. Provided the pulse is sufficiently short that the high pressure gas remains in the vicinity of a surface or nozzle wall, this method is an efficient propulsion mechanism. The propulsion system operates in a way similar to detonation propulsion systems that have been proposed for use in high pressure environments.¹⁶⁻²⁰ Periodic "explosions" in the nozzle transfer the detonation or laser energy to the working fluid. The two most significant potential advantages afforded by a pulsed laser propulsion system over a CW laser propulsion system are: 1) simplicity in engine design as a result of permitting the laser beam to enter the nozzle via the exhaust plane; and, 2) elimination of constraints resulting from plasma instability. However, the power conversion efficiency (efficiency of converting laser power to

power in the rocket exhaust) must be determined. In Ref. 4 a low power conversion efficiency was obtained because the pulse time of the laser was too long. In addition, with pulsed laser propulsion, thrust is obtained when laser energy is converted to kinetic energy by a continuously weakening shock wave traversing the propellant gas. The relative efficiency of generating thrust in this manner is not known a priori to be the same as when converting laser power to thrust in a steady process.

As a result of our past theoretical study the laser requirements for an experimental test of pulsed laser propulsion concepts were specified, and a suggested experiment was presented.⁸ In this report the results of a proof of principle experiment are presented. Our experimental objective is to demonstrate the feasibility of a pulsed laser propulsion system and to determine the specific impulse as a function of laser power, pulse repetition frequency, ambient conditions and propellant mass flow. The nozzle configuration is taken to be an idealized extension of the concept introduced in Refs. 2 and 4. A schematic of the single pulse nozzle configuration^{2,4} is presented in Fig. 1.1a. The nozzle walls focus the incoming beam to yield a breakdown in the propellant at the focus. With a short laser pulse, the resulting shock becomes a blast wave which propagates to the nozzle exit plane, converting all of the high pressure gas behind it into a force on the nozzle wall. This nozzle was designed for single pulse operation only. Therefore, no considerations of propellant supply were necessary. The fluid mechanics of a repetitively pulsed laser propulsion system was analyzed in Ref. 8, and thus, the fluid dynamics of the propellant feed system were included. The configuration analyzed is shown in Fig. 1.1b. The nozzle drawn with a solid line is

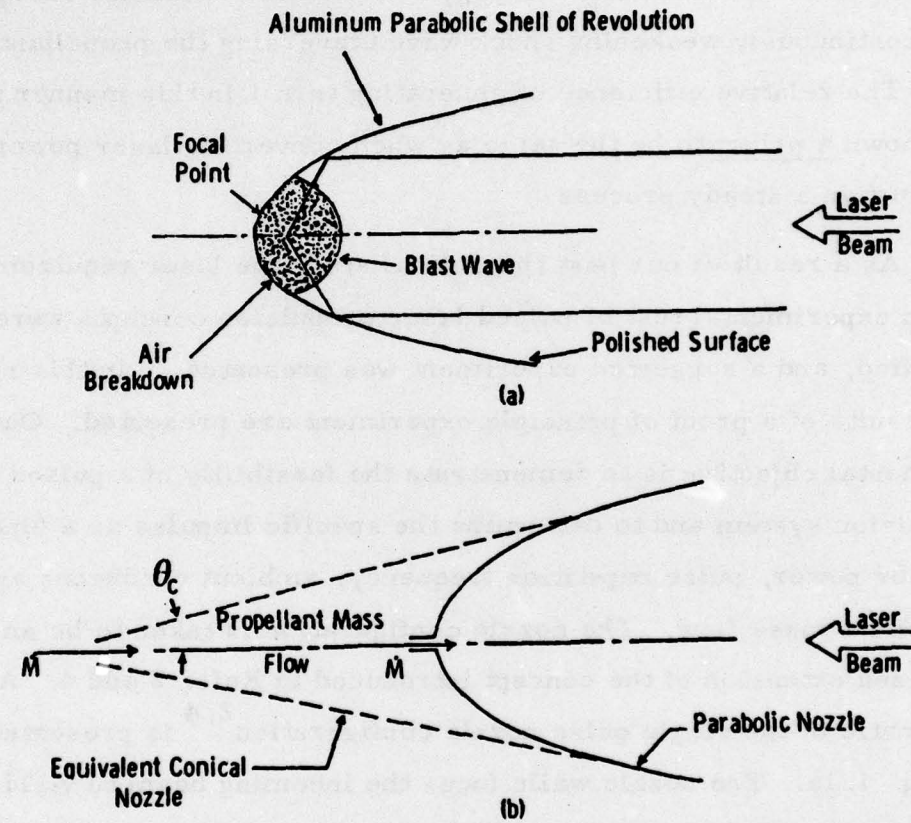


Fig. 1.1 a) Single Pulse Propulsion Concept as Introduced in Ref. 4.

b) Multiple Pulse Propulsion Concept and Equivalent Conical Nozzle.

the parabolic self focusing nozzle. However, for simplicity this nozzle was replaced by a conical nozzle which is shown dashed in the figure. The angle of the cone was chosen such that the exhaust gases leave the exit plane at the same angle relative to the thrust axis as with the parabolic nozzle. The beam was assumed to be focused externally so that the focusing angle equals the cone angle. The propellant was treated as a steady source flow entering at the apex (or "throat") of the conical nozzle, and periodically laser induced blast waves are ignited at $r = 0$ where r is measured from the apex.

Experiments were performed with both a self-focusing parabolic nozzle and a conical nozzle with external focusing. The helium propellant was delivered from a fixed volume reservoir and passed through the throat of the nozzle. At a predetermined repetition rate one, two, or three lasers were fired sequentially and the laser energy absorbed near the throat. The resulting expansion of the high temperature plasma and shocked propellant provided thrust at high specific impulse. The laser repetition rate and choked flow mass flow rate determined the amount of propellant mass heated during each pulse.

In this report the results of the feasibility experiments are presented in Section 2, the theory of pulsed laser propulsion, when the gas expands into a vacuum is reviewed, and also an update of the theory for operation with back pressure is presented. The rocket, laser system and associated parts used in the experiments are discussed in Section 3. The experiments using conical and parabolic nozzles at 1 atmosphere back pressure and experiments with the parabolic nozzle at reduced pressures are presented in Section 4. The scaling laws and maps for large scale operation are discussed in Section 5 along with other engineering considerations for a laser propulsion system. A Summary is presented in Section 6.

2. THEORETICAL UPDATE

2.1 Review of Model for Vacuum Operation

A fluid mechanical model has been developed to assess the performance of the laser-powered thruster concept as shown in Fig. 2.1. The model utilizes blast-wave theory to calculate the thrust and specific impulse in a vacuum environment. The details of the fluid mechanical model for operation in a vacuum environment are presented in Ref. 8, and briefly reviewed here. The nozzle is initially treated in a conical geometry for simplicity, and equivalence between the conical and parabolic nozzle is examined in Section 2.3. The theory for a single pulse is developed by considering the blast wave propagating into the nonuniform density field induced by the release of propellant in the throat region. A pulse sequencing theory is proposed to extend the single pulse theory to multiple pulse operation. An example result for the laser energy requirements in a vacuum environment is presented in Fig. 2.2 for helium and Fig. 2.3 for air.

In Fig. 2.2 the time between laser pulses is plotted versus the orifice diameter (diameter of throat through which the propellant is fed into the breakdown region). The propellant is taken to be helium which passes into the throat from a plenum chamber at 3 atmospheres stagnation pressure. This pressure is sufficient to "choke" the propellant flow at one atmosphere. ρ^* and u^* are the propellant density and velocity, respectively, in the throat before the laser pulse breaks down the propellant and produces the blast wave. The energy conversion efficiency is the ratio of energy in the blast that results in thrust to the laser energy. The results in Fig. 2.2 are for a 50% energy conversion efficiency. An operating corridor for multiple pulse laser propulsion at a specific impulse of 1000

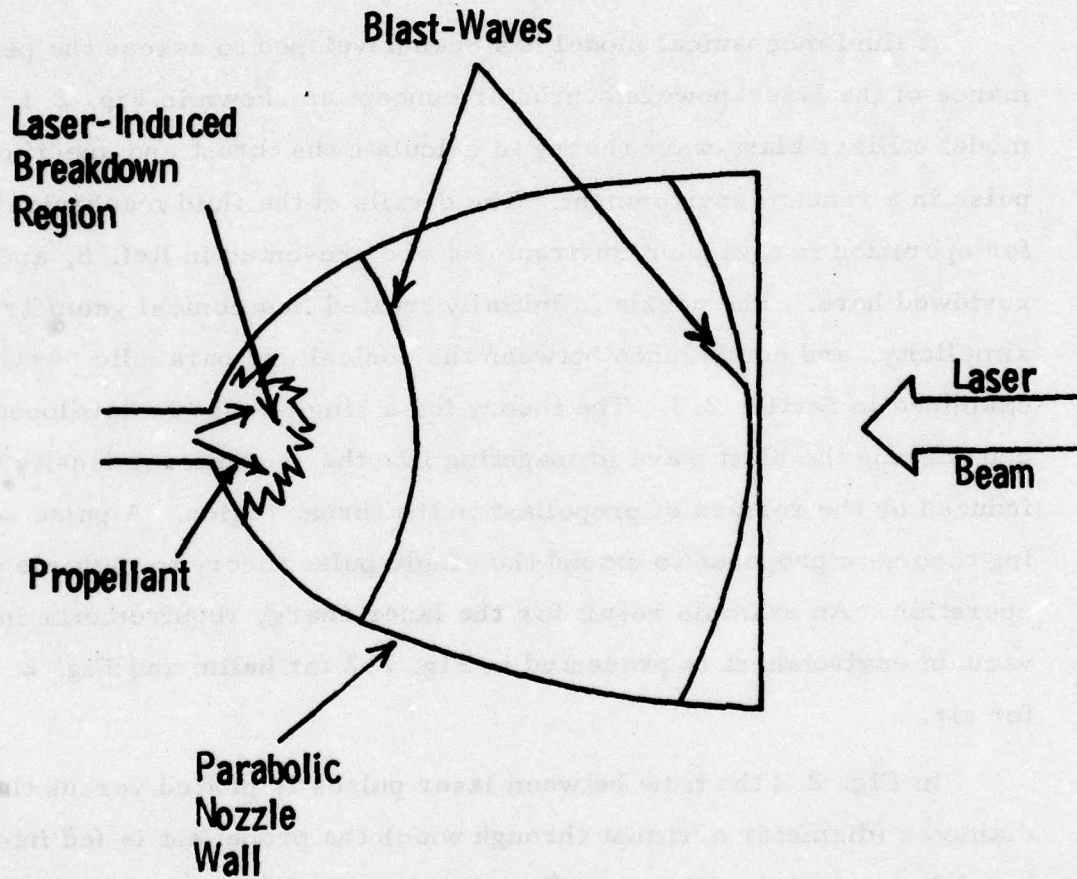


Fig. 2.1 Schematic of Repetitively Pulsed Laser Powered Thruster Concept.

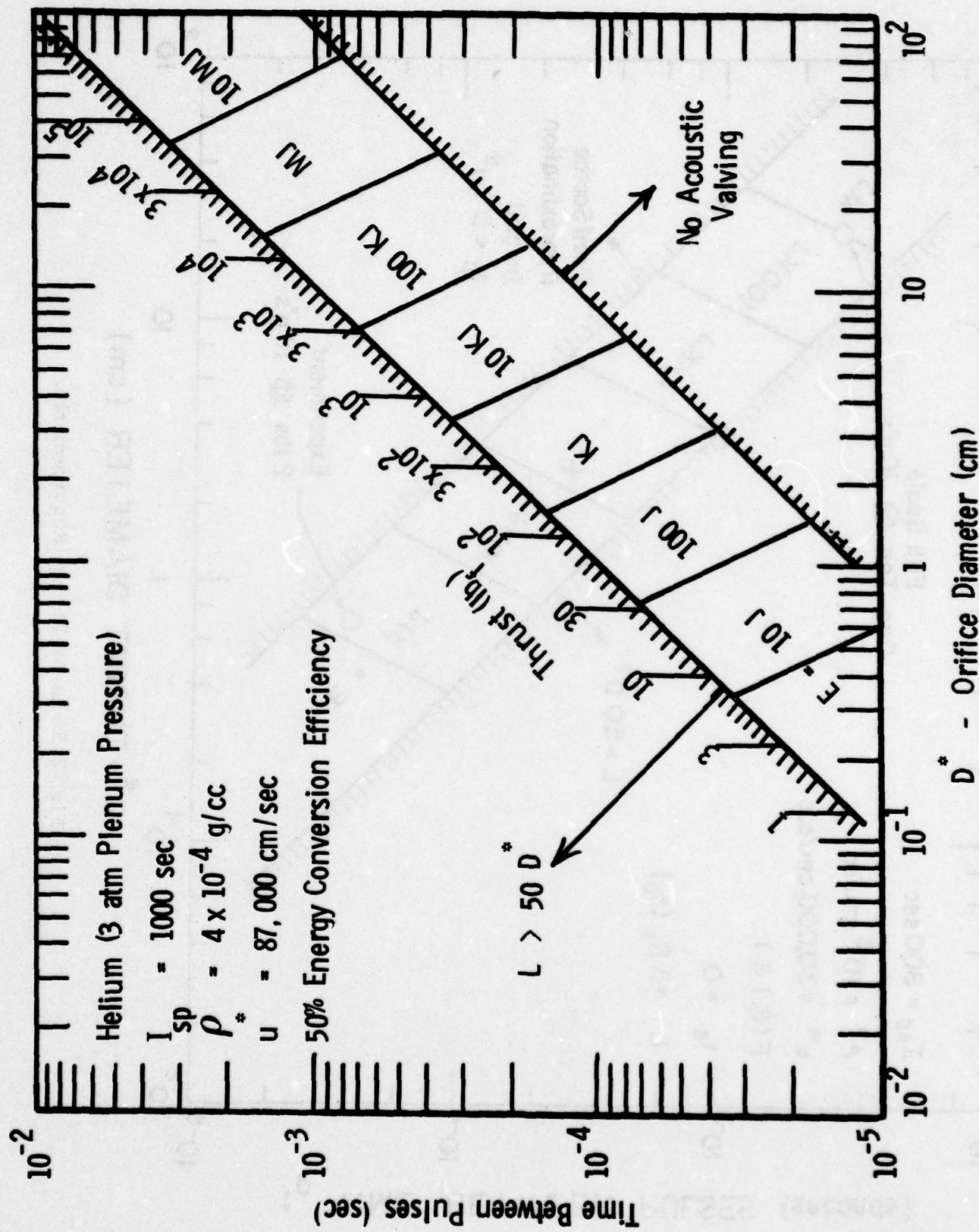


Fig. 2.2 Laser Energy Requirements : Vacuum Operation.

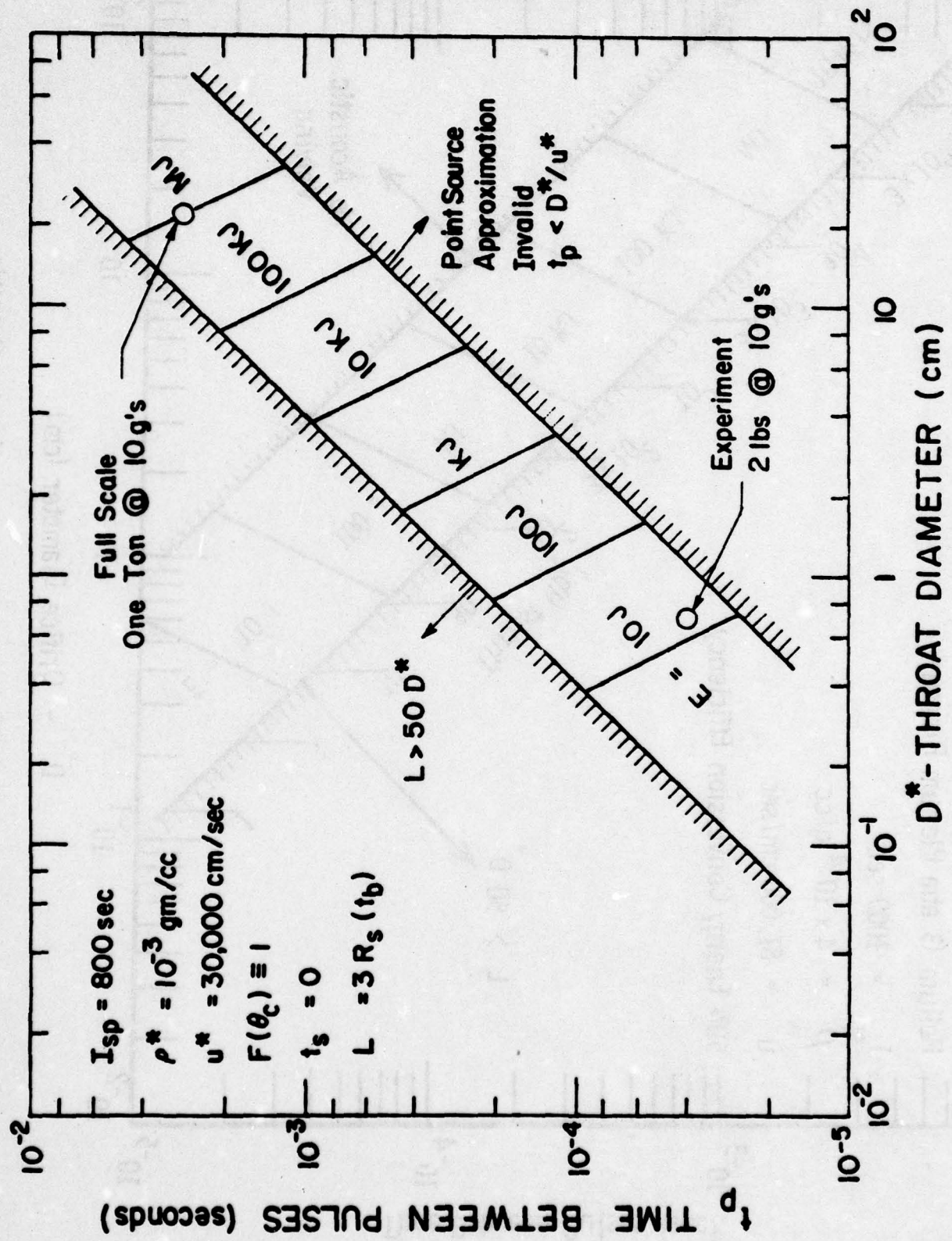


Fig. 2.3 Laser Energy Requirements.

sec is delineated in Fig. 2.2. The upper boundary of the corridor is set arbitrarily where the length of the conical nozzle is equal to fifty times the throat diameter. It is felt that aspect ratios greater than 50 may be undesirable for full scale operation due to engineering and weight considerations. The lower boundary of the corridor is set by propellant feed considerations, i.e., to the right of this boundary the time between pulses is so short that there is insufficient time for propellant to enter the nozzle between laser pulses. This is designated as the acoustic valving limit. Constant energy lines are shown within the operating corridor and vertical lines of constant thrust are presented. As an example, a 100J per pulse laser operating at 7×10^{-5} sec between pulses (14,285 pps) is capable of powering a 132 Nt (30 lb) thrust rocket engine that has a throat diameter of 0.7 cm and a length (if it were conical) of 35 cm. Similarly, a 100 KJ per pulse laser at 7×10^{-4} sec between pulses (1,428 pps) will power a 13,200 Nt (3000 lb) thrust engine with a 7 cm throat and a conical length of 3.5 m.

2.2 Finite Back Pressure Operation

A description of pulsed laser propulsion operating at finite back pressure may be developed in a manner similar to the vacuum mode. The prepulse flow field is established first; then the single pulse is modeled, and finally, pulse sequencing for REP operation is outlined.

Consider the prepulse propellant flow through a conical nozzle operating at finite ambient pressure p_∞ . The plenum pressure is p_0 and is so chosen to choke the flow at the sonic orifice. Downstream of the orifice, the flow accelerates supersonically and then shocks down to subsonic flow as illustrated in Fig. 2.4. It is noted here that the nozzle length will be chosen such that the blast wave will remain strong enough

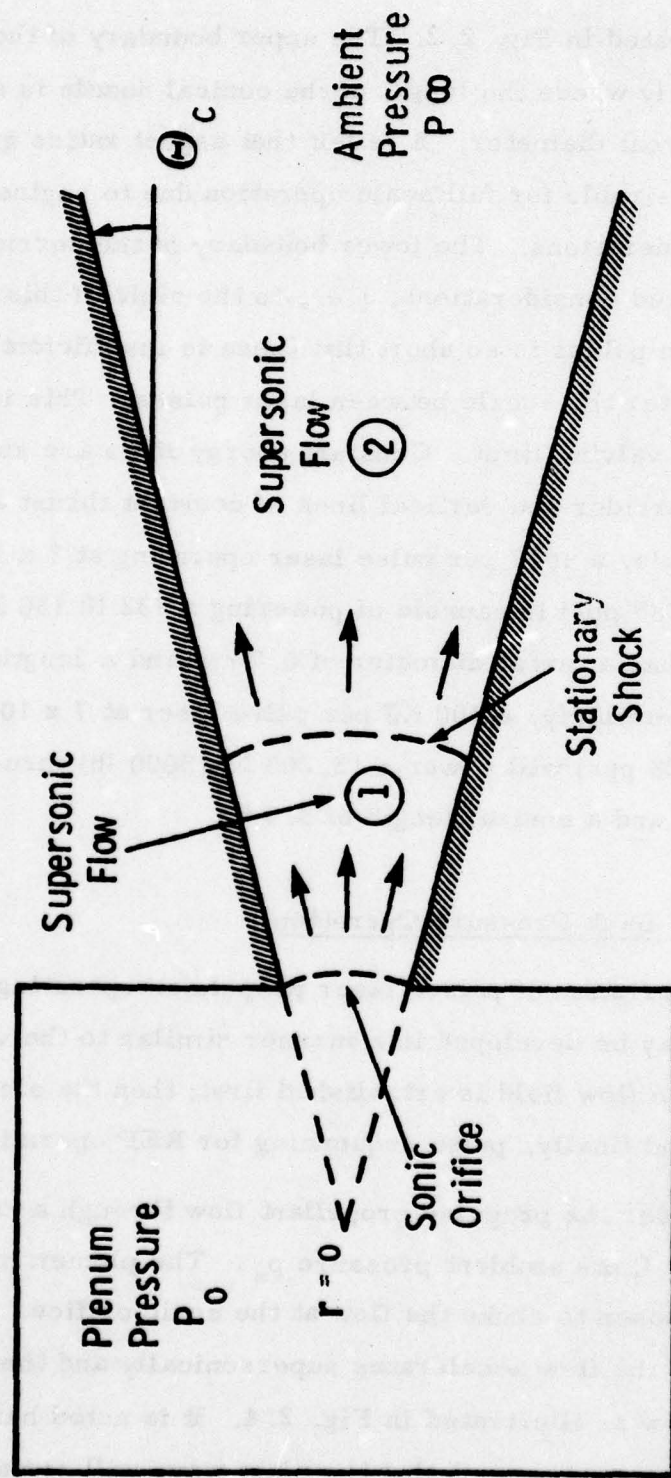


Fig. 2.4 Conical Nozzle - Propellant Flow at Finite Back Pressure.

to propagate from the orifice to the exit plane. Hence, the weaker shock, established by the chamber pressure p_o , cannot propagate to the exit plane and will remain stationary in the diverging portion of the nozzle.

Within the conical nozzle, continuity requires

$$u = \frac{\rho^* u^* (r^*)^2}{\rho r^2} \quad (2.1)$$

where u is the gas velocity, ρ is the gas density, $*$ denotes sonic conditions and r is measured from the apex of the cone. The sonic radius r^* is related to the orifice diameter D^* by

$$r^* = \left(\frac{\pi}{4\Omega} \right)^{\frac{1}{2}} D^* \quad (2.2)$$

where Ω is the solid angle of the cone

$$\Omega = 2\pi (1 - \cos \theta_c) \quad (2.3)$$

and θ_c is the cone half angle. The density in the subsonic flow is approximately equal to $\rho_o p_\infty / p_o$. Hence, the gas density and velocity in the subsonic section are

$$\rho_2 = \left(\frac{\gamma+1}{2} \right)^{1/(\gamma-1)} \rho^* p_\infty / p_o \quad (2.4)$$

and

$$u_2 = \left(\frac{2}{\gamma+1} \right)^{1/(\gamma-1)} p_o / p_\infty u^* \left(\frac{r^*}{r} \right)^2 \quad (2.5)$$

respectively.

Equations (2.4) and (2.5) describe a subsonic flow of approximately uniform density. Hence, the blast wave formed by the laser energy deposition propagates into a nearly uniform atmosphere. The Sedov solution for the motion of the shock front yields

$$R_s = \xi_0 \left(\frac{E}{\rho_2} \right)^{1/5} \left(\frac{4\pi}{\Omega} \right)^{1/5} t^{2/5} \quad (2.6)$$

where ξ_0 is a constant of order unity and factor $(4\pi/\Omega)^{1/5}$ is introduced since the energy E is restrained to expand into Ω instead of 4π steradians.

The length (L) of the nozzle is chosen such that the shock velocity, dR_s/dt , is twice the speed of sound (a_∞) at the nozzle exit plane. This insures that the gas pressure within the nozzle is always in excess of p_∞ . The time corresponding to the shock propagation from $r = 0$ to $r = L$ is denoted by t_{blast} ,

$$t_{blast} = \frac{L^{5/2}}{\xi_0^{5/2} \left(E/\rho_0 \right)^{1/2} \left(4\pi/\Omega \right)^{1/2}} \quad (2.7)$$

Solving the equation $dR_s/dt = 2a_\infty$ for $L = R_s$ at $t = t_{blast}$, we obtain

$$L = \frac{\xi_0^{5/3} \left(E/\rho_2 \right)^{1/3} \left(4\pi/\Omega \right)^{1/3}}{(5a_\infty)^{2/3}} \quad (2.8)$$

The pulse sequencing theory requires that the laser pulse be repeated on a time scale which is somewhat less than t_c , the time required

for the flow to convect through the nozzle, otherwise propellant will exit the nozzle without being shocked. The convection time may be obtained by integrating the fluid velocity, $u(r)$. Omitting the relatively short time required for the gas to convect through the supersonic portion of the nozzle, we obtain

$$t_c = \frac{L^3}{3 \left(\frac{2}{\gamma + 1} \right)^{\frac{1}{\gamma - 1}} (p_0/p_\infty) u^* (r^*)^2}, \quad (2.9)$$

where in omitting the superonic flow, we have assumed that L is much greater than the shock location

$$L \gg r^* \left(\frac{A^*}{A} \right)^{1/2} \quad (2.10)$$

and the area ratio A/A^* is known function of p_0/p_∞ through the normal shock relations.

Having defined the relevant times and nozzle length, the theoretical value of the impulse that may be obtained from this system may be determined by extending the vacuum theory. The vacuum and finite back pressure cases are identical when the time between pulses (t_p) is chosen such that it is equal to the convection time t_c . In this case, the Nth shock processes the propellant released during the Nth cycle and the gas expands through a nozzle that is one breakthrough radius in length. The time and spatial pressure fields may differ in the finite back pressure and vacuum cases but the momentum transfers are practically identical because the pulse energy and propellant masses at breakthrough are identical. The length of the nozzle has been chosen such that the gas pressure is well in excess of p_∞ ($V_s = 2a_\infty$) and the percent of the vacuum

thrust recovered is limited only by the length of the nozzle. The vacuum theory indicates that the specific impulse for this length nozzle is 3/4 of the vacuum limit.

$$I_{sp} (t_p = t_c) = \frac{3}{4} I_{sp} \left|_{\text{vacuum}} \right. \quad (2.11)$$

for $\gamma = 5/3$, independent of p_∞ . The expression for I_{sp} vacuum has been previously derived and is restated:

$$I_{sp} \sim \frac{1}{g} \frac{8}{\pi}^{1/2} \left(\frac{E}{p^* u^* (D^*)^2} \right)^{1/2} \left(\frac{1}{t_p} \right)^{1/2} \quad (2.12)$$

When t_p is less than t_c , the Nth pulse propagates through the propellant released during the Nth cycle, and through the tail of the previous pulse. The tail of the previous pulse is a gas of pressure p_∞ and was non-existent in the vacuum case. The net effect of this tail is to enhance the specific impulse of the system. Each successive pulse will see a nozzle filled with propellant at a pressure of approximately p_∞ . Hence, each pulse delivers the same total impulse, independent of t_p , but the mass of propellant expanded during each pulse increases in direct proportion of t_p . Subsequently, the specific impulse scales as $1/t_p$ and the constant is chosen to recover Eq. (10) when $t_p = t_c$

$$I_{sp} (p_\infty) = \frac{3}{4} \left(\frac{t_c}{t_p} \right) I_{sp} \left|_{\text{vacuum}} \right. \quad (2.13)$$

Values specific to our experiments were inserted into Eq. (2.13) and the results are illustrated in Fig. 2.5. The results of Eqs. (2.7), (2.9), and (2.13) may be used to compare with experiment results at finite back pressure using the 15° conical nozzle and this will be done in Section 4. In addition, these equations will be used to determine scaling laws which are discussed in Section 5.

2.3 Equivalence Between Conical and Parabolic Nozzles at Finite p_∞

A fluid dynamical theory discussed above, described pulsed laser propulsion using a conical nozzle and an externally focused beam. In this subsection we consider the requirements for an equivalent self-focusing parabolic nozzle which meets the design conditions set forth for the conical nozzle. From a one-dimensional steady gas dynamic point-of-view, the area ratio for both nozzles must be the same in order to yield the same gas pressure and velocity at the nozzle exit plane. To achieve proper pulse sequencing, the fluid convection time and the shock propagation time through the nozzle must also be equivalent.

A coordinate system is established at throat of the parabolic nozzle, Fig. 2.5. The parabolic nozzle is described by

$$y_p = B \sqrt{x} \quad (2.13)$$

and the conical nozzle by

$$y_c = \theta_c (x + x_0) \quad (2.14)$$

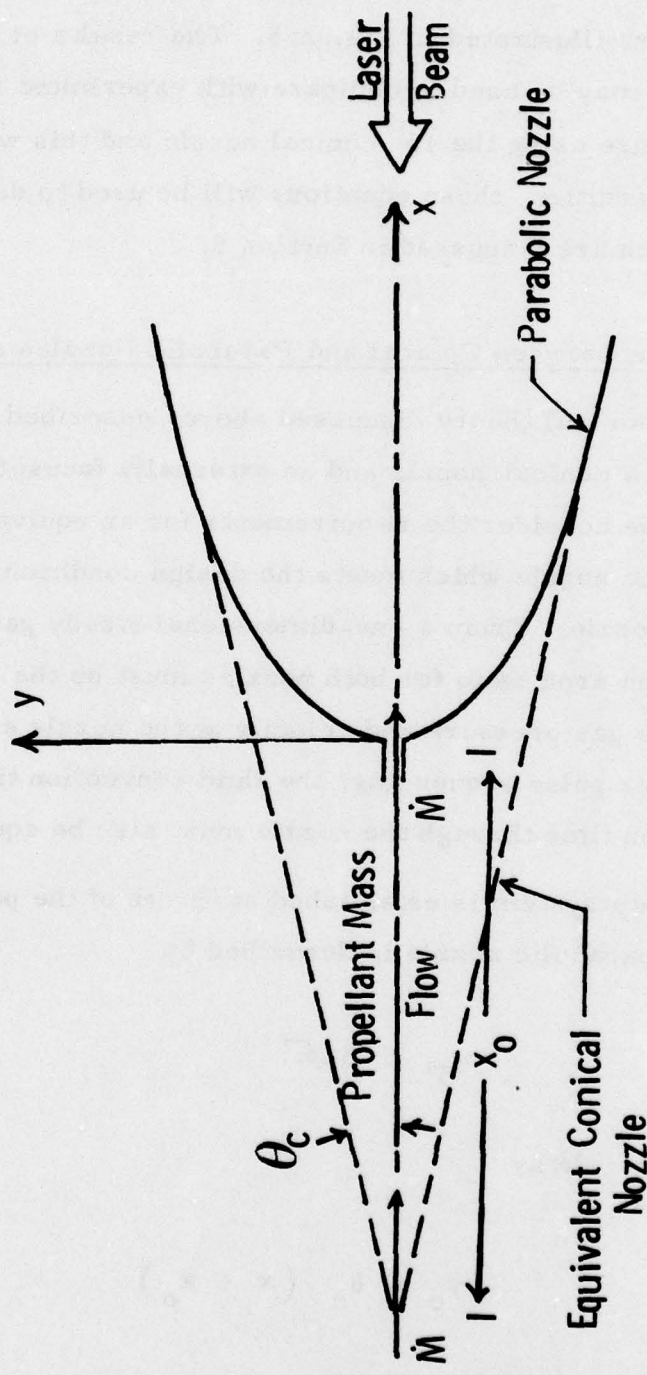


Fig. 2.5 Parabolic Nozzle Equivalent to Conical Nozzle.

where x_o is the distance from the apex of the conical nozzle to the parabolic nozzle. Choosing B and x_o such that both nozzles have the same area ratio and divergence angle at the exit plane, we obtain

$$B = 2 \theta_c \sqrt{L_p}$$

and

$$x_o = L_p ,$$

where L_p is the length of the parabolic nozzle. From the definition of x_o it follows that the length of the equivalent parabolic nozzle is one half of that of the conical nozzle (L_c)

$$L_p = 0.5 L_c .$$

To establish an equivalence of the basis of the flow convection time, one-dimensional gas dynamics is used. The difference in the area vs. x histories of the two nozzles indicates that the convection times are identical if

$$L_p = \left(\frac{1}{6}\right)^{1/3} L_c \approx 0.55 L_c ,$$

where it should be noted that this relationship is valid only in subsonic flow (finite p_∞ operation). For vacuum operation, the gas reaches its limiting velocity and L_p must equal L_c for equivalent convection times. Hence, there is no equivalence between parabolic and conical nozzles for vacuum operations.

The shock propagation time is also an important part of the pulse sequencing. In a conical nozzle operating at finite p_∞ , the shock velocity decay is $1/x^{3/2}$ or $(\text{area})^{-3/4}$. Using the area history for the parabolic nozzle the shock propagation times are equivalent if

$$L_p = \frac{1}{2} \left(\frac{7}{5}\right)^{2/5} L_c \quad L_c = 0.57 L_p .$$

These three criteria for the equivalence between parabolic and conical nozzles are slightly inconsistent for finite p_∞ operation. However, one can use this approximate equivalence to design an experiment using parabolic nozzles at finite background pressure and expect to achieve the specific impulses predicted by the conical nozzle theory. Ultimately, a more detailed theory is necessary but for the present time, the theory is developed only to the point of defining appropriate experiments. In addition, a theory for parabolic nozzles needs to be developed for vacuum operation conditions (i.e., when the cold propellant is supersonic throughout the nozzle).

3. EXPERIMENT DESIGN AND ASSEMBLY

3.1 Nozzle Design

Experiments were performed using two distinct nozzle configurations, conical and parabolic. Because the theoretical modeling was for a conical nozzle, a series of experiments were performed with a conical nozzle to compare with the theoretical predictions. This configuration is gasdynamically the simplest, and beam focusing is accomplished externally, permitting control and variation of laser beam spot size and breakdown location. On the other hand, because a full size rocket will use a self-focusing nozzle, experiments with a parabolic nozzle were also performed. This nozzle is optically optimum and permits near spherical focusing of a collimated laser beam.

3.1.1 Conical Nozzle

The size of the nozzle was determined using the theoretical predictions for an I_{sp} performance of approximately 800 sec. Because experiments were to be performed at different ambient pressures (from one atmosphere to a vacuum), a flexibility of having two nozzle lengths was built into a design. Theoretically, it has been determined that a nozzle length equal to $3 R_b$, where R_b is the "breakthrough" radius, provides greater than 90% of the thrust obtained with an infinitely long nozzle when the propellant specific heat ratio $\gamma \geq 1.5$.⁸ Therefore, we will make the nozzle length to be $3 R_b$ for a specific operation condition. Considering the design map for vacuum operation with air as a propellant shown in Fig. 2, 3 and $D^* = 0.5$ cm, which is appropriate for laser energies from 5 to 15 J, a reasonable choice of maximum interpulse time is 100 μ sec. $R_b \approx 8$ cm for this case and the nozzle length was made 24 cm long.

When the rocket is operated in a finite back pressure environment, a normal shock will exist in the nozzle for the cold propellant flow (see Section 2). Therefore, different design criteria for the nozzle lengths are appropriate as discussed in Section 2. Specifically, the laser induced blast wave pressure at the exit plane should be strong compared to the maximum background pressure. This requirement for laser energies $\geq 4\text{ J}$ is met by a nozzle 3.2 cm long operating at 1 atm. Therefore, the nozzle was made 24 cm long with a detachable skirt 20.8 cm long. A schematic of the conical nozzle - plenum chamber assembly is presented in Fig. 3.1. In order to minimize the weight of the assembly, aluminum was used. The plenum is attached to the nozzle with a diaphragm in between to maintain the stagnation pressure in the plenum until the experiment is performed. Design considerations for the plenum will be discussed below. The rocket is completely self-contained to permit use of a ballistic pendulum as is discussed below. The nozzle half angle was chosen to be 15° and greater than 95% of the theoretical thrust can be anticipated with this nozzle angle.⁸ In addition, this angle allows multiple laser beams to be focussed at the throat. Four pressure transducer ports are provided to mount four LD-80 (Celeseo Products Inc.) pressure transducers. One transducer is mounted in the plenum wall to monitor the change in the stagnation pressure during the experiment. The second transducer is mounted close to the nozzle throat to measure high pressures in the breakdown region. The third transducer is placed at the estimated "break-through" radius to determine the propellant pressure prior to the isentropic expansion,⁸ and the fourth transducer is mounted in the exhaust plane.

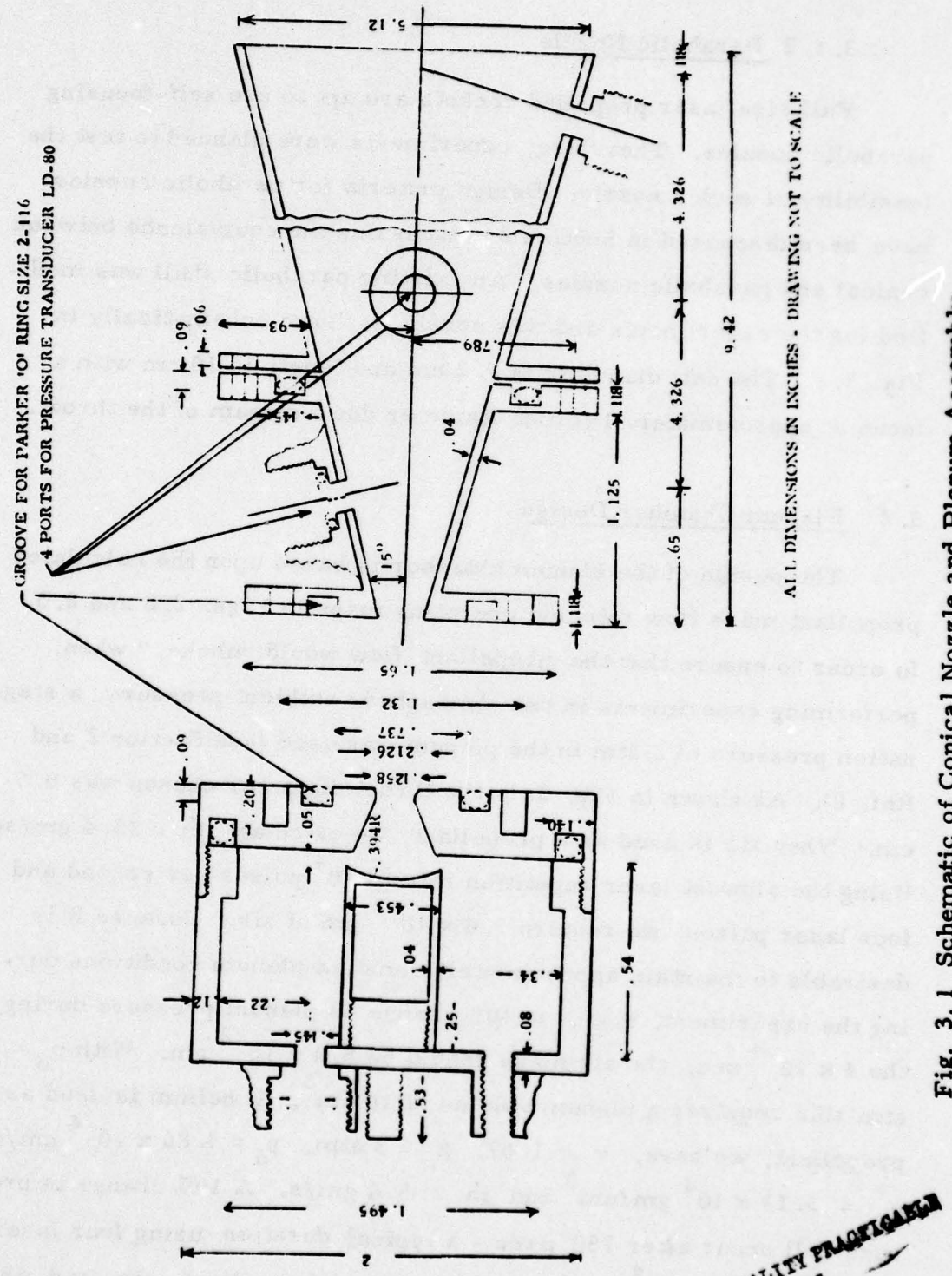


Fig. 3.1 Schematic of Conical Nozzle and Plenum Assembly.

THIS PAGE IS BEST QUALITY PRATICABLE
FROM COPY FINISHED TO DDC

3.1.2 Parabolic Nozzle

Full size laser propelled rockets are apt to use self-focusing parabolic nozzles. Therefore, experiments were planned to test the feasibility of such a nozzle. Design criteria for parabolic nozzles have been discussed in Section 2 discussing the equivalence between conical and parabolic nozzles. An existing parabolic shell was modified for the experiments and this nozzle is shown schematically in Fig. 3.2. The exit diameter is 7.2 cm and length is 10 cm with a focus at approximately 1 throat diameter down stream of the throat.

3.2 Plenum Chamber Design

The design of the plenum chamber is based upon the calculated propellant mass flow rate and operating maps in Figs. 2.2 and 2.3. In order to ensure that the propellant flow would "choke," when performing experiments in one atmosphere ambient pressure, a stagnation pressure of 3 atm in the plenum was used (see Section 2 and Ref. 8). As shown in Fig. 3.1, the throat diameter chosen was 0.5 cm. When air is used as a propellant, we calculate $\dot{m} = 13.4 \text{ gm/sec}$. Using the slowest laser repetition rate of 10^4 pulses per second and four laser pulses, we require $5.4 \times 10^{-3} \text{ gm}$ of air. Because it is desirable to maintain approximately constant plenum conditions during the experiment, e.g., $\leq 10\%$ change in plenum pressure during the $4 \times 10^{-4} \text{ sec}$, the air mass should be $5.4 \times 10^{-2} \text{ gm}$. With $p_o = 3 \text{ atm}$ this requires a plenum volume of 16 cm^3 . If helium is used as a propellant, we have, $\gamma = 1.67$, $p_o = 3 \text{ atm}$, $\rho_o = 4.86 \times 10^{-4} \text{ gm/cm}^3$, $\rho^* = 3.13 \times 10^4 \text{ gm/cm}^3$ and $\dot{m} = 5.4 \text{ gm/s}$. A 10% change in pressure will occur after 150 μsec - a typical duration using four laser pulses. The 16 cm^3 plenum is appropriate for helium, air, and other propellant gases.

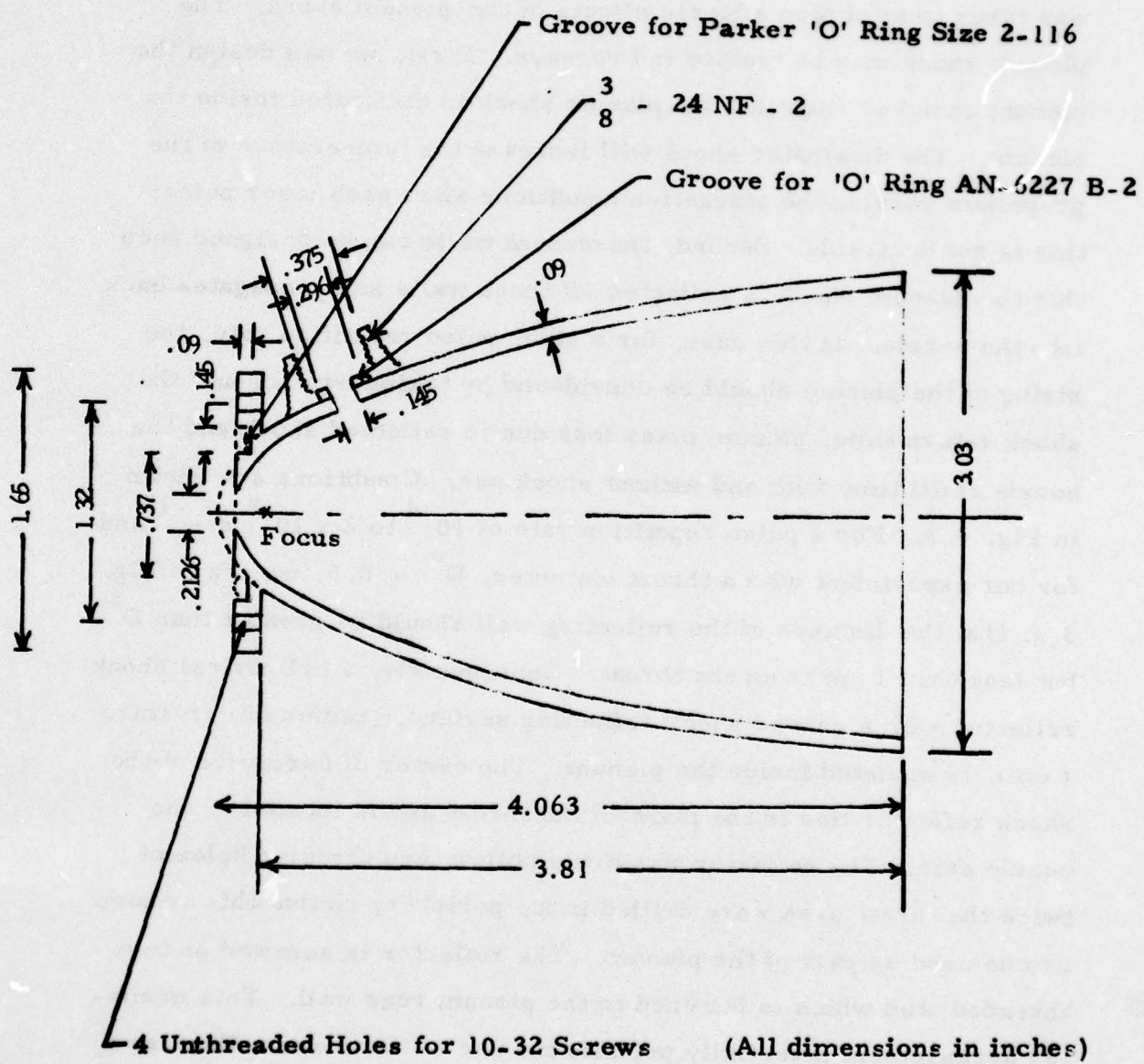


Fig. 3.2 Parabolic Nozzle.

When the high energy laser pulse is focused at the throat, the blast wave generated propagates into the plenum as well as the nozzle. The shock will propagate upstream of the throat because the shock is much stronger than the plenum stagnation pressure. Because the shock could significantly perturb the propellant mass flow conditions, care was taken to minimize adverse effects of the plenum shock. The plenum shock may be treated in two ways. First, we can design the plenum chamber such that the plenum shock is dissipated inside the plenum. The dissipated shock will increase the temperature of the propellant varying the stagnation conditions after each laser pulse; this is not desirable. Second, the plenum walls can be designed such that the plenum shock is reflected off these walls and propagates back into the nozzle. In this case, for a given pulse repetition rate, the sizing of the plenum should be considered by taking into account the shock return time, plenum mass loss due to reflected shock and the nozzle refill time with and without shock gas. Conditions are shown in Fig. 3.3. For a pulse repetition rate of 10^{+4} to $2 \times 10^{+5} \text{ sec}^{-1}$ and for our experiment with a throat diameter, $D^* = 0.5$, we see in Fig. 3.3. that the distance of the reflecting wall should be greater than D^* but less than 1 cm from the throat. Consequently, a cylindrical shock reflector with a curved shock reflecting surface, (radius of curvature 1 cm), is mounted inside the plenum. The center of curvature of the shock reflector lies in the plane of the throat and is located on the nozzle axis. The reflector was made hollow and circular holes of twice the throat area were drilled in its periphery so that this volume can be used as part of the plenum. The reflector is screwed on to a threaded stud which is fastened to the plenum rear wall. This mounting arrangement potentially permits the use of the shock reflectors of different designs if desirable.

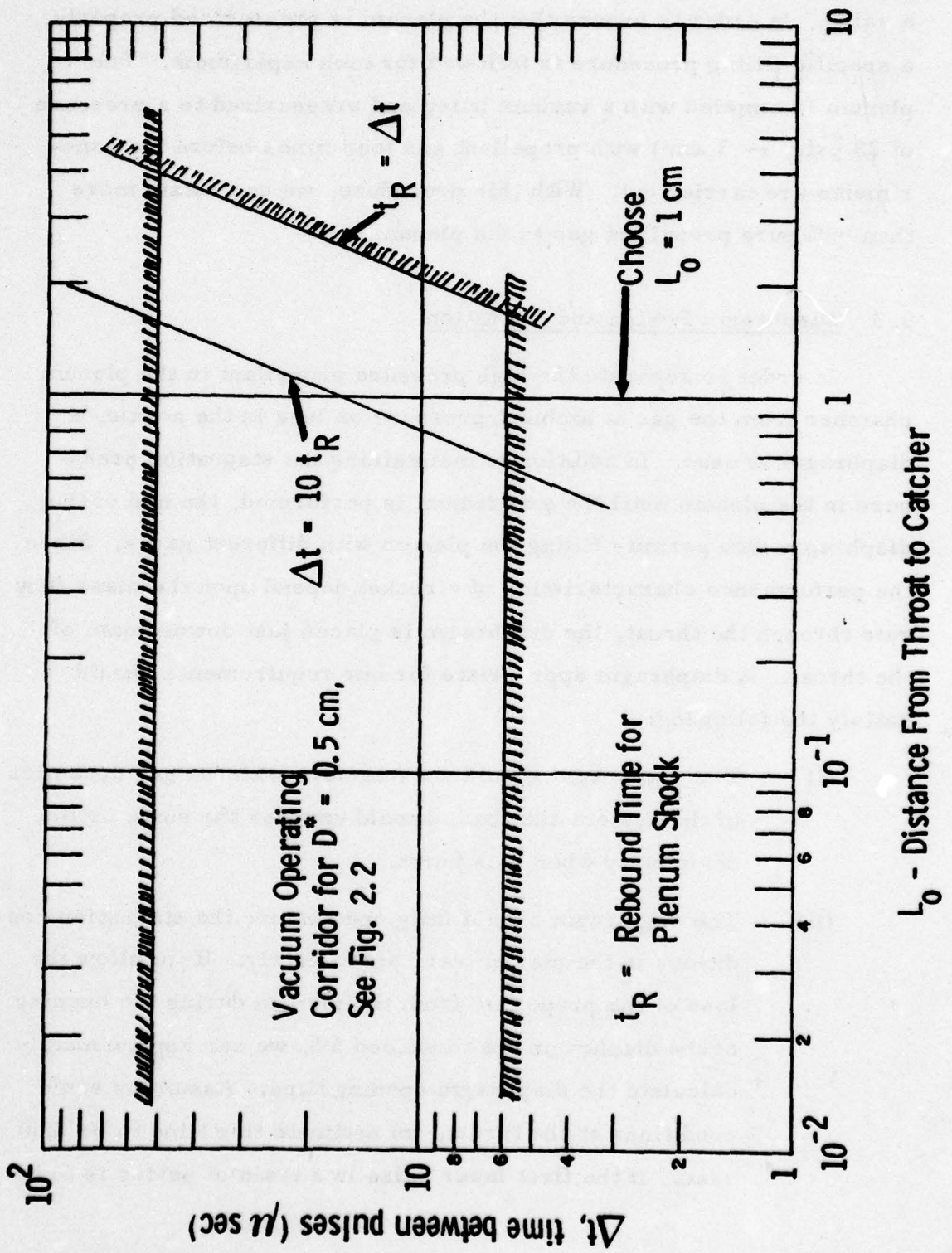


Fig. 3.3 Location of Shock Catcher.

At the rear plenum wall, a threaded gas inlet port is provided for a valve. In order to ensure that the plenum is pressurized properly, a specific filling procedure is followed for each experiment. The plenum is emptied with a vacuum pump and pressurized to a pressure of 28 psig, (~ 3 atm) with propellant gas four times before the experiments are carried out. With this procedure, we can obtain more than 99% pure propellant gas in the plenum.

3.3 Diaphragm Design and Operation

In order to separate the high pressure propellant in the plenum chamber from the gas at ambient pressure or less in the nozzle, a diaphragm is used. In addition to maintaining the stagnation pressure in the plenum until the experiment is performed, the use of the diaphragm also permits filling the plenum with different gases. Since the performance characteristics of a rocket depend upon the mass flow rate through the throat, the diaphragm is placed just downstream of the throat. A diaphragm appropriate for our requirements should satisfy the following:

- (i) The diaphragm should not interfere with the gas dynamics of the system and thus, should uncover the sonic orifice completely when it is burst.
- (ii) The diaphragm should fully open before the stagnation conditions in the plenum vary significantly. If we allow the loss of the propellant from the plenum during the opening of the diaphragm not to exceed 5%, we can approximately calculate the diaphragm opening time. Assuming sonic conditions at the throat, we estimate this time to be 200 μ sec. If the first laser pulse in a train of pulses is to be

meaningful, the diaphragm opening time requirements are more stringent. Typically, for an interpulse time of 30 μ sec, the diaphragm should fully open in less than 30 μ sec.

- (iii) It must hold a pressure difference of three atmosphere without a leak.
- (iv) It should be convenient to use.

Based upon the aforementioned requirements, a number of materials including aluminum, copper, Mylar and latex were considered and tried. We also examined diaphragm scoring techniques such as chemical etching, electroplating and scribing. From a comparison of different diaphragm materials, it was found that the latex diaphragm best suits our requirements. The latex material is stretched over the nozzle flange. In order to control the magnitude of the tension on the diaphragm, a circle was printed on the surface of the latex material and stretched by 500%. Each time it was ensured that the deviation of the stretched printed circle from a perfect circle was less than 10% at a specified radius. This scheme ensures that the diaphragm is stretched uniformly to a reasonable degree of accuracy for each experiment.

The diaphragm was punctured with an electrical spark. A series of experiments were done to determine the electrode position which yields the minimum opening time. The diaphragm opening time was measured by monitoring light transmission through the throat and by this technique which is described below. It was concluded that the electrode should be halfway between the O ring and the nearest edge of the throat (see Fig. 3.1).

As discussed above, determination of the time it takes for the diaphragm to be fully open is necessary in our experiment. A technique which monitors the transmission of a He-Ne laser beam through the diaphragm was employed for this purpose. This scheme is illustrated in Fig. 3.4. A He-Ne laser beam is deflected at right angles using a beam splitter and is then focused onto the shock reflector in the plenum using a focusing lens. A photodiode detects the light that is reflected from the shock reflector and transmitted through the diaphragm which is translucent. In Fig. 3.5, we show the oscilloscope trace of the reflected light. As the diaphragm tears, the diaphragm loses some of its tension at the throat where the transmission of He-Ne beam is being monitored and becomes thicker and thus more optically dense. For this reason, in Fig. 3.5, we see that just after the diaphragm is punctured, the transmitted light intensity decreases but increases again when the diaphragm clears the hole. With a pressure difference of 28 psi across the diaphragm and with a beam diameter of 1.5 mm it was found that the diaphragm starts to open in about 60 μ sec and fully opens in about 78 μ sec. We have also done experiments with a beam diameter of 0.5 cm and with no pressure difference across the diaphragm. The corresponding opening times are 60 μ sec and 110 μ sec.

3.4 Optical Train

Optical systems were designed for both the parabolic and conical nozzle. Each system may have to generate irradiances of $\geq 10^9 \text{ W/cm}^2$ near the nozzle throat to produce the needed laser-induced breakdown in the propellant gas. This was accomplished by 30 cm focal length mirrors for each laser beam and the short conical nozzle experiments. The parabolic nozzle self-focused the laser beams to produce the breakdown. Experiments were not performed with the 24 cm long conical nozzle due to

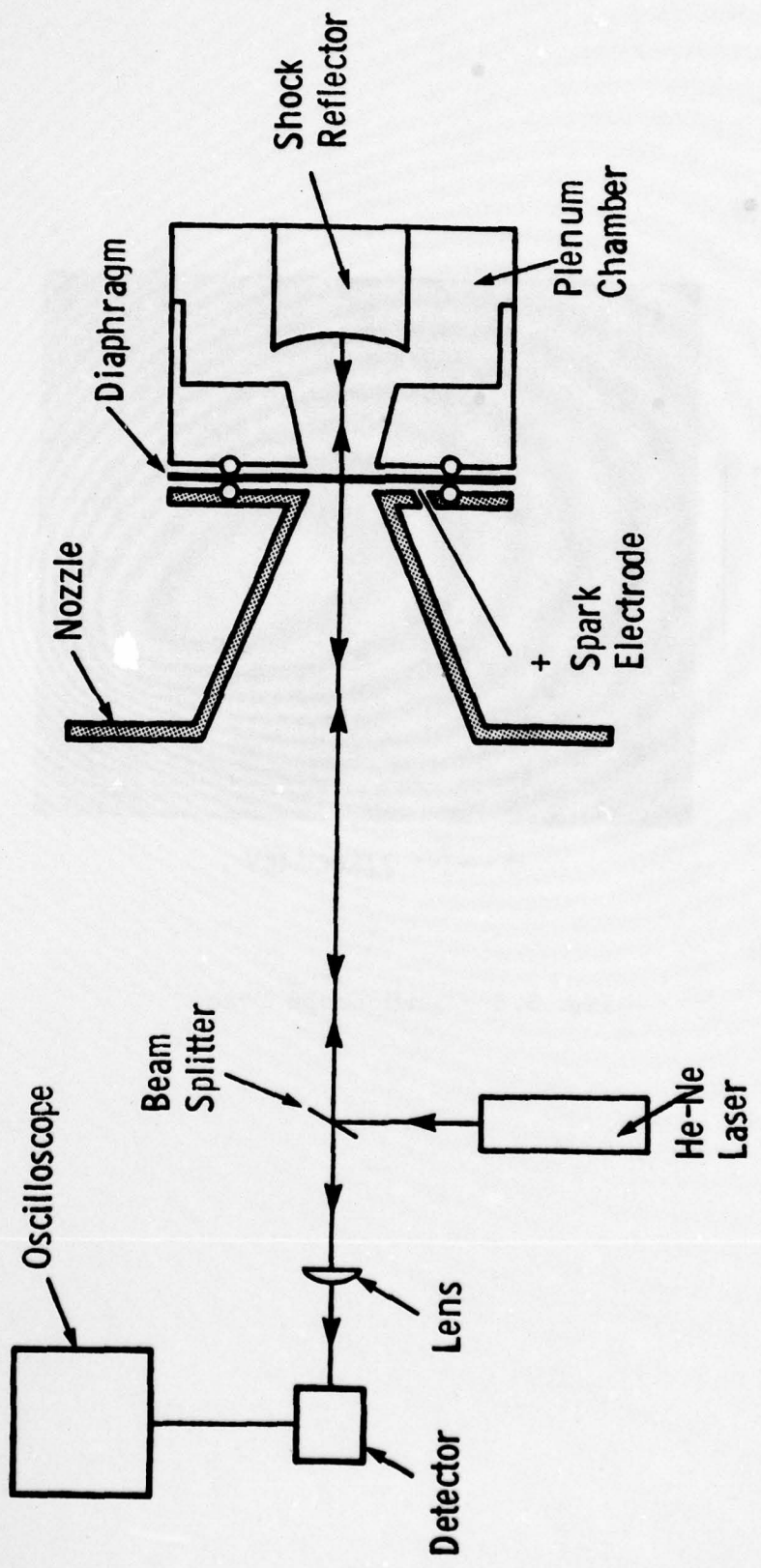


Fig. 3.4 Schematic for Measuring Diaphragm Opening Time.

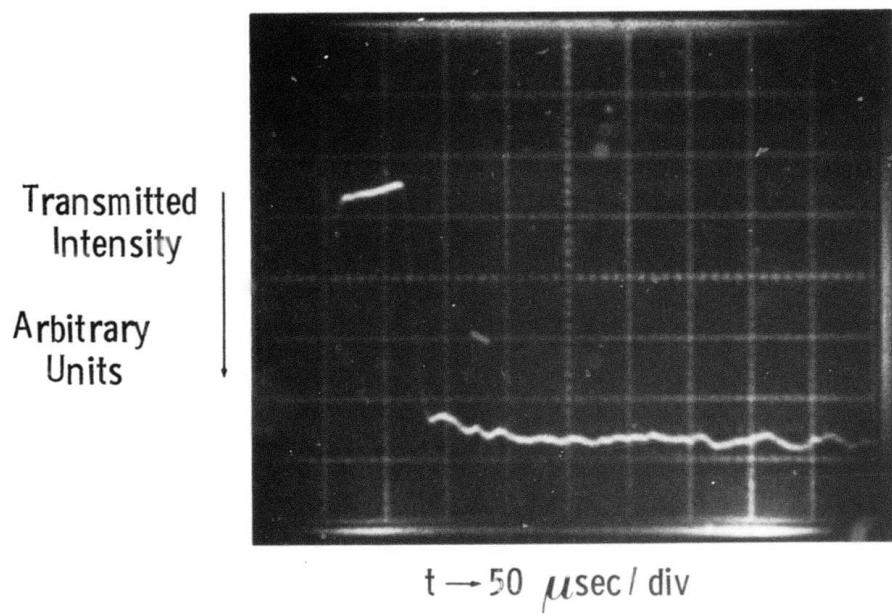


Fig. 3.5 Oscilloscope Trace.

lack of time but, the optical system was designed. The optical system is composed of a set of four off axis telescopes. Each telescope is composed of first a 5 cm diameter divergent mirror and a 10 cm diameter convergent mirror. This arrangement was necessary in order to obtain the irradiance of $\geq 10^9 \text{ W/cm}^2$ at a distance much greater than the nozzle length. The distance was chosen to be 60 cm by a trade-off between off-axis angle, focal length, and diameter of the primary mirror. Calculations of the astigmatism introduced by an off-axis telescope were made and found to be intolerable - i.e., the high intensity area would be too large. Therefore, the straightforward technique for using orthogonal planes to eliminate astigmatism was investigated and was determined to be satisfactory. This means that the sagittal rays from the small divergent mirror became the tangential rays of the large convergent mirror.

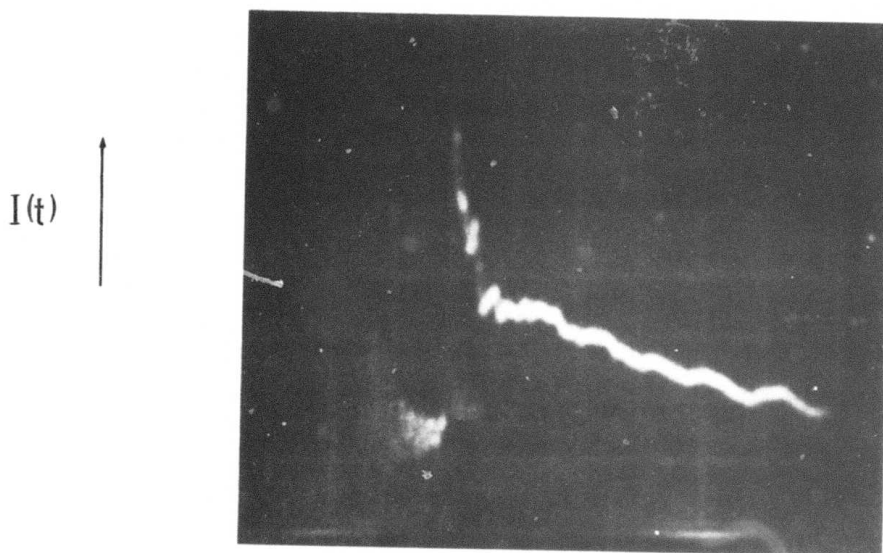
The optical system for the parabolic nozzle consisted of plane mirrors directing each $3 \times 3 \text{ cm}$ laser beam into the parabola. The angle between each laser beam and the axis of symmetry was approximately 6×10^{-2} radians.

3.5 Laser System and Delay Generator

The laser system used to investigate multiple pulse laser propulsion is composed of three CO₂ laser kits (K-103) from Lumonics Research Ltd. of Canada. These TEA lasers are charged from one high voltage power supply, and triggered individually from a four channel variable delay trigger generator. Therefore, one, two, or three laser pulses were obtained with various interpulse times.

The CO₂ TEA laser is a short pulse laser. Typically the output pulse of such a laser has a very short high power spike followed by a lower power but longer duration "tail." This "tail" can contain up to 2/3 of the total laser energy. The experiments consisted of operating the lasers with a flowing gas mixture of He : CO₂ : N₂ of 5 : 1.6 : 0.8 SCFH measured with flow meters calibrated for air. The laser capacitors were charged to 32 kV, and the lasers had an output of approximately 9J each. This output energy was selected as a result of a trade-off between pulse-to-pulse stability of 3 lasers and total output energy. The pulse shape was monitored with a LTD-T05 pyroelectric detector manufactured by Carson Alexiou. Figure 3.6 is a representative trace of the detector output. We observe a spike and a tail of several μ sec duration. The laser energy was monitored with a 50D pyroelectric energy meter manufactured by Lumonics. The amplitude of the approximately 50 msec wide pulse is proportional to the laser pulse energy.

A four channel trigger generator was used to sequence the lasers. The delay generator could either be triggered internally by a variable delay timer or signal from an antenna. Both methods were used depending on the electronic circuit used to break the diaphragm. During the one atmosphere tests, the antenna was used and the signal came from the spark that broke the diaphragm. During the low pressure tests, i.e., 10^{-4} atm, the internal circuitry was used. One of the output channels was used to trigger a high voltage pulse to break the diaphragm. This technique was used because of the need for a short duration electrical pulse to eliminate glow discharge problems in the vacuum chamber.



Time —————
.5 μs / div

Fig. 3.6 Trace of Pyroelectric Detector Output.

3.6 Vacuum Chamber

Before performing experiments at reduced pressures, it is necessary to know the ambient pressure at which the cold propellant gas flow expands as if it were expanding in a total vacuum. For the conical nozzle of 24 cm length, calculations performed during one-dimensional isentropic relations show that for helium propellant ($p_0 \sim 3$ atm) the vacuum expansion is achieved when the ambient pressure is less than 6.5 microns. Under the same conditions with air as a propellant, vacuum expansion is achieved when the pressure is less than 30 microns. The difference between air and helium is a result of the specific heat ratio difference between a monatomic and diatomic gas. Background pressures slightly higher than these were used to keep the pump-down time reasonable for the $\sim 0.42 \text{ m}^3$ (15 ft³) chamber used. Therefore, oblique shocks existed at the exit plane. To illustrate the effect of background pressure, calculations were made of the propellant exit velocity as a function of the ambient pressure for steady-state helium flow through the conical nozzle with the plenum stagnation pressure of 3 atmospheres. For exit pressures greater than 5.4×10^{-3} atmosphere, a normal shock exists in the nozzle and the flow is initially supersonic and finally subsonic. In the ambient pressure range 5.4×10^{-3} atmosphere to 8.56×10^{-6} atmosphere, the helium flow is supersonic throughout the length of the nozzle and oblique shock waves exist at the exit plane. Since the theoretical analysis carried out in Section 2. and Ref. 8 is based upon the assumption that a supersonic flow is present throughout the length of the nozzle, it is best to perform experiments at ambient pressure less than 5.4×10^{-3} atmospheres to compare experimental and theoretical results.

A vacuum chamber assembly was designed and procured for performing laser propulsion experiments at these reduced background pressures. The chamber consists of a steel bell jar, 0.71m diameter and 1.2 m long, horizontally mounted on wheels which roll on a track. The bell jar was modified by adding two 10 cm diameter observation windows along the side. The laser beams pass through potassium chloride (KC1) windows mounted on an aluminum flange which forms the remaining side of the vacuum chamber. Three rectangular ports for visual/optical monitoring of the rocket and flanges for electrical feedthroughs were provided. Three rods attached to the large aluminum flange and a smaller flange attached to the rods were placed in the chamber to hold the optics and nozzle in the chamber. The chamber was evacuated with a mechanical vacuum pump so that a vacuum of $\leq 25 \mu$ could be obtained. Provision was also made to be able to backfill the chamber with a specific gas if desired.

4. EXPERIMENTAL RESULTS

The goal of the experimental program was to demonstrate the feasibility of the proposed pulsed laser powered thruster and achieve high specific impulse expected from this system. The theory, which has been discussed in Section 2, predicts the operating parameters which yield an I_{sp} of 1000 sec for both vacuum and finite back pressure operation. Experiments were performed with exit plane pressures ranging from 10^{-4} to 1 atm, and it will be seen that the desired specific impulse was obtained with approximately 50% energy conversion. Two rocket nozzle configurations were designed and tested - a conical nozzle with external optical focusing and a parabolic nozzle with internal focusing. The experiments will be discussed in chronological order. Conical nozzle experiments were performed at 1 atmosphere and parabolic experiments were performed at 1 to 10^{-4} atmospheres. The latex diaphragm was used in all the experiments separating the plenum from the nozzle. We will first discuss how long it takes for the helium propellant gas to fill the nozzle.

4.1 Propellant Flow Through the Nozzle

Since we are interested in shocking the propellant gas, it is first desirable to know the time it takes for the propellant gas to fill the nozzle. The gas pressure as a function of time was measured at two places downstream of the throat. The pressure-time history was obtained at one atmosphere ambient pressure using only the small conical nozzle. When the diaphragm bursts, a shock wave is produced. This shock wave arrives at the first transducer in 120 μ sec and at the second transducer in 170 μ sec. Thus, the diaphragm shock travels a distance of 1.5 cm in 50 μ sec, with an average shock velocity of 3×10^4 cm/sec.

If we assume strong shock relations, we find that the helium-air contact surface travels with a constant velocity which is 5/6th of the shock velocity. From this we can deduce the time it takes the helium to fill the nozzle to be 126 μ sec.

We can also obtain a rough estimate of the nozzle filling time by modeling the propellant flow through the nozzle as follows: we can assume the flow as one-dimensional flow in a constant area shock tube. In this case, the helium-air contact surface moves with a constant velocity which is 3/10th of the local sound speed and takes 132 μ sec to reach the exit plane. However, in a diverging nozzle the velocity of He-air contact surface does not remain constant but decreases downstream of the nozzle. Consequently, 132 μ sec should be considered as the lower bound on convection time for helium. Another estimate of the nozzle-filling time could be made if we assume that the flow in the nozzle is steady and isentropic as in Section 2.2. In this case helium fills the nozzle in 130 μ sec.

There is close agreement in the nozzle filling times deduced from the shock arrival time and from calculations performed using two different models. Therefore, it is proper to take 130 μ sec as the nozzle-filling time for time sequencing of the laser pulses.

4.2 Conical Nozzle Experiments

The first series of experiments were performed with short conical nozzle using helium propellant at 1 atmosphere background pressure. Up to two laser beams were focused at the nozzle throat with 30 cm focal length mirrors. The laser interpulse time was varied to obtain the dependence of I_{sp} on interpulse time with other parameters fixed.

The experimental arrangement is shown in Fig. 4.1. The primary diagnostic for the rocket performance was a ballistic pendulum to measure total impulse. This pendulum had a length of 3.35 m and a mass of 300 gm. The maximum deflection was recorded photographically and by observation. This was accomplished by illuminating a thin vertical wire attached to the rear of the rocket with a He-Ne laser beam. The specularly scattered light was magnified by a lens to obtain a 6.9 magnification of movement. The maximum displacement of the image was observed and also the length of the motion was recorded with an open shutter camera.

The rocket cold flow parameters were discussed in Section 3, and specifically for these experiments, the plenum conditions were $p_o = 2.93 \times 10^6$ dyne/cm², $T_o \sim 293^\circ K$, and $\rho_o = 4.9 \times 10^{-4}$ gm/cm³, with helium as the gas. Therefore, the choked flow mass flow rate with the 0.5 cm diameter throat is 5.4 gm/sec.

The sequence of events for the experiments were as follows:

1. Plenum pressurized and rocket installed on the pendulum;
2. Capacitor charged until the applied voltage broke the diaphragm;
3. Delay generator triggered by the EM wave from the electrical pulse breaking the diaphragm;
4. Diaphragm opened and helium flow commences;
5. First laser triggered 180 μ sec after event # 2;
6. Subsequent laser(s) triggered at specific interpulse times.

The trace illustrates the helium propellant induced wave followed by the much stronger laser pulse induced wave.

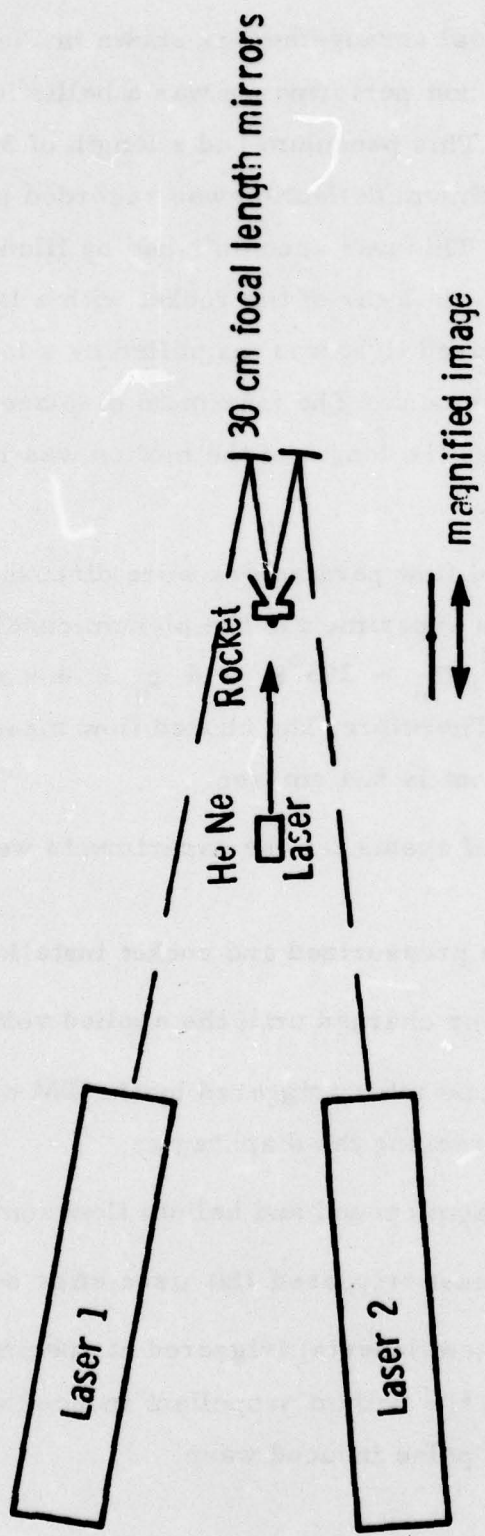


Fig. 4.1 Experimental Schematic, Conical Nozzle, $P_\infty = 1 \text{ atm}$.

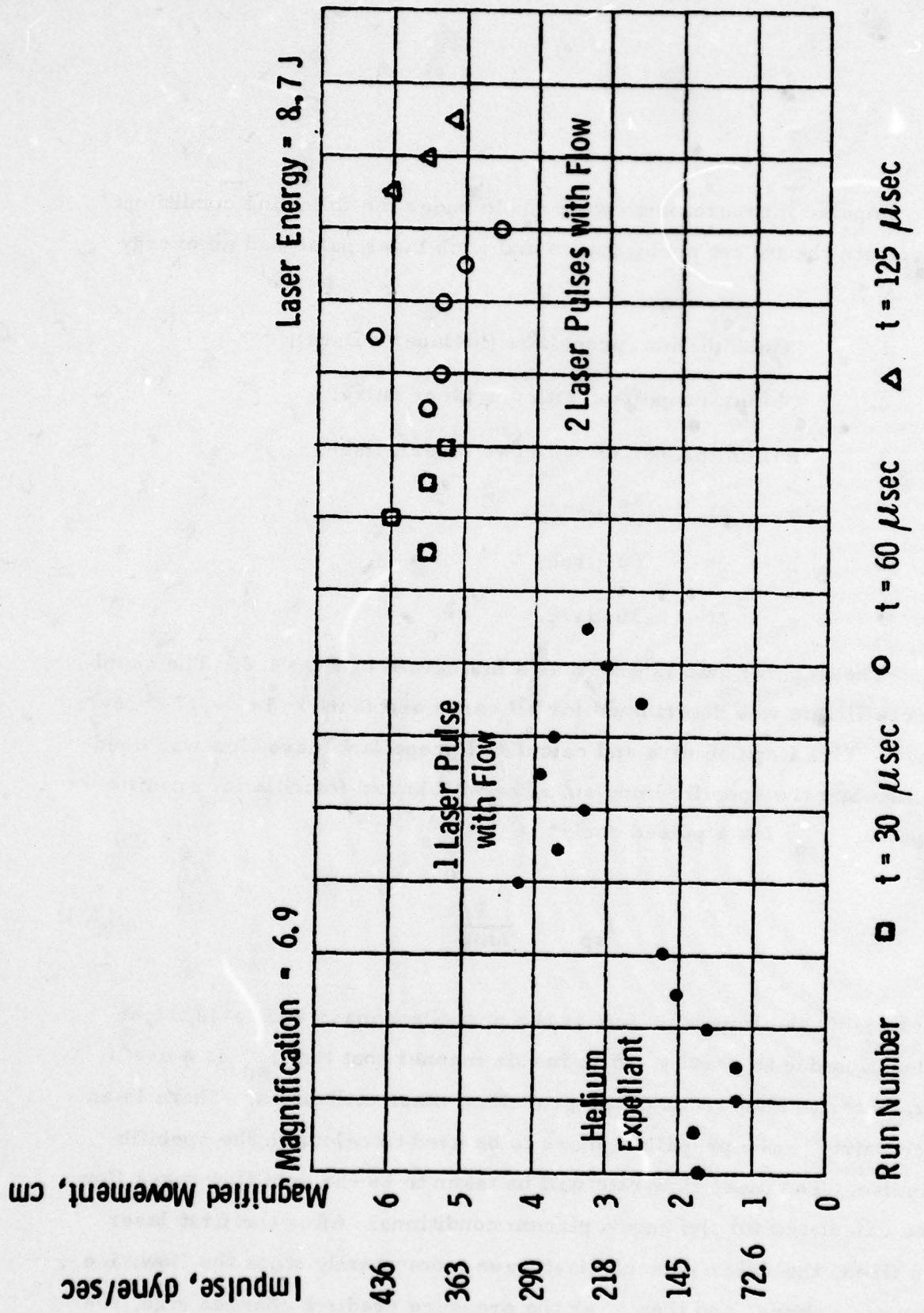
Impulse measurements were made under the following conditions to evaluate the rocket performance and each laser pulse had an energy of ~ 8.7 J:

1. "Cold" helium propellant (no laser pulses);
2. Helium propellant with one laser pulse;
3. Helium propellant with two laser pulses.
 - a. $\Delta t = 125 \mu\text{sec}$;
 - b. $\Delta t = 60 \mu\text{sec}$;
 - c. $\Delta t = 30 \mu\text{sec}$.

The impulse data is shown as a histogram in Fig. 4.2. The coupling coefficient was determined for all cases and found to be ~ 17 dyne-sec/J. This impulse data and calculated propellant mass flow was used to calculate the specific impulse. The well known formula for specific impulse, I_{sp} , for a pulsed rocket is

$$I_{sp} = \frac{I}{\Delta m g} \quad (4.1)$$

where I is the impulse, Δm is the propellant mass and g is the acceleration due to gravity. It is in this manner that the I_{sp} is a useful parameter to keep track of the propellant mass utilization. There is an uncertainty in the propellant mass to be used to calculate the specific impulse. The mass flow rate will be taken to be the cold flow mass flow rate calculated for the known plenum conditions. After the first laser has fired, the laser induced blast wave momentarily stops the flow, i.e., acoustic valving, and then after the pressure gradient changes sign, the



flow restarts. Therefore, an upper bound for the propellant mass introduced for the second pulse, Δm , is

$$\Delta m = \dot{m} \Delta t \quad (4.2)$$

where Δt is the time between pulses.

Using this formulation we can determine the specific impulse pertinent to the n^{th} pulse, $(I_{\text{sp}})_n$, by knowing the impulse due to $n - 1$ pulses, I_{n-1} , and n pulses, I_n , mass flow rate and time between pulses. Hence, we obtain the specific impulse for the n^{th} pulse to be

$$(I_{\text{sp}})_n = \frac{I_n - I_{n-1}}{\dot{m} \Delta t} \quad (4.3)$$

Using this formula, we reduced the data in Fig. 4.2 to obtain the specific impulse for the 2nd pulse and the results are given in Fig. 4.3. The circles represent the average values of the specific impulse calculated by

$$I = \frac{I_2 - I_1}{\dot{m} \Delta t} \quad (4.4)$$

The theoretical predictions using Eq. (2.13) for various assumed values of the energy conversion efficiency are shown for comparison with the conical nozzle data in Fig. 4.3. The error bars are determined using the best estimate of the standard deviation and the statistical formula for determining the standard deviation of the difference of two variable quantities is

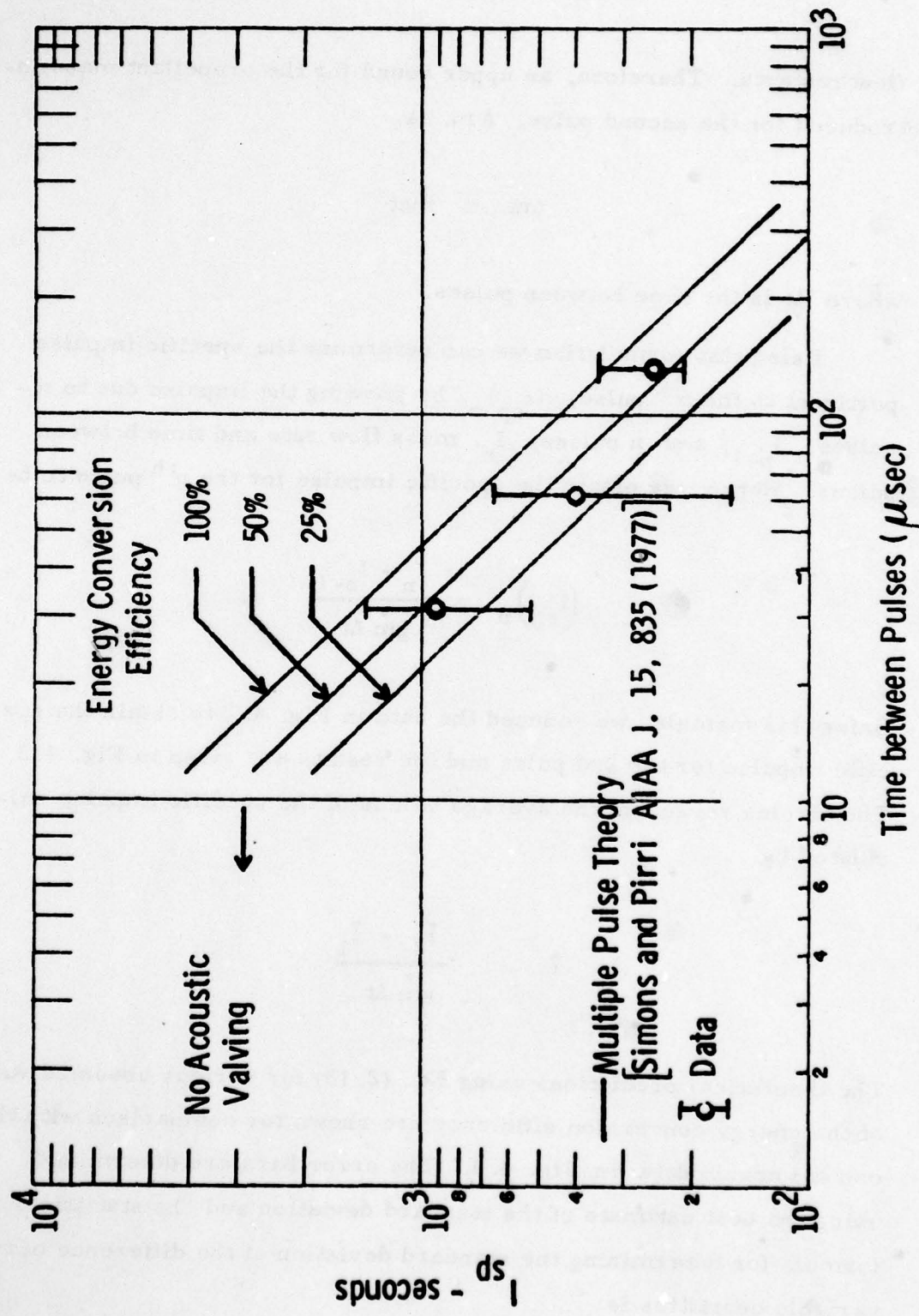


Fig. 4.3 Two Pulse Data with Conical Nozzle - One Atmosphere Background Pressure.

$$\sigma = \sqrt{\sigma_2^2 - \sigma_1^2} \quad (4.5)$$

where σ_2 is the standard deviation for double pulse experiments and σ_1 is the standard deviation for the single pulse experiments. Using Eq. (4.3) the 1σ error bars were determined for the I_{sp} data and are shown in Fig. 4.3. We note that even though the data is for independent experiments, the impulse for two pulses is not independent from the impulse due to one pulse. Specifically, if an experimental value of the impulse is higher than the average value for two pulses, it is likely that the impulse of the first pulse was also higher than the average impulse. Thus, this method accentuates the error bars but is used because it is fair representation of the data.

A detailed analysis has not been done to determine the sources of scatter in the data, but some comments can be made. The variations could have been caused by variations in laser pulse energy, laser breakdown induced blast waves - strength and location, and plenum conditions. The laser produced breakdowns have had variations in strength and location which would effect the rocket impulse. Cold flow propellant impulse measurements have produced variations in impulse. Because a fraction of the total impulse is due to the cold flow after the laser pulses are over, the cold flow impulse needs to be considered, (it is subtracted out in the data reduction process). The causes of this scatter could be variations in plenum pressure, changes in exit velocity/density time history, or slight differences in area ratio due to imperfect alignment of the plenum and nozzle.

These experiments have shown that an I_{sp} of ~ 1000 sec can be obtained with this laser powered thruster. In addition, the predicted dependence of I_{sp} on interpulse time correlates very well with theoretical predictions discussed in Section 2.

4.3 Parabolic Nozzle Experiments

The conical nozzle was used to compare the experimental results with theory. Because it is expected that a full-scale rocket will use a parabolic nozzle, experiments were done with a parabolic nozzle utilizing the same plenum and throat as the conical nozzle. These experiments ranged from one to three laser pulses and background pressures from one to 10^{-4} atmospheres (corresponding to altitudes from sea level to ~ 70 km). As the experimental results will show, the laser produced blast waves excited from the nozzle during the interpulse time for the 10^{-4} atm experiments, so no new phenomenology would be encountered if the background pressure had been reduced even further. Furthermore, because the pulses are independent, asymptotic performance was reached with only a few pulses, the results are independent of pulse number. The experiments will not be discussed in chronological order which is 1 atm, $1/5$ atm, and 10^{-4} atm.

4.3.1 Parabolic Experiments at One Atmosphere

The atmospheric background pressure experiments with parabolic nozzle used the same plenum chamber, pendulum and impulse recording techniques as the conical nozzle experiments. The characteristics of the parabolic nozzle were discussed in Section 3 (10.5 cm long and 7.2 cm exit diameter yielding an area ratio of 205).

The same experimental procedure was used as described in Section 4.2 with the exception that the delay between the spark breaking the diaphragm and the first laser firing was increased from 180 to 400 μ sec to ensure that the breakdown would occur in helium. However, this plenum did not have sufficient capacity to fill the entire parabola

with helium at 1 atm, so the rocket performance was for a mixture of helium and air. As described in Section 3, the plenum is capable of providing the necessary propellant mass for the vacuum tests because of the falloff of propellant density for the entire nozzle length.

The one atmospheric background pressure tests were performed to establish the initial feasibility of beam focusing using a parabolic nozzle and a learning experience before using the vacuum chamber. It was understood before the experiments were performed that the data would not be representative of full-scale operation at one atmosphere because the nozzle was designed for vacuum operation and was too large in volume yielding weak waves at the exit plane.

Data was taken as follows:

1. "Cold" helium propellant (no laser pulses);
2. Helium propellant with one laser pulse;
3. Helium propellant with multiple laser pulses (interpulse time \approx 32 μ sec)

Impulse data was obtained and is shown in Fig. 4.4. The impulse data can be used just as in the conical nozzle experiments to obtain a propellant specific impulse. It is noted that for these tests, much of the shocked gas leaving the parabola is air. Therefore, one needs to delineate between actual specific impulse and propellant specific impulse. They become equal when the rocket is operated for a long time, but not in the case for one or two pulses. It should be pointed out that the definition of fuel specific impulse is also used in detonation propulsion where the exhaust gases include shocked ambient gas as well as

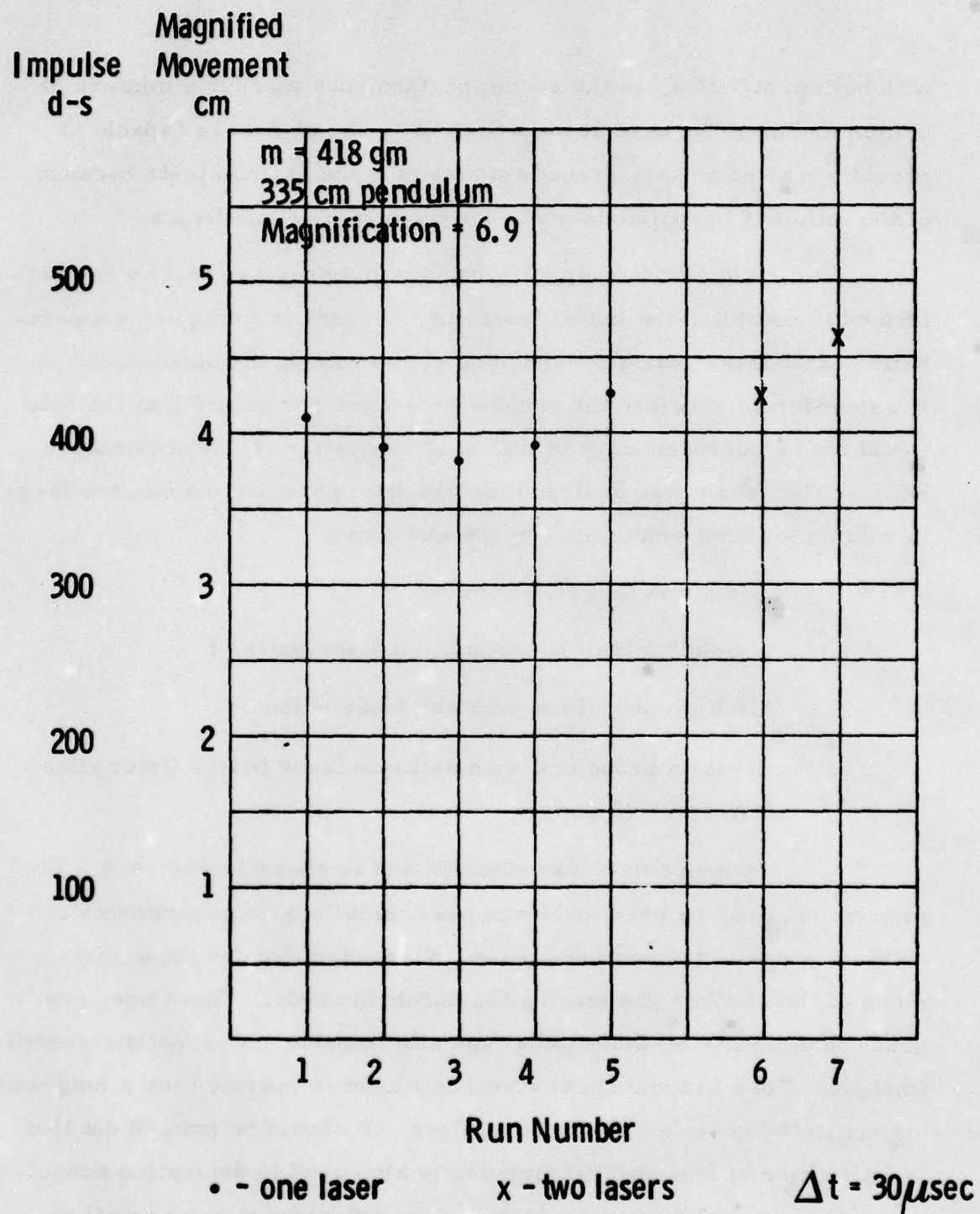


Fig. 4.4 Impulse Histogram.

products of the explosive.¹⁶⁻²⁰ The impulse data and calculated propellant flow yields an average value of I_{sp} of 256 sec for the second pulse, with an upper 1σ bound of 420 sec and lower 1σ bound of 110 sec.

4.3.2 Parabolic Experiments at 1/5 Atmosphere

When the vacuum chamber was ready for use, tests were performed at reduced pressure. The diaphragm still was being broken with the same technique of charging a 2.5 nfd capacitor until the latex was punctured. As expected, this technique would not work at all pressures because of glow discharge generation at lower pressures. Before a remedy was instituted, tests were performed at 1/5 atmospheric pressure.

The same procedure was used as discussed above with a 180 μ sec time delay between the spark breaking the diaphragm and the first laser firing. The following tests were performed:

1. Cold flow (no lasers);
2. One laser pulse with helium propellant;
3. Two laser pulses with helium propellant.

The impulse again was determined using a ballistic pendulum 45 cm in length. The impulse results are given in Fig. 4.5. This data was reduced to obtain the propellant specific impulse for the second pulse.

The result is that $I_{sp} = 1100$ sec and the coupling coefficient ratio of impulse to laser energy, was 34 d-s/J. These are not consistent numbers for steady operation because the conversion efficiency is greater than unity (in this case 2.4). This explicitly shows that the air within

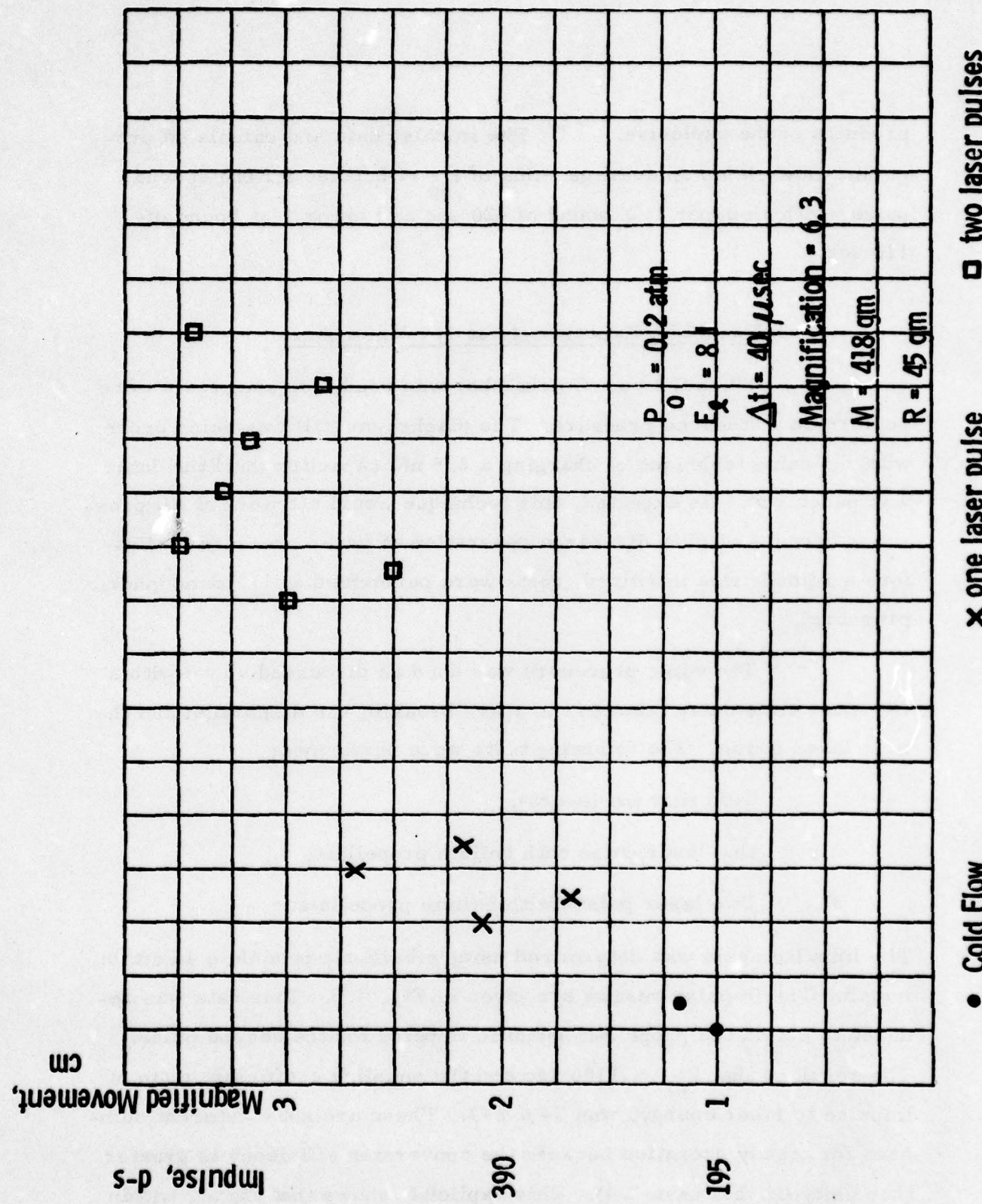


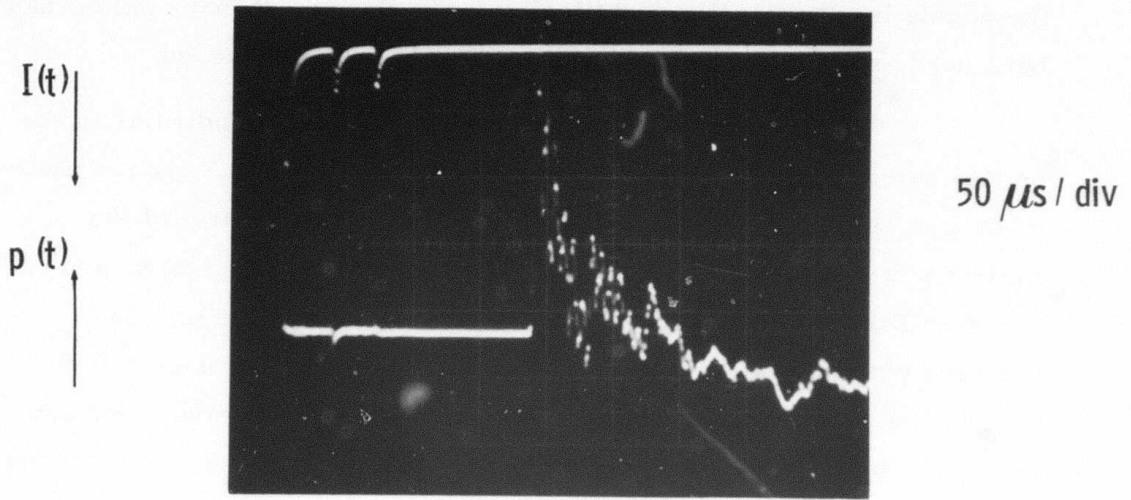
Fig. 4.5 Impulse Data Histogram.

the nozzle is significantly contributing to the thrust. If many pulses had been used, asymptotic performance would have been achieved.

A pressure transducer was mounted perpendicular to the optical axis after the above experiments had been done. A silicon photodiode was another diagnostic which monitored the laser breakdown radiation from the parabolic nozzle. Two representative traces are shown in Fig. 4. 6. Figure 4. 6a is for three laser pulses with the chamber evacuated to 1/5 atmosphere. We note the 180 μ sec transit time of the first wave which is propagating into some He and some air. Figure 4. 6b is for a case when the chamber was evacuated to 2 torr and backfilled with helium to 1/5 atmospheric pressure. Here the transit time is much less, illustrating the faster wave speeds that occur as expected in helium. Figure 4. 6a illustrates three laser pulses occurring before the processed gas reaches the exit plane and Fig. 4. 6b shows the first pressure pulse reaching the exit plane when the third laser fired. Because the laser induced wave had not reached the exit plane before the lasers ceased, asymptotic operation clearly has not been achieved with this number of laser pulses. To achieve asymptotic operation with a few laser pulses and also demonstrate operation at lower pressures corresponding to higher altitudes, tests at 10^{-4} atm were performed.

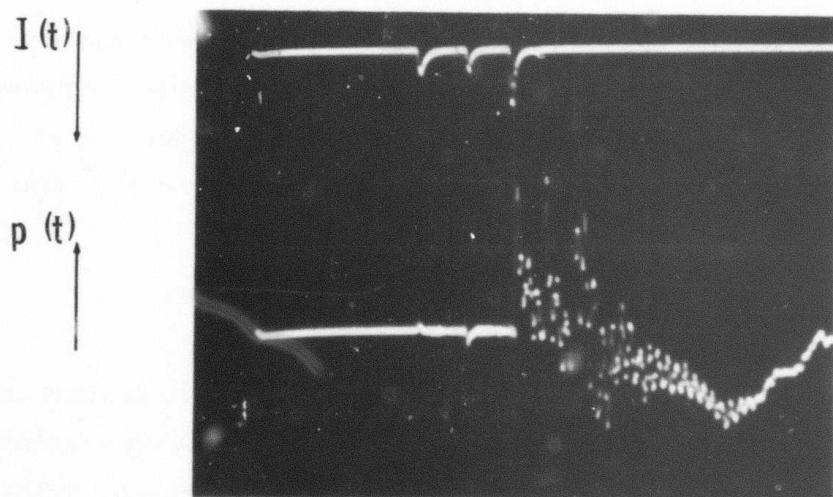
4. 3. 3 Parabolic Experiments at 10^{-4} Atmosphere

Data was taken at 1.6×10^{-4} atm pressure to demonstrate operation in a vacuum regime. The vacuum operation theory required a supersonic expansion of the cold propellant gas in the nozzle. This condition was met for our parabolic nozzle with an area ratio of 205 for pressures below 5×10^{-3} atmospheres. However, because the



1/5 atm air

Fig. 4.6 a Representative Pressure Transducer Trace.



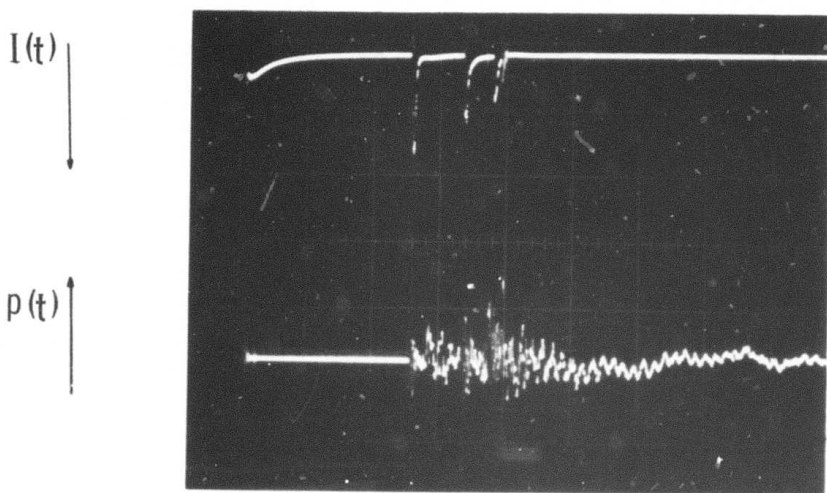
$t \longrightarrow 50 \mu\text{s} / \text{div}$

1/5 atm helium

Fig. 4.6 b Representative Pressure Transducer Trace.

transit time of a wave is longer than the interpulse time at this pressure, it is not certain that the rocket has achieved asymptotic performance for each pulse when only 2 or 3 pulses are used. This uncertainty can be eliminated by reducing the vacuum chamber pressure so that each pressure pulse exits from the nozzle before the next laser fires. In this manner the pulses are certain to be independent and asymptotic performance is obtained with a few pulses. The operating parameters for this to occur are dependent on both laser and rocket parameters and were experimentally achieved with the chamber pressure at 1.6×10^{-4} atm and a laser interpulse time of 35 μ sec. This behavior is demonstrated with pressure transducer data shown in Fig. 4.7. A pressure transducer was mounted parallel to the optical axis and off center so as to monitor the stagnation pressure of the exhaust gas but not block the laser beams. The other trace is the signal from a silicon photodiode monitoring the light from the laser produced breakdown. Because the pressure wave is detected before the second laser fired, the independence of the pulses has been demonstrated. The data will be discussed in more detail below.

The tests at 1.6×10^{-4} atm pressure again used helium propellant with a laser interpulse time of approximately 30 μ sec. Besides measuring the imparted impulse with a ballistic pendulum, measurements were made of the laser energy, interpulse time, optical radiation from the breakdown region and static and stagnation pressures. The optical radiation was monitored using a silicon photodiode which has a sensitivity from the UV to 1.1 microns. The signal was useful as a relative measure of the strength of the laser induced breakdown and the presence of propellant after each laser pulse. Two pressure transducers were mounted near the nozzle exit plane. One was mounted



50 μ sec / div

$t \longrightarrow$

$$p_{\infty} = 10^{-4} \text{ atm}$$

Fig. 4.7 Oscilloscope Trace.

perpendicular to the rocket axis to monitor static pressure and the other parallel to monitor the stagnation pressure.

Thirteen runs were made composed of three cold flow, three two-pulse and seven three-pulse. The impulse data showed very poor statistics because the cold flow impulse dominated the total impulse which had not been the case for the higher pressure tests. The cold flow impulse increases as the background pressure is reduced due to the increasing exit velocity with decreasing background pressure. Because the requirement of relatively constant plenum condition needs to be met, one solution is to reduce the exit plane velocity of supersonic cold propellant. This can be done by using a higher molecular weight propellant gas. This was not tried in the present program because a study of different propellants was beyond the scope of the program. Because the scatter in the impulse data was greater than the added impulse of the third laser pulse, technique of computing I_{sp} from impulse measurements and propellant mass flow could not be used to provide accurate data. Therefore, the pressure transducer data was used to calculate the exhaust velocity, and, thus, the specific impulse.

An average propellant velocity was calculated using measurements of the transit time of the propellant wave over the measured distance from the focus of the nozzle to the transducer. The vacuum theory was used to compare the average velocity to the exit velocity for our experimental conditions and it was found that these velocities are identical, i.e., within 5%. Therefore, the deduced wave velocity will yield the I_{sp} because the exhaust pressure times the exit area term in the thrust equation is small compared to the propellant momentum term for our experiments.

The average transit time for the second pulse was 20.5 μ sec with a maximum of 30 μ sec and a minimum of 15 μ sec. The average transit time for the third pulse was 25 μ sec with a maximum of 15 μ sec and a minimum of 10 μ sec. The above transit times and the eleven centimeter distance from the focus to the transducer yields an average specific impulse of 540 sec for the second pulse with an average laser energy of 7.9 J and an average specific impulse of 440 sec for the third pulse with an average laser energy of 7.3 J. Because the average laser energy was lower for the third pulse, it is expected that average specific impulse would be lower for the third pulse compared to the second pulse.

Not only the transit time measurements but also the magnitude of the stagnation pressure along with a model will yield an approximation of I_{sp} . Because the static pressure is more than an order of magnitude smaller than the stagnation pressure, the stagnation pressure p_s is

$$p_s \approx \frac{1}{2} \rho_e u_e^2 \quad (4.6)$$

where ρ_e is the density and u_e is the gas velocity at the exit plane. Using the measurement of p_s and a calculated density at the transducer location, the exhaust velocity can be calculated. The density was calculated using the theoretical profile for a conical nozzle, the calculated propellant mass, and nozzle length.⁸ A new theory for a parabolic nozzle was out of the scope of this program. A linearly increasing density with axial distance to the wave-front is appropriate for our case of using helium, ($\gamma = 1.67$), and we will assume this density field does not change after breakthrough. The density at the wave front can be calculated using the

calculated mass per laser pulse and the solid angle of the rocket. A solid angle of 0.032 ster rad was calculated from the exit area and nozzle length. The formula for the density at the wave front, ρ_e , is

$$\rho_e = \frac{4m}{r^3 \Omega} \quad (4.7)$$

where m is the propellant mass, r is the distance from the focus, and Ω is the solid angle of the gas expansion. Specific to our experimental conditions of 30 μ sec between pulses, we find that

$$\rho_e \approx 2 \times 10^{-6} \text{ gm/cm}^3.$$

The measurements of the stagnation pressure ranged from 3×10^5 to 7×10^5 dynes/cm². Using Eq. (4.6), we find that the exhaust velocity ranges from 5.5×10^5 to 8.4×10^5 cm/s yielding an I_{sp} of 550 to 840 sec. These values fall within the error bars of specific impulse calculated from transit time data.

The deduced specific impulse for all the parabolic experiments is plotted in Fig. 4.8 as a function of background pressure. Theory lines are also provided. It is clear that only the 10^{-4} atm experimental results compared closely with the theory. Both the $1/5$ and 1 atm experimental conditions, i.e., two pulses, were not representative of asymptotic performance so it is expected that there would be disagreement between theory and experiments.

The experimental and theoretical results presented above have demonstrated that 1) the PSI pulsed laser-powered thruster is a working concept; 2) a 500-1000 sec specific impulse can be obtained;

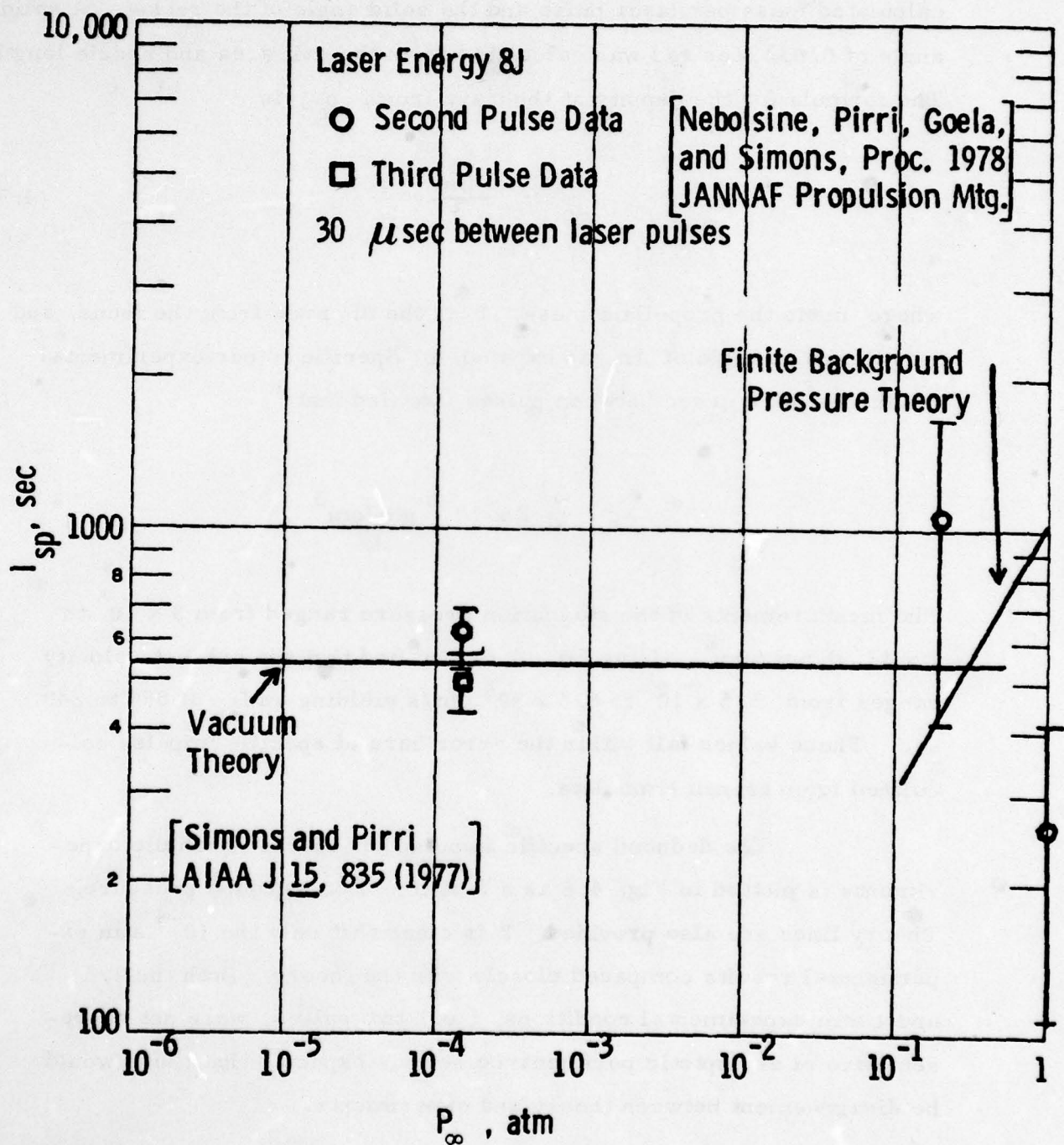


Fig. 4.8 I_{sp} vs. Background Pressure with Parabolic Nozzle.

3) gaseous propellant feed systems are reliable for self-regulating propellant flow; and, 4) parabolic nozzle focusing yields a strong laser breakdown in the propellant and significant thrust to laser power ratio.

4.4 Pressure Transducer Data Interpretation

In the Appendix it is shown that it is difficult to determine the flow velocity using a velocity diagnostic in the multiple pulse experiments. In Section 4.3 we discussed, briefly, how the pressure transducer data was used to determine the specific impulse in the parabolic nozzle experiments. In this section, the techniques for determining additional gas properties using the transducer data and blast wave theory, are presented. The pressure-time history at the short conical nozzle exit plane can give us information which can be used to deduce the flow velocity for the tests at 1 atm. An LD-80 (Celestec Transducer Products Inc.) pressure transducer was used at the nozzle exit plane to obtain pressure-time history as shown in Fig. 4.9.

Let R_s be the distance of the pressure transducer from a virtual blast wave source, p_{s1} be the pressure measured and t_{s1} be the blast wave arrival time at the transducer. From blast wave calculations, we obtain

$$R_{s1} = \xi_o \left(\frac{E}{\rho_o} \right)^{1/5} \left(\frac{4\pi}{\Omega} \right)^{1/5} t_{s1}^{2/5} \quad (4.8)$$

$$P_{s1} = \frac{8}{25(\gamma+1)} \xi_o^5 E \left(\frac{4\pi}{\Omega} \right) R_{s1}^{-3} \quad (4.9)$$

$$D = \frac{2}{5} \xi_o^{5/2} \left(\frac{E}{\rho_o} \right)^{1/2} \left(\frac{4\pi}{\Omega} \right)^{1/2} R_{s1}^{-3/2} \quad (4.10)$$

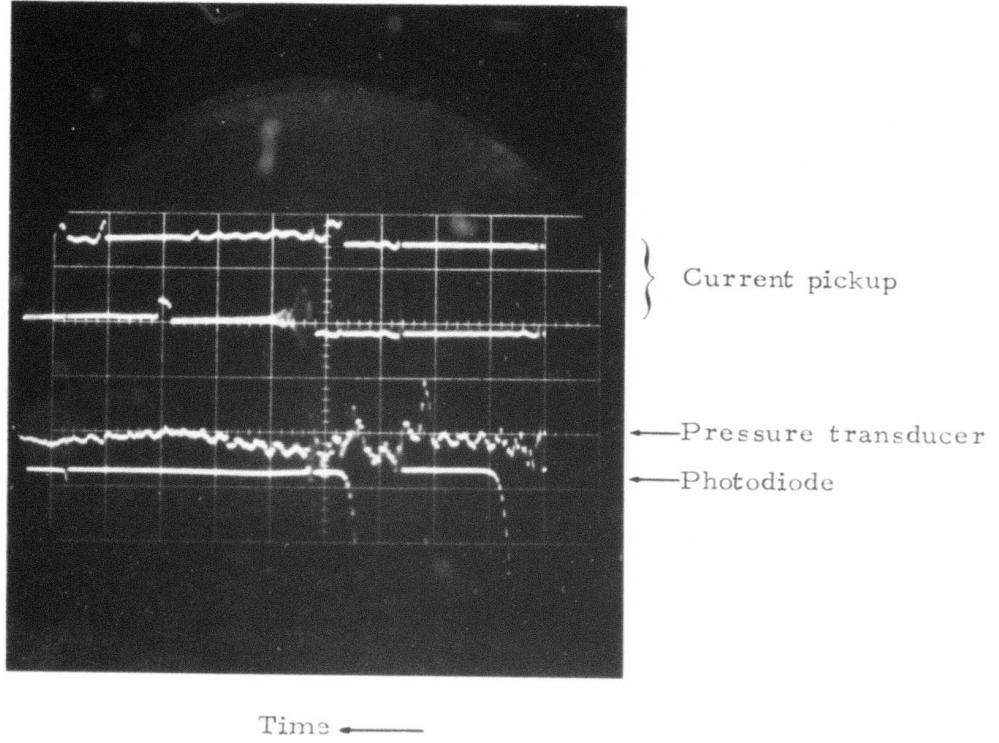


Fig. 4.9 Oscilloscope Trace.

$$U_1 = \frac{2}{\gamma + 1} D \quad (4.11)$$

where D is the blast wave velocity, U_1 , the velocity of the gas just behind the blast wave, E is the energy, ρ_o is the density and Ω is the solid angle of the nozzle. From Eqs. (4.8) - (4.11), we can deduce the blast wave energy, the density and exit velocity of the flow as follows:

Exit Velocity (u_e)

$$u_e = \left(\frac{R_e}{R_{s_1}} \right)^{-3/2} U_1 .$$

Using Eqs. (4.8), (4.10) and (4.11) we get

$$u_e = \left(\frac{R_e}{R_{s_1}} \right)^{-3/2} U_1 = \frac{4}{5(\gamma + 1)} \left(\frac{R_{s_1}}{R_e} \right)^{-3/2} \left(\frac{R_{s_1}}{t s_1} \right) . \quad (4.12)$$

Blast Wave Energy (E)

From Eq. (4.9) we can calculate E

$$E = \frac{25(\gamma + 1)}{8\xi_o^5} R_{s_1}^3 \left(\frac{\Omega}{4\pi} \right) p_{s_1} . \quad (4.13)$$

Gas Density (ρ_o)

From Eq. (4.8) we can calculate (E/ρ_o)

$$\frac{E}{\rho_o} = \frac{\frac{R}{\rho_o} s_1^5}{\frac{5}{2} t_{s_1}^5} \left(\frac{\Omega}{4\pi} \right) .$$

Using Eq. (4.13) for E , ρ_o can be determined

$$\rho_o = \frac{25(\gamma + 1)}{8} p_{s_1} \left(\frac{t_{s_1}}{R s_1} \right)^2 . \quad (4.14)$$

Specific Impulse (I_{sp})

The specific impulse is defined as the thrust per unit weight flow rate. The thrust T is given as

$$T = \rho_e A_e u_e^2 + (p_e - p_o) A_e g \quad (4.15)$$

where the subscript e refers to the nozzle exit plane and p_o is the ambient pressure.

$$\therefore I_{sp} = \frac{T}{mg} = \frac{u_e}{g} + \frac{(p_e - p_o)}{mg} A_e . \quad (4.16)$$

The thrust T is a function of time. Consequently, I_{sp} in Eq. (5.9) is the instantaneous specific impulse. However, since most of the mass is near the blast wave, I_{sp} in Eq. (4.16) is also the average specific impulse. The mass flow rate \dot{m} is given as

$$\dot{m} = \rho_e A_c u_e .$$

Just after the shock

$$\rho_e = \rho_1 = \rho_o \left(\frac{\gamma + 1}{\gamma - 1} \right)$$

$$\frac{p_e}{p_{s_1}} = \left(\frac{R_{s_1}}{R_e} \right)^3$$

Using Eq. (4.14) we get

$$\frac{(p_e - p_o) A}{\dot{m}} = \frac{2}{5} \left(\frac{\gamma - 1}{\gamma + 1} \right) \frac{R_{s_1}^{5/2}}{R_e^{3/2} t_{s_1} g} - \frac{2}{5} \left(\frac{\gamma - 1}{\gamma + 1} \right) \frac{p_o}{p_{s_1}} \frac{R_e^{3/2}}{R_{s_1}^{1/2} t_{s_1} g} . \quad (4.17)$$

The last term on the right hand side in Eq. (4.17) is a contribution due to the ambient pressure which is neglected in the blast wave theory. Since

$p_e/p_o \geq 5$, this contribution due to p_o is also neglected in the calculation of the specific impulse. Therefore, from Eqs. (4.12) and (4.17) we get

$$I_{sp} = \frac{4}{5(\gamma + 1)g} \left(\frac{R_s}{R_e} \right)^{-3/2} \left(\frac{R_s}{t_s} \right) + \frac{2}{5} \left(\frac{\gamma - 1}{\gamma + 1} \right) \frac{R_s^{5/2}}{R_e^{3/2} t_s g}. \quad (4.18)$$

Two laser pulses of 8.7 Joules energy were focused at the throat of the small conical nozzle. With the plenum pressurized to 28 psig with helium, pressure transducer measurements were made in one atmosphere ambient pressure. The results of these measurements are presented in Figs. 4.10 - 4.12. In Fig. 4.10, we show the blast wave energy for eight different tests. For both laser pulses the ratio of blast wave energy to laser energy yields energy conversion efficiencies of the order of 50%. This is in agreement with the comparison of theoretical and experimental results shown in Fig. 4.3.

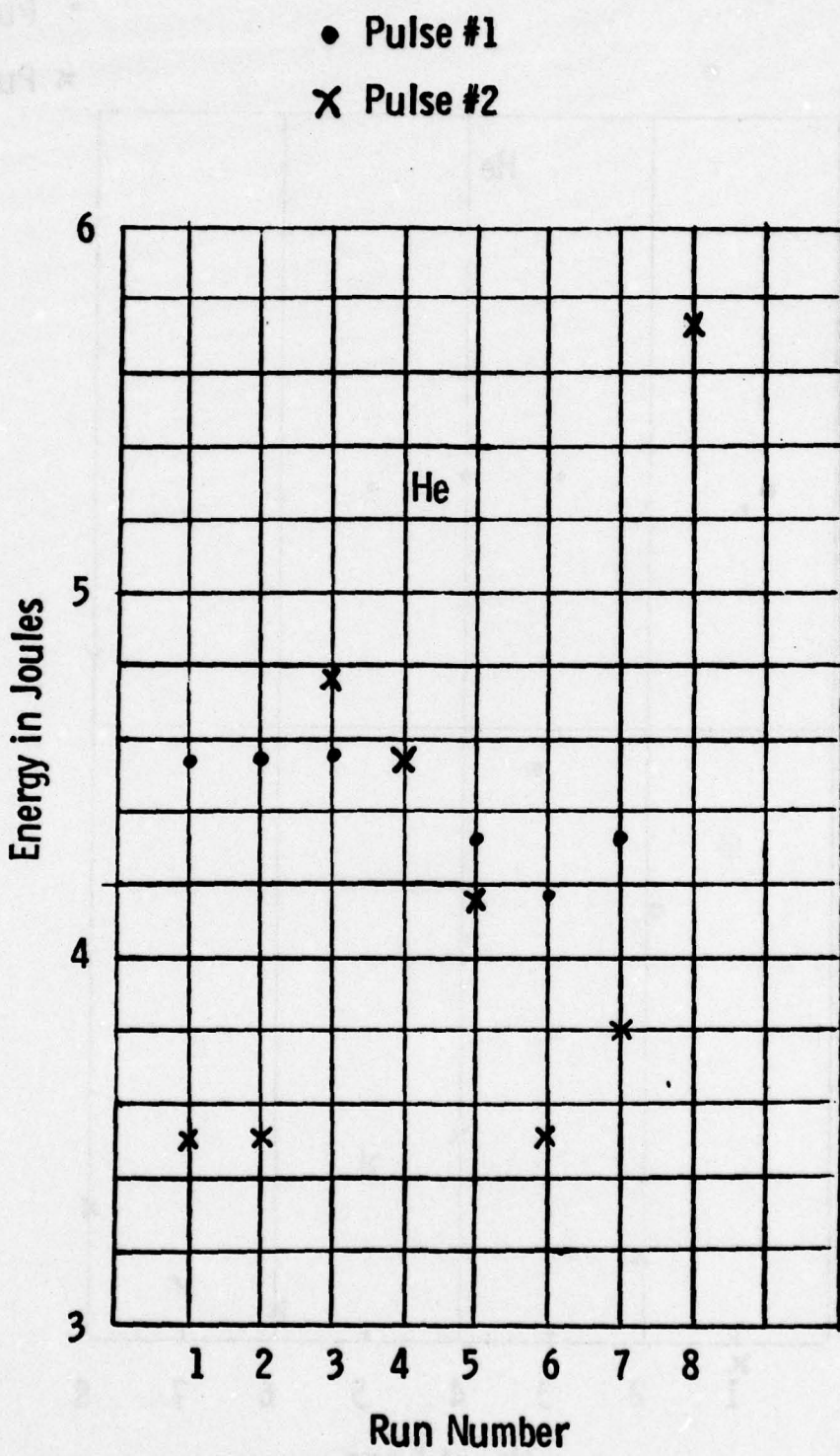


Fig. 4.10 Deduced Blast Wave Energy.

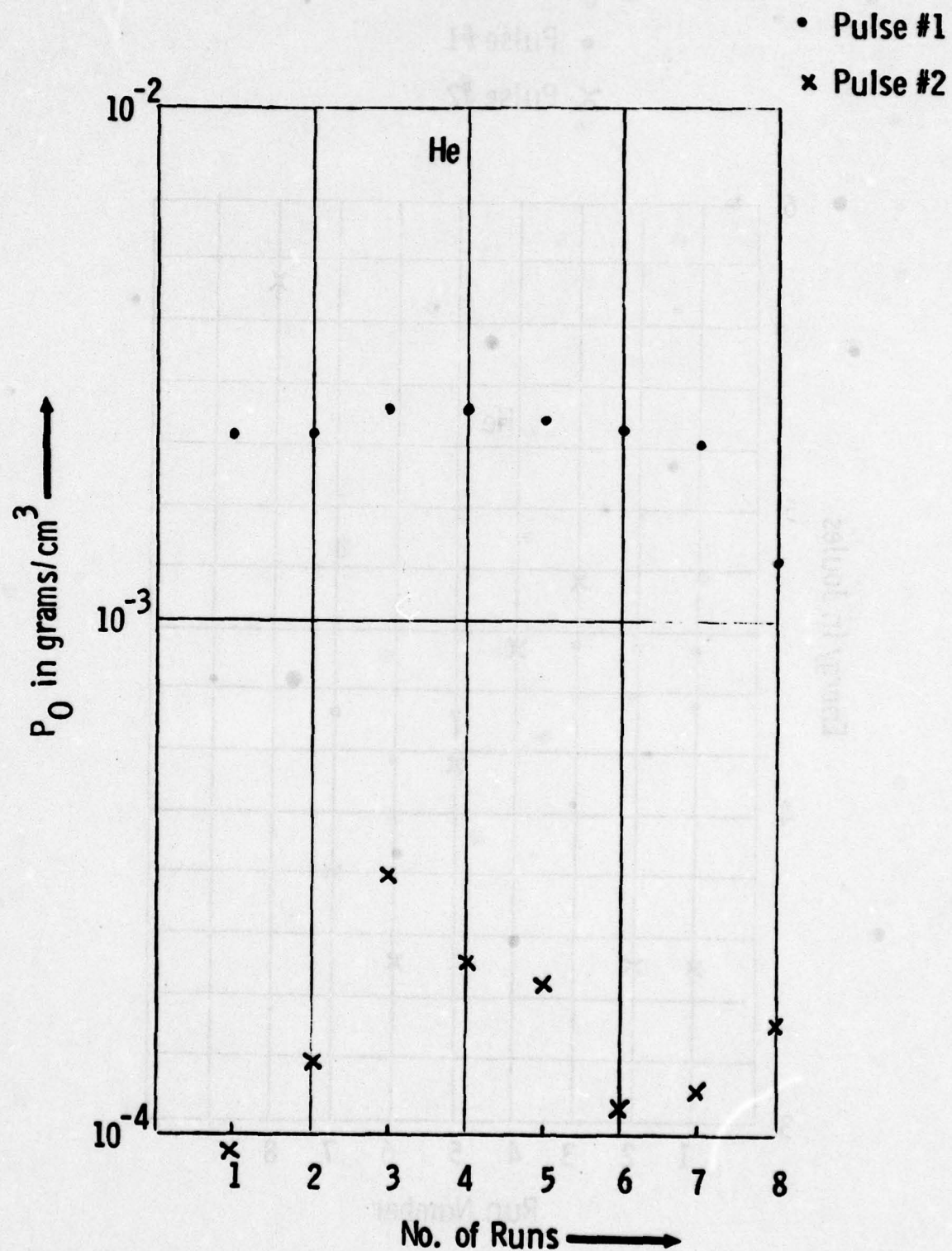


Fig. 4.11 Deduced Helium Density.

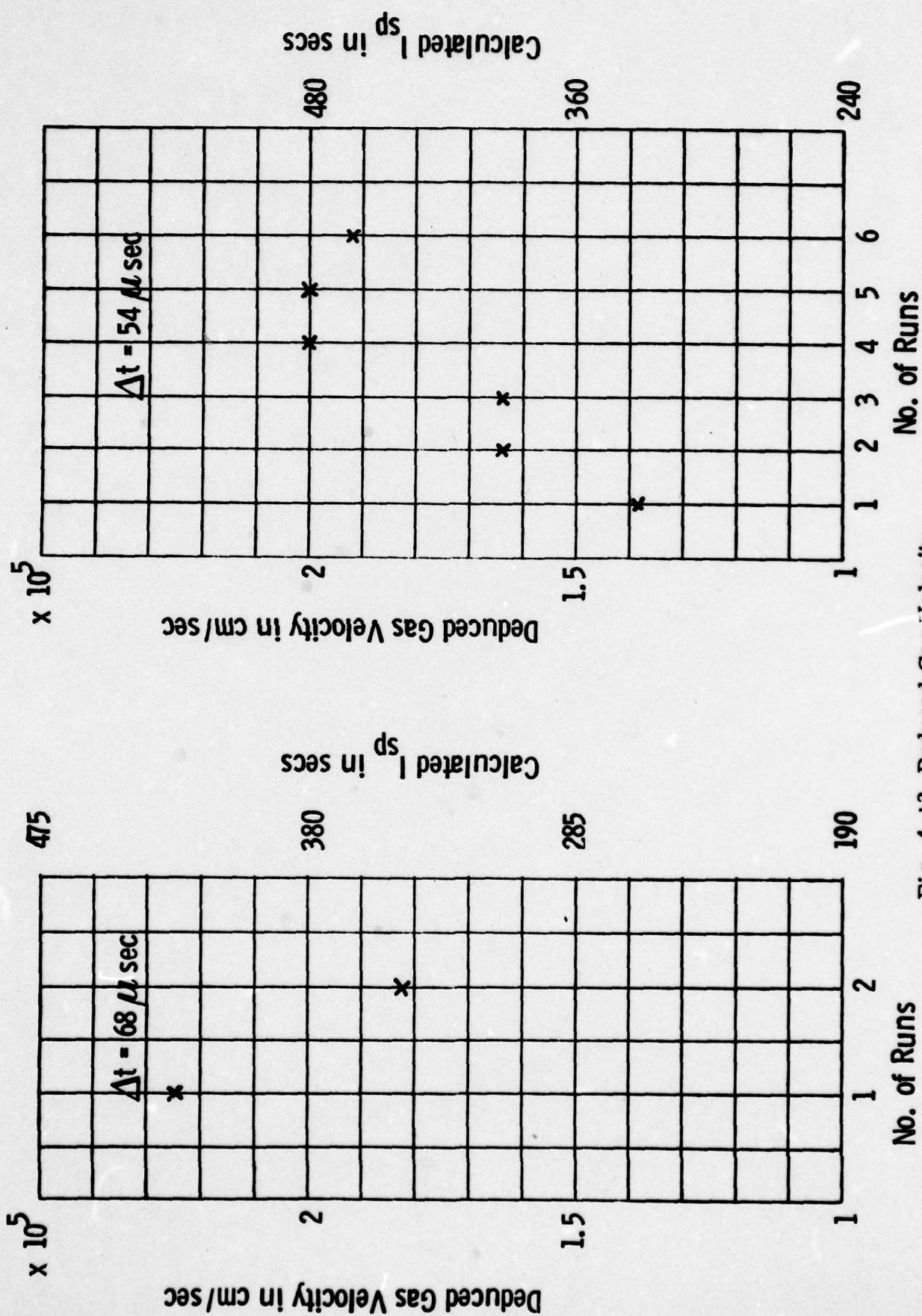


Fig. 4.12 Deduced Gas Velocity.

5. SCALING LAWS FOR EXPERIMENTS AT INCREASED LASER ENERGY

5.1 Laser Energy and REP Rate Requirements

To illustrate the results for finite p_∞ and design experiments over a wide range of parameter space, we restrict the propellant to helium at 3 atm pressure and 300°K. The nozzle is a 15° conical nozzle designed for an I_{sp} of 1,000 seconds at 50% energy conversion efficiency. The required pulse repetition frequencies and nozzle lengths are obtained as functions of orifice diameter, pulse repetition frequency, $1/\Delta t$, and ambient pressure. The restraints on the system are that Δt must exceed t_{blast}^* and D^*/u^* to assure acoustic valving and p_∞ must be sufficiently high to retain the interior shock (Fig. 2.4) well inside the nozzle. When p_∞ is reduced to a level where the shock moves outside the nozzle exit plane, the vacuum results for finite length nozzles are appropriate.

Operating maps have been developed as outlined above and are illustrated in Figs. 5.1 - 5.4. The independent variable is D^* which, for choked flow and $I_{sp} = 1,000$ sec, is related to thrust (T) by

$$T = \frac{\pi}{4} \rho^* u^* D^* I_{sp}^2$$

Each map corresponds to a different p_∞ and illustrates the laser energies, nozzle lengths and pulse repetition frequencies necessary to achieve 1,000 seconds. It is noted that the system parameters are very sensitive to the choice of p_∞ and one could initially question the possibility of designing a

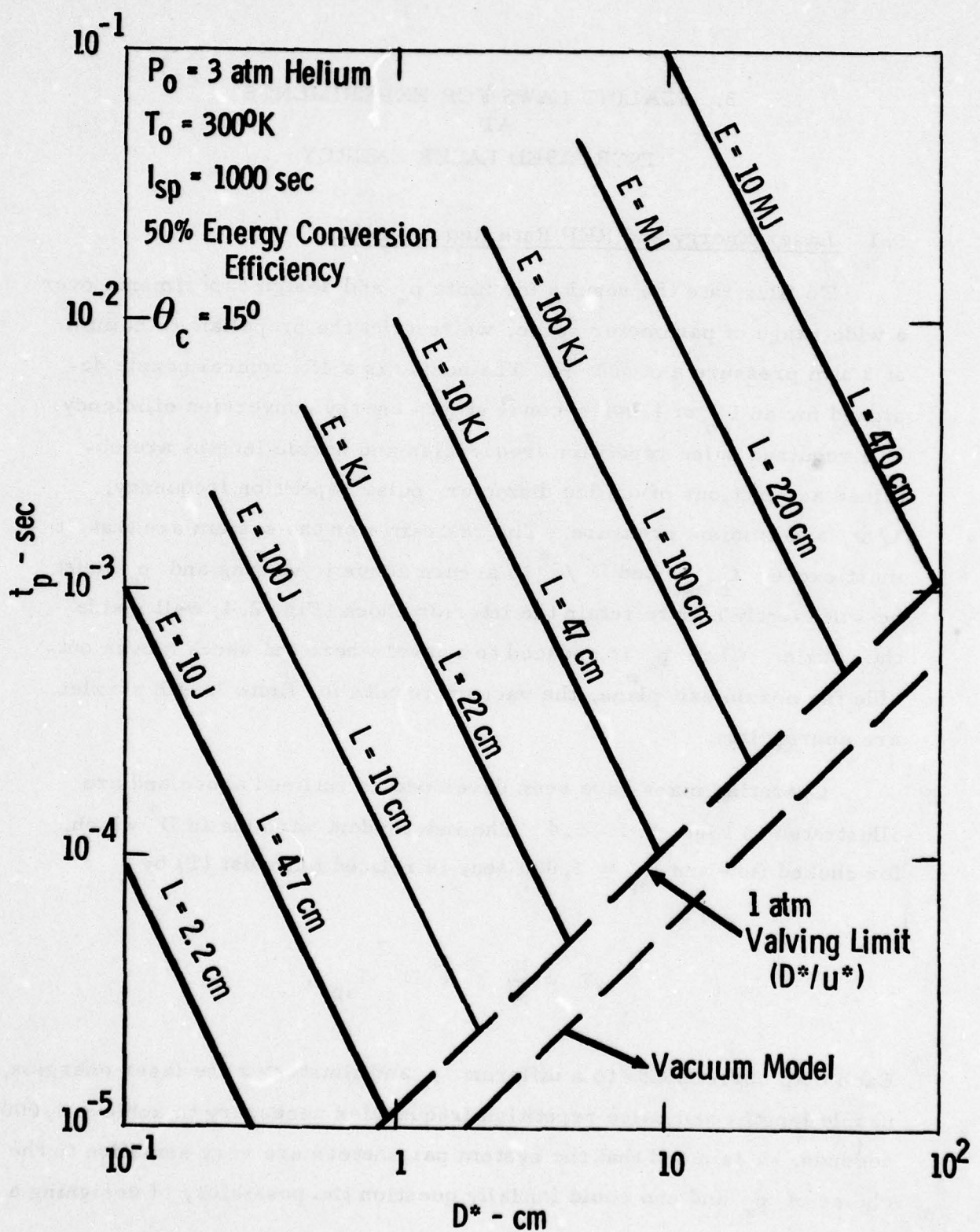


Fig. 5.1 Laser Energy Requirements - 1 atm Operation.

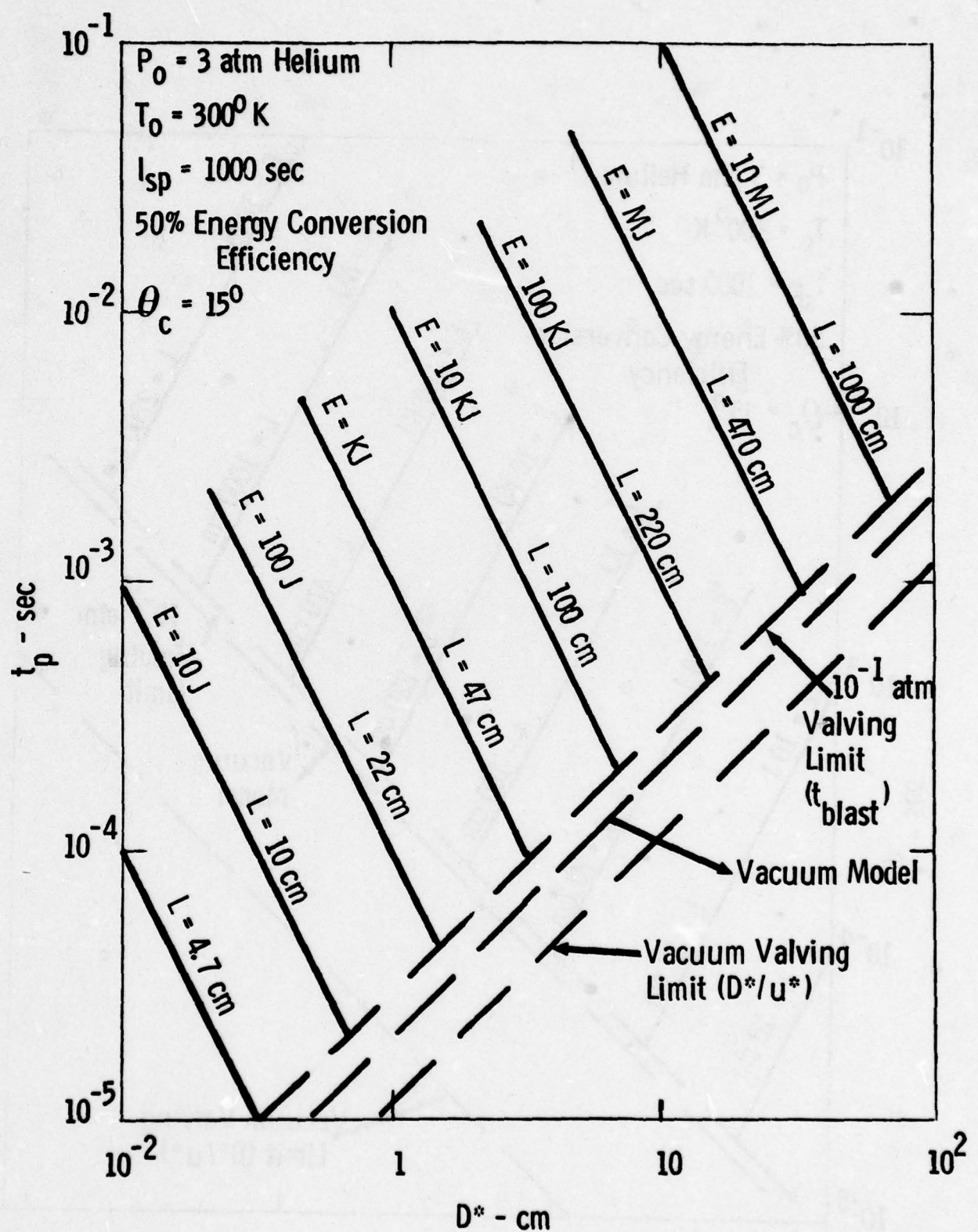


Fig. 5.2 Laser Energy Requirements - 10^{-1} atm Operation.

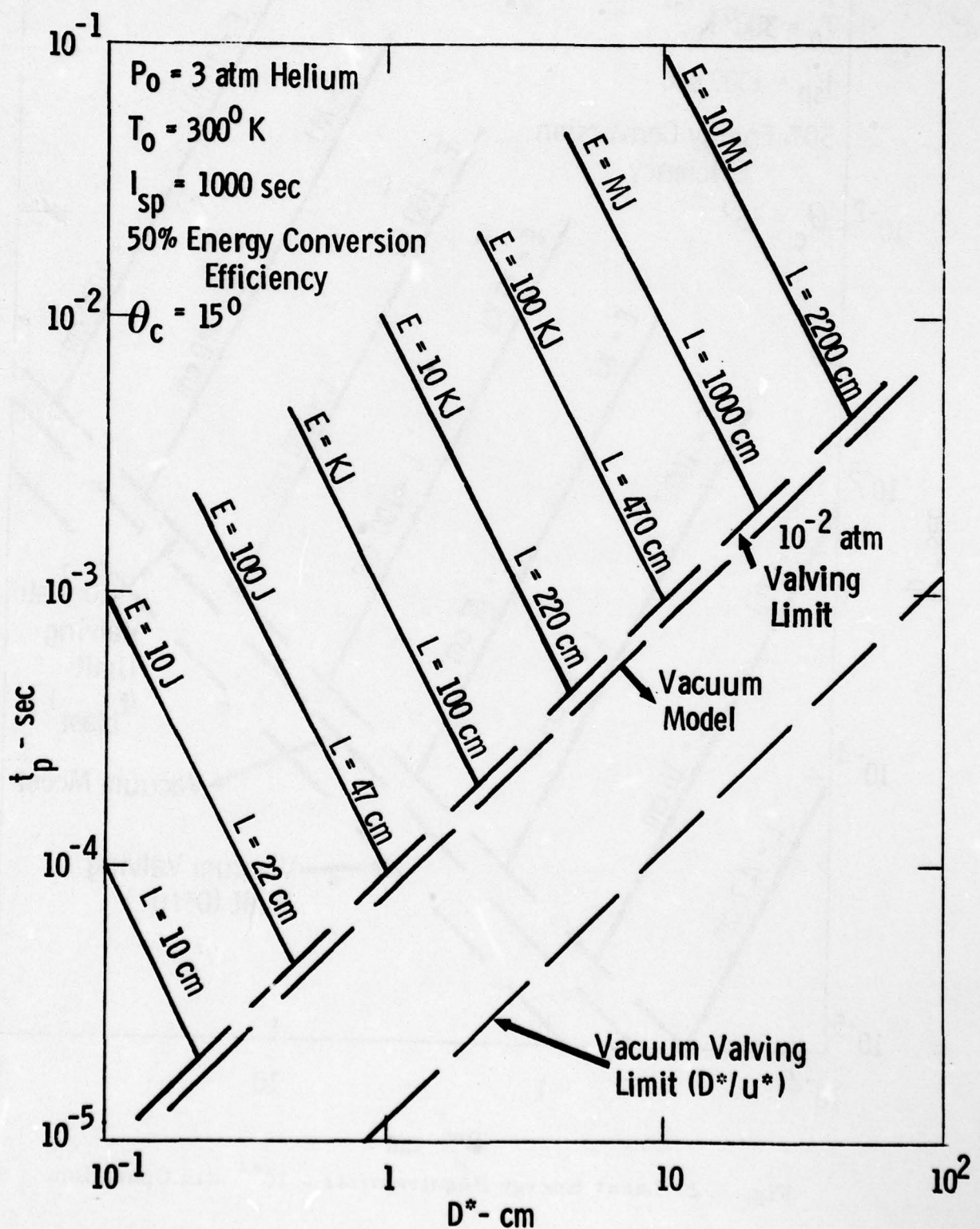


Fig. 5.3 Laser Energy Requirements - 10^{-2} atm Operation.

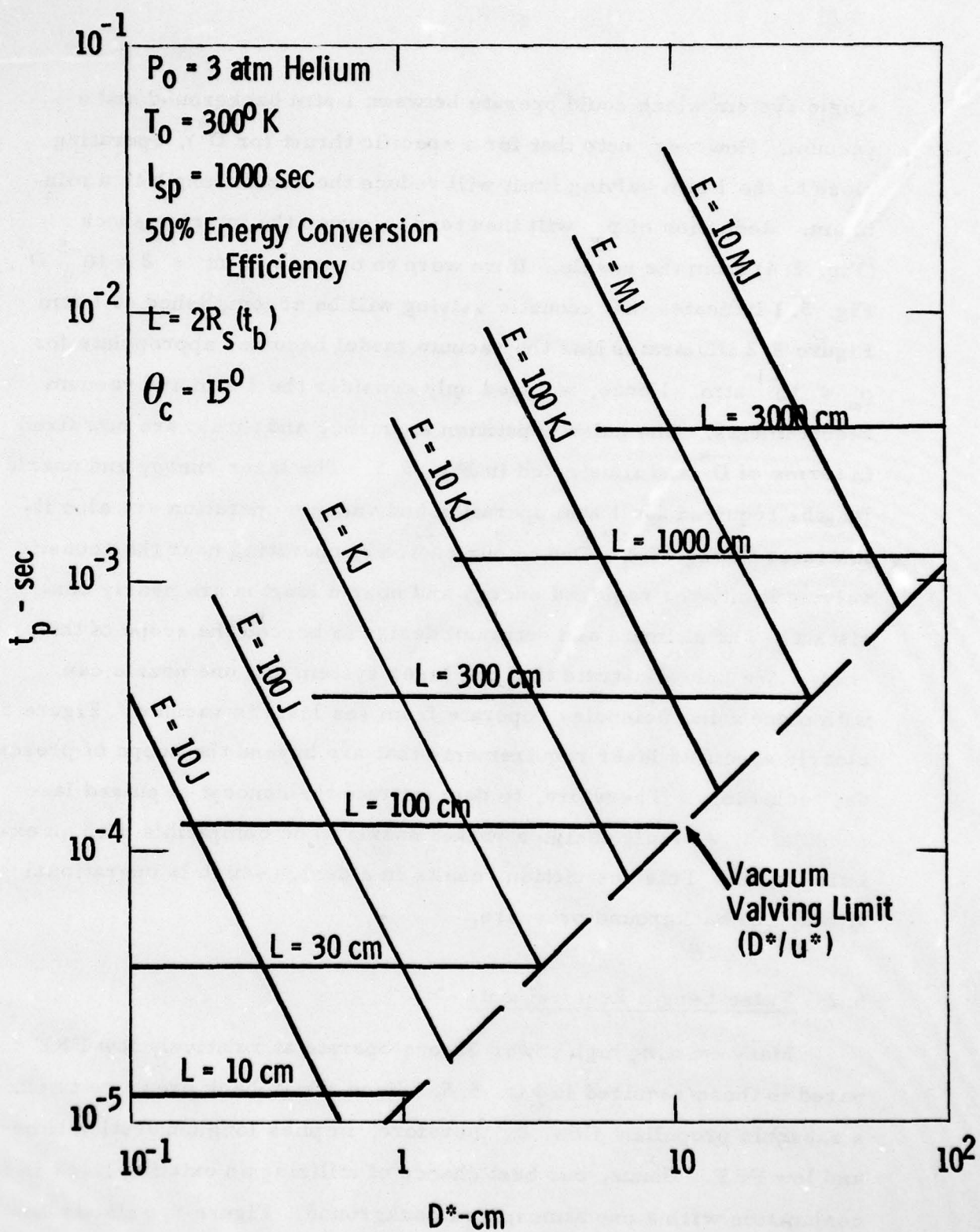


Fig. 5.4 Laser Energy Requirements - Vacuum Operation.

single system which could operate between 1 atm background and a vacuum. However, note that for a specific thrust (or D^*), operating close to the 1 atm valving limit will reduce the nozzle length to a minimum. Reduction of p_∞ will then tend to sweep the interior shock (Fig. 2.4) from the nozzle. If we were to operate at $\Delta t = 2 \times 10^{-5} D^*$, Fig. 5.1 indicates that acoustic valving will be accomplished at 1 atm. Figure 5.2 illustrates that the vacuum model becomes appropriate for $p_\infty < 10^{-1}$ atm. Hence, we need only consider the 1 atm and vacuum requirements. The pulse repetition frequency and thrust are now fixed in terms of D^* and illustrated in Fig. 5.5. The laser energy and nozzle lengths required for 1 atm operation and vacuum operation are also illustrated in Fig. 5.5. Due to our choice of operating near the acoustic valving limit, the required energy and nozzle lengths are nearly constant. The ultimate and optimum design is beyond the scope of this study. We only illustrate that one laser system and one nozzle can, with modest inefficiencies, operate from sea level to vacuum. Figure 5.5 clearly specified laser requirements that are beyond the scope of present day technology. Therefore, to demonstrate the concept of pulsed laser propulsion, we must design a rocket nozzle to be compatible with an existing laser. This restriction results in a design which is operational at only one background pressure.

5.2 Pulse Length Requirements

Many existing high power lasers operate at relatively low PRF compared to those required in Fig. 5.5. Since a high back pressure implies a subsonic propellant flow, it, therefore, implies long convection times and low PRF. Hence, our best chance of utilizing an existing laser is in conjunction with a one atmosphere background. Figure 5.6 illustrates

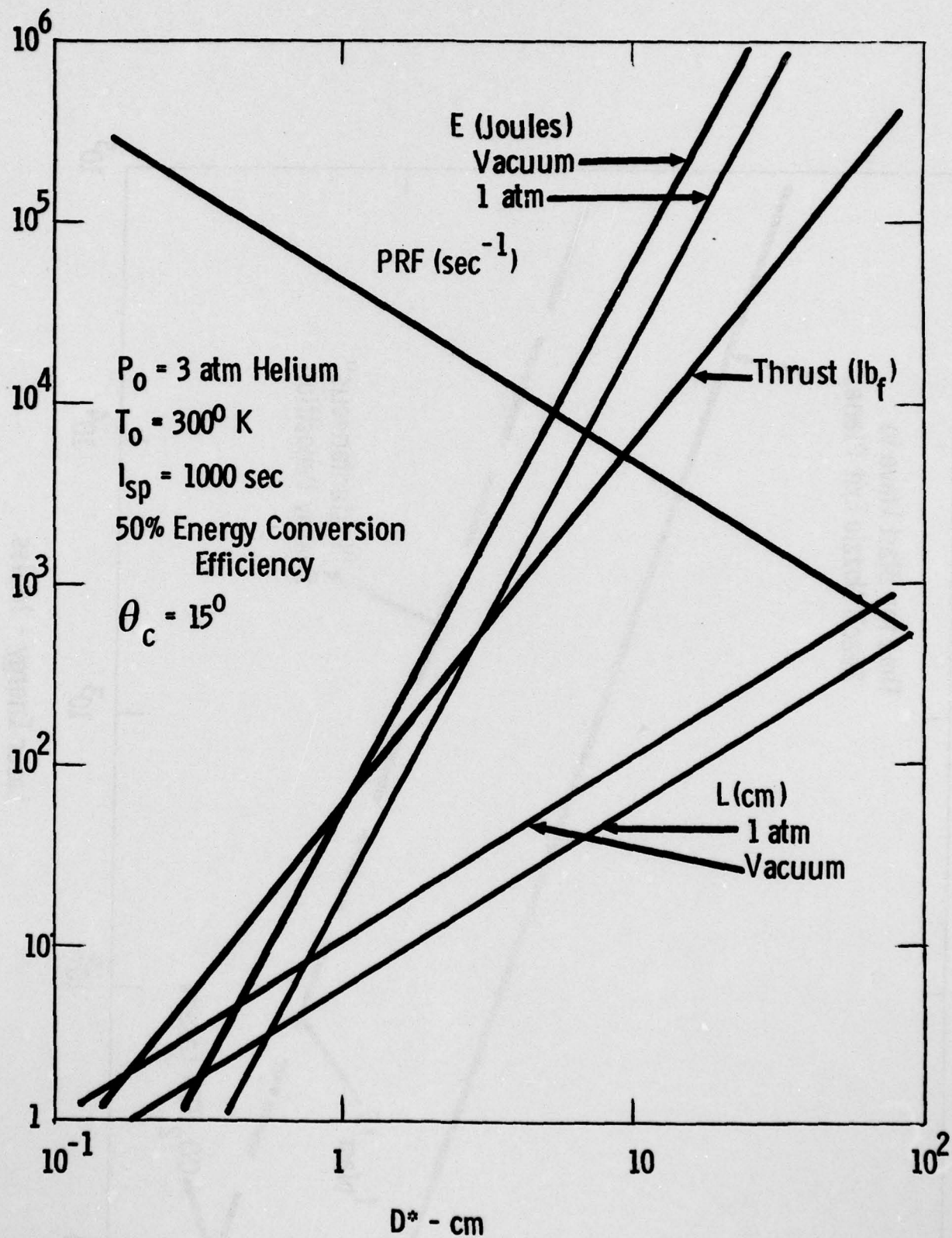


Fig. 5.5 "Universal" Design - Sea Level to Vacuum.

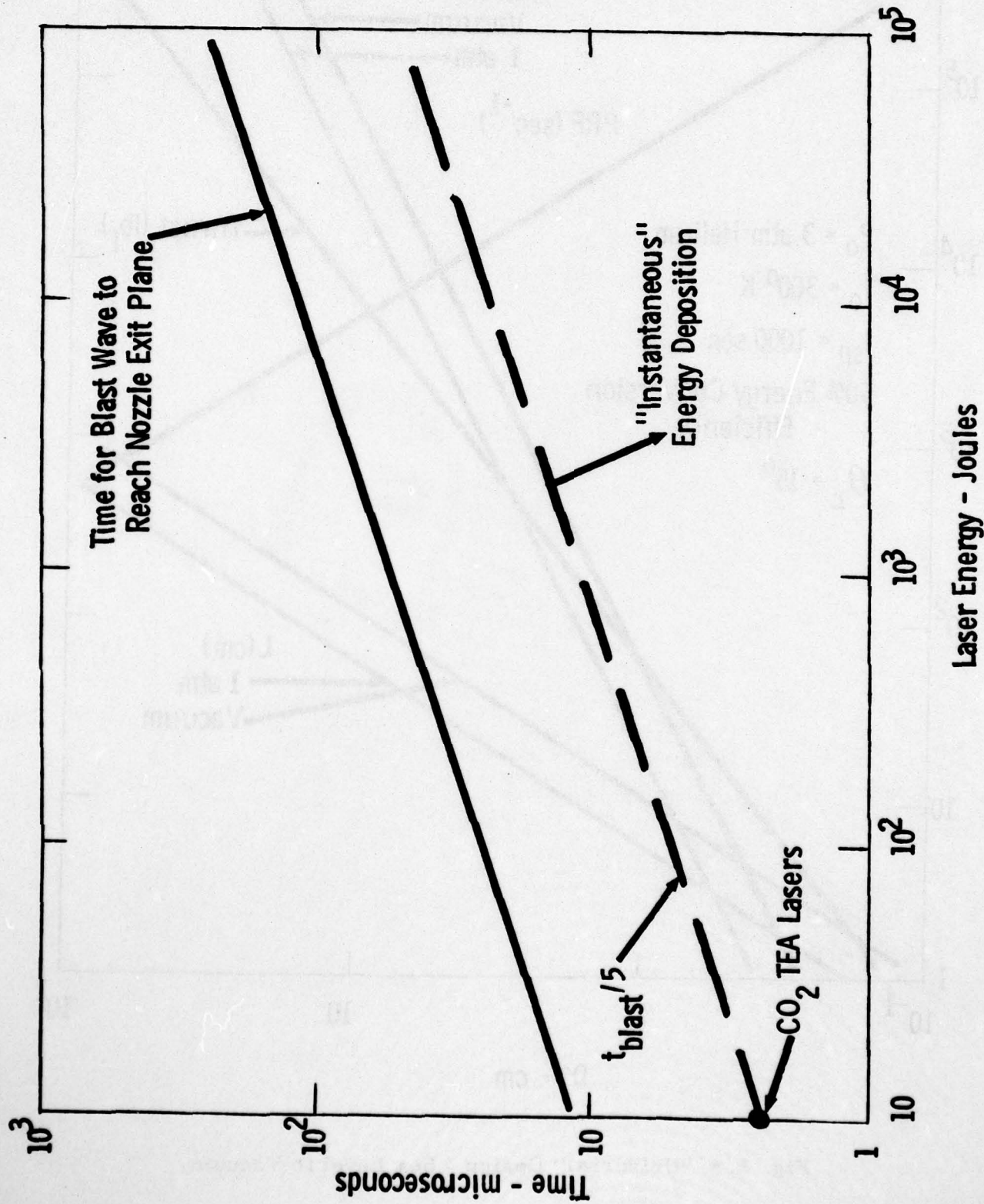


Fig. 5.6 Required Pulse Duration @ 1 atm.

that a 1 KJ laser will require a 22 cm nozzle whereas a 10 to 100 KJ laser will require nozzles upwards of one meter in length. (Parabolic lengths are 1/2 of this value.) The PRF associated with each laser simply depicts the orifice diameter or level of thrust. The criterion which distinguishes the best choice of existing lasers is the pulse duration, τ_p , which must be much less than the shock propagation time t_{blast} as illustrated in Fig. 5.6. If the pulse duration is significantly less than t_{blast} the energy deposition may be considered "instantaneous" and the present theory is valid. Choosing $\tau_p \leq t_{blast}/5$ has proven successful for the small scale laboratory experiments and is used as an upper limit on pulse duration. Hence, a KJ laser must not exceed a 10 μ sec pulse duration, whereas a 10 KJ laser cannot exceed a 25 μ sec pulse duration. So long as these limitations on the pulse duration are accomplished, a corresponding nozzle may be designed to be operated in conjunction with a KJ and 10 KJ laser. These designs are illustrated in Figs. 5.7 and 5.8, respectively. A KJ laser operating at 100 pulses/sec requires a D^* of 0.31 cm, and a length (parabolic) of 11 cm. Such a device will yield 6 lb_f (26.7 Nt) of thrust. Alternatively, a 10 KJ laser operating at 100 pps requires a D^* of 1 cm, $L_p = 23$ cm and will deliver 60 lb_f (267 Nt) thrust. All devices have an aspect ratio of unity as depicted by the original choice of $\theta_c = 15^\circ$ and $L_p = L_c/2$.

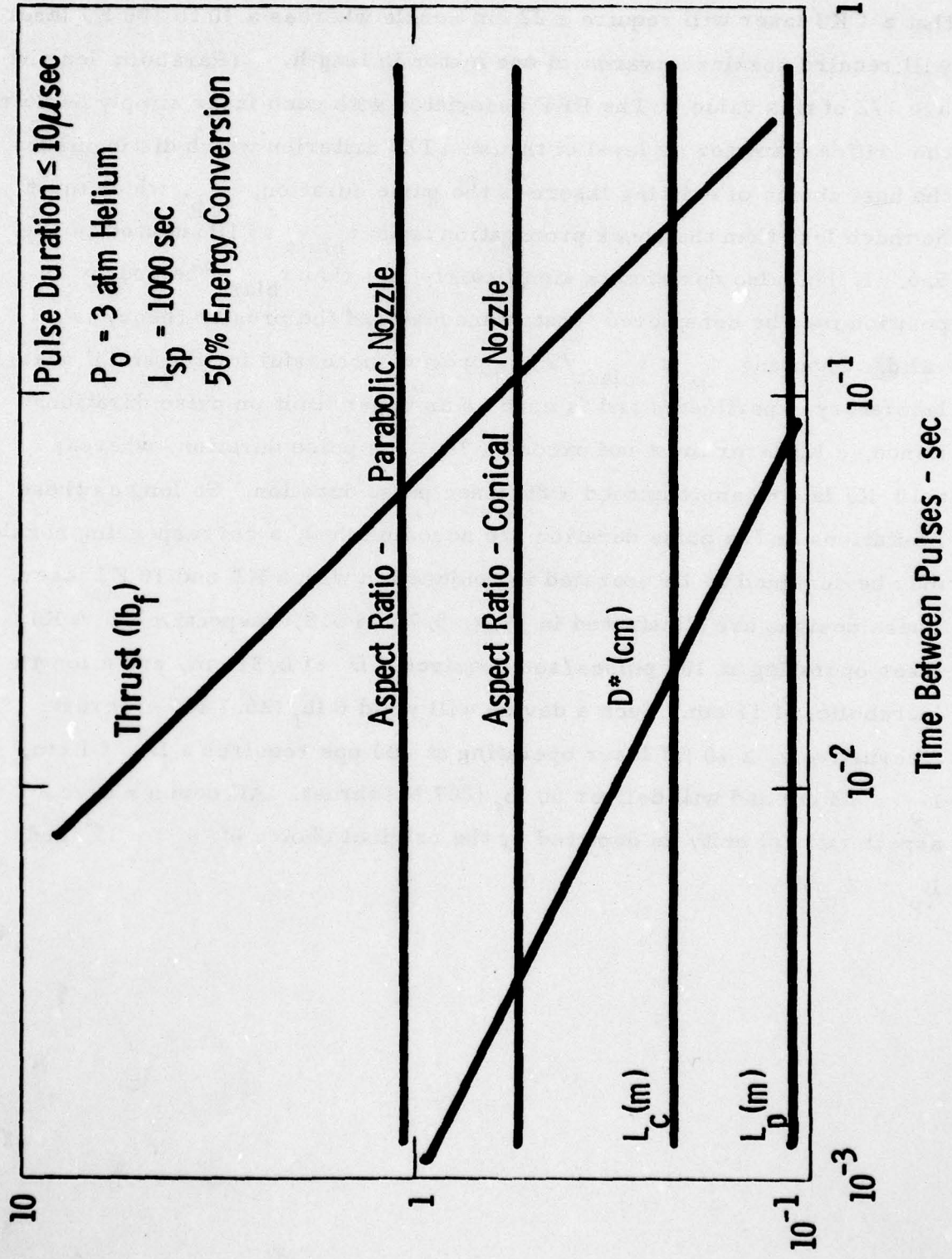


Fig. 5.7 Design for 1 KJ Operation @ 1 atm.

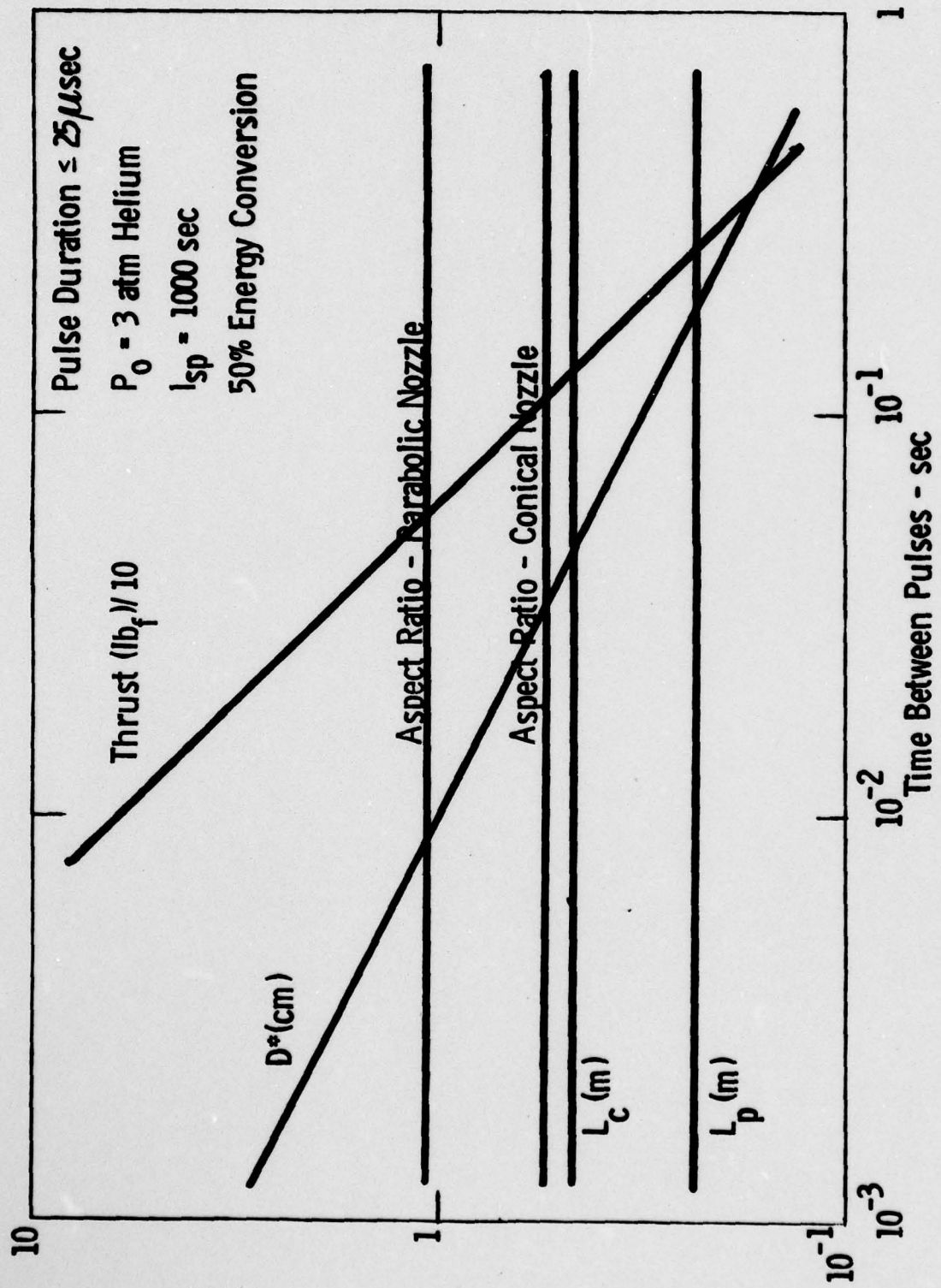


Fig. 5.8 Design for 10 KJ Operation @ 1 atm.

6. SUMMARY AND CONCLUSIONS

A series of proof of principle experiments with supporting analysis have been performed to demonstrate that the PSI pulsed laser propulsion concept can achieve high specific impulse. The maximum specific impulse experimentally obtained was 920 sec at 1 atmospheric operation and 540 sec at low pressure operation. Besides demonstrating a high specific impulse, it was shown that agreement between the specific impulse predicted by a simplified theory and the experimental results are obtained if the conversion efficiency of laser power to rocket power is taken to be 50%. The pulsed laser propulsion concept was demonstrated for both a conical nozzle (which was useful to compare with theory) and a parabolic nozzle which is the most likely nozzle shape for a full scale rocket. In addition, the experiments demonstrated that acoustic valving can be achieved, i.e., the propellant mass flow is regulated by the laser produced blast waves.

Scaling laws were established which specify laser parameters and propellant mass flow to obtain laser powered rocket performance for arbitrary I_{sp} and thrust as a function of back pressure. Results of the scaling laws were discussed in Section 5 and dramatically illustrate that back pressure lowers necessary laser repetition rate while increasing required laser energy per pulse. This allows the use of developing high power laser technology to test this propulsion concept with larger laser energies. For example, a rocket thrust of 100 pounds (445 Nt) with an I_{sp} of 1000 sec can be obtained with a 10 KJ/pulse laser operating at 100 pps.

Since the goal of this program was simply to demonstrate a concept, several issues remain to be resolved. The specific impulse obtained was

a result of two laser pulses. For thrusting in a vacuum each pulse is independent and a two pulse simulation adequately represents the steady-state thrusting sequence. However, at one atmosphere the transient effects of start up may require many pulses before steady-state simulation is obtained. At present, it is not clear how representative the two pulse results are of long duration testing with a one atmosphere background pressure. In addition, helium is not a realistic propellant because of systems considerations and specific impulse measurements with other propellants must be made before an optimum propellant choice can be made. Finally, the energy loss mechanisms must be isolated before the energy conversion efficiency can be determined in order to permit scaling of this thruster concept.

Although many issues remain and this program is far from complete, the results of the present experiment are the first step toward establishing pulsed laser propulsion as a viable future propulsion system.

REFERENCES

1. A. R. Kantrowitz, "Propulsion to Orbit by Ground-Based Lasers," Aeronautics and Astronautics, Vol. 10, No. 5, May 1972, p. 74.
2. A. N. Pirri and R. F. Weiss, "Laser Propulsion," AIAA Paper 72-719, Boston, MA (1972).
3. F. E. Rom and H. A. Putre, "Laser Propulsion," NASA TM-X-2510, April 1972.
4. A. N. Pirri, M. J. Monsler and P. E. Nebolsine, "Propulsion by Absorption of Laser Radiation," AIAA Journal, Vol. 12, No. 9, September 1974, pp. 1254-1261.
5. D. D. Papailiou, ed., "Frontiers in Propulsion Research: Laser, Matter - Antimatter, Excited Helium, Energy Exchange, Thermo-nuclear Fusion," NASA TM 33-722, Jet Propulsion Laboratory, Pasadena, California, March 1975.
6. L. N. Myrabo, "MHD Propulsion by Absorption of Laser Radiation," Journal of Spacecraft and Rockets, Vol. 13, No. 8, August 1976, pp. 466-472.
7. G. E. Caledonia, P. K. S. Wu and A. N. Pirri, "Radiant Energy Absorption Studies for Laser Propulsion," NASA Report CR-134809, Physical Sciences Inc. Report TR-20, March 1975; also P. K. S. Wu and A. N. Pirri, "Stability of Laser Heated Flows," AIAA Journal, Vol. 14, No. 3, March 1976, pp. 390-392.
8. A. N. Pirri, G. A. Simons and P. E. Nebolsine, "The Fluid Mechanics of Pulsed Laser Propulsion," Physical Sciences Inc. Report TR-60; also G. A. Simons and A. N. Pirri, "The Fluid Mechanics of Pulsed Laser Propulsion," AIAA Journal, Vol. 15, pp. 835-842, June 1977.
9. N. H. Kemp, R. G. Root, P. K. S. Wu, G. E. Caledonia, and A. N. Pirri, "Laser-Heated Rocket Studies," NASA Report CR-135127, Physical Sciences Inc. Report TR-53, May 1976; also N. H. Kemp and R. G. Root, "Nozzle Flow of Laser-Heated, Radiating Hydrogen with Application to a Laser-Heated Rocket," AIAA Paper 77-695.

10. F. V. Bunkin and A. M. Prokhorov, "Use of Laser Energy Source in Producing Reactive Thrust," Sov. Phy. Usp., Vol. 19, pp. 561-573, July 1976.
11. A. N. Pirri, R. Schlier and D. Northam, "Momentum Transfer and Plasma Formation Above a Surface with a High Power CO₂ Laser," Applied Physics Letters, Vol. 21, No. 3, August 1972, pp. 79-81.
12. J. E. Lowder, D. E. Lencioni, T. W. Hilton, and R. J. Hull, "High-Energy Pulsed CO₂ Laser-Target Interaction in Air," Journal of Applied Physics, Vol. 44, No. 6, June 1973, p. 2759.
13. A. N. Pirri, "Theory for Momentum Transfer to a Surface with a High-Power Laser," The Physics of Fluids, Vol. 16, No. 9, September 1973, p. 1435.
14. R. B. Hall, W. E. Maher, and P. S. P. Wei, "An Investigation of Laser-Supported Detonation Waves," AFWL-TR-73-28, June 1973, Air Force Weapons Lab., N. Mexico.
15. L. R. Hettche, J. T. Schriempf, and R. L. Stegman, "Impulse Reaction Resulting from the In-Air Irradiation of Aluminum by a Pulsed CO₂ Laser," Journal of Applied Physics, Vol. 44, No. 9, September 1973, p. 4079.
16. L. H. Back and G. Varsi, "Detonation Propulsion for High Pressure Environments," AIAA Journal, Vol. 12, No. 8, August 1974, pp. 1123-1130.
17. G. Varsi, L. H. Back and K. Kim, "Blast Wave in a Nozzle for Propulsive Applications," Acta Astronautica 3, pp. 141-156.
18. K. Kim, L. H. Back, G. Varsi, "Measurement of Detonation Propulsion in Helium and Performance Calculations," AIAA Journal, Vol. 14, pp. 310-312, March 1976.
19. K. Kim, "Exit of Blast Wave From a Conical Nozzle," AIAA Paper 76-401.
20. K. Kim, G. Varsi, L. H. Back, "Blast Wave Analysis Detonation Propulsion," AIAA Journal, Vol. 15, pp. 1500-1503.

21. Y. Zel'dovich and Y. Raizer, Physics of Shock Waves and High-Temperature Hydrodynamics Phenomena, Vol. 1, Academic Press, New York, 1966.
22. C. Lahaye, L. Jean, and H. Doyle, "Velocity Distributions in the Wake of Spheres," AIAA Journal, Vol. 8, 1521, (1970).
23. G. G. Bach and J. H. S. Lee, "An Analytical Solution for Blast Waves," AIAA Journal, Vol. 12, 271-275, (1970).

APPENDIX

DIRECT MEASUREMENT OF PROPELLANT EXHAUST VELOCITY USING DOUBLE SPARK TECHNIQUE

A direct measurement of the propellant exhaust velocity was desired to provide more accurate measurements of I_{sp} than those discussed above. Because of the high velocities ($> 10^5$ cm/sec) and short duration ($\sim 10^{-5}$ sec), conventional velocity measurement techniques are not applicable. Thus, a double spark technique was developed which could provide the data under certain conditions. This double spark technique was a modification of the technology developed by Lahaye et al.²² Unfortunately, the diagnostic did not work for conditions of prime interest, i.e., rocket operation with two laser pulses, and the data from pressure transducers and blast wave theory were subsequently used to deduce exhaust velocity, blast wave energy and ambient density. It is not clear at this time whether the problems with the spark diagnostic could not have been resolved with further work; however, continued troubleshooting was beyond the scope of the present contract.

The technology will now be described.

In the double spark technique, two pairs of electrodes were placed along the direction of the flow as shown in Fig. A1. The technique is based upon the following features:

- (i) A spark at the first set of electrodes ionizes a narrow filament of gas;
- (ii) The ionized gas moves with the flow velocity towards the second pair of electrodes;

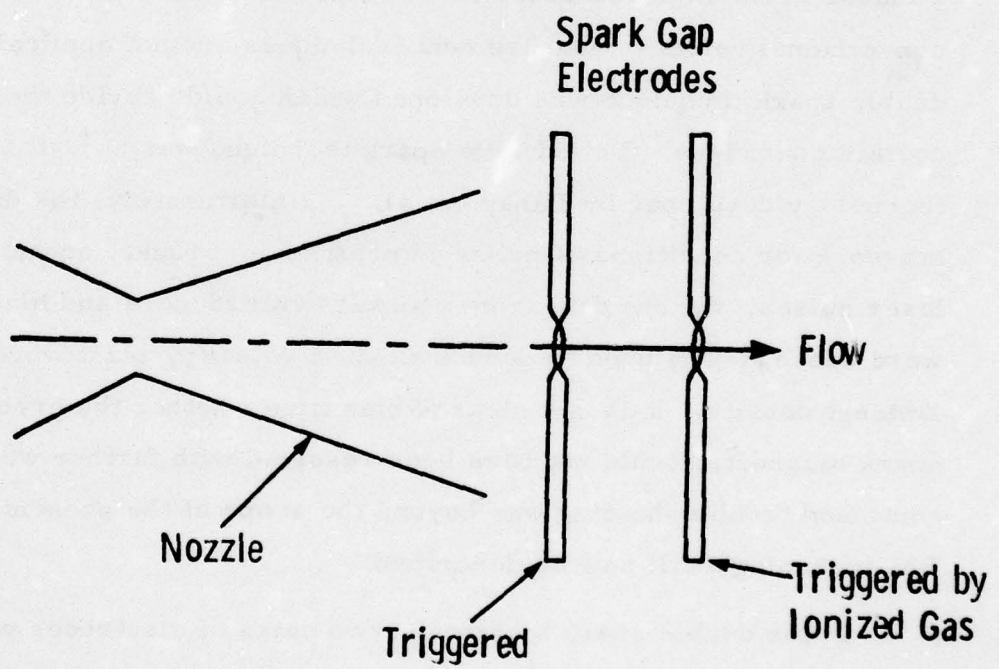


Fig. A. 1 Double Spark Velocity Diagnostic.

- (iii) Before the ionized gas reaches the second pair, a voltage, which is approximately 90% of the minimum voltage that causes a breakdown in the ambient gas, is applied on the spark gap 2;
- (iv) When the ionized gas moves to the second set, a breakdown occurs in the presence of the applied voltage.

The precise timings of occurrence of the two sparks can be obtained either by using a photodiode or by monitoring the current pulses using a current loop. Thus, a determination of the time it takes for the gas to flow from spark gap 1 to spark gap 2 can be made. Knowing the distance between the two pairs of electrodes and assuming that the flow velocity essentially remains constant from one pair to the other, we can determine the gas velocity.

To test the technique, the flow velocity measured from the double spark technique as described above was compared with a Pitot tube measurement. A steady flow was created in a pipe of 3 cm diameter using a vacuum pump. A velocity of 80 meters/sec measured with the double spark technique was found to be within 20% of that obtained from a Pitot tube measurement.

It is possible to arrange the two sets of electrodes in two ways, 1) the parallel configuration (Figs. A. 1); and 2) the perpendicular configuration (Fig. A. 2). The alignment of the electrodes is critical in the parallel configuration while only a fraction of the ionized gas is utilized to trigger spark gap 2 in the perpendicular configuration. Preliminary experiments performed using both these configurations yielded useful velocity data. However, due to alignment considerations, we have used the perpendicular configuration.

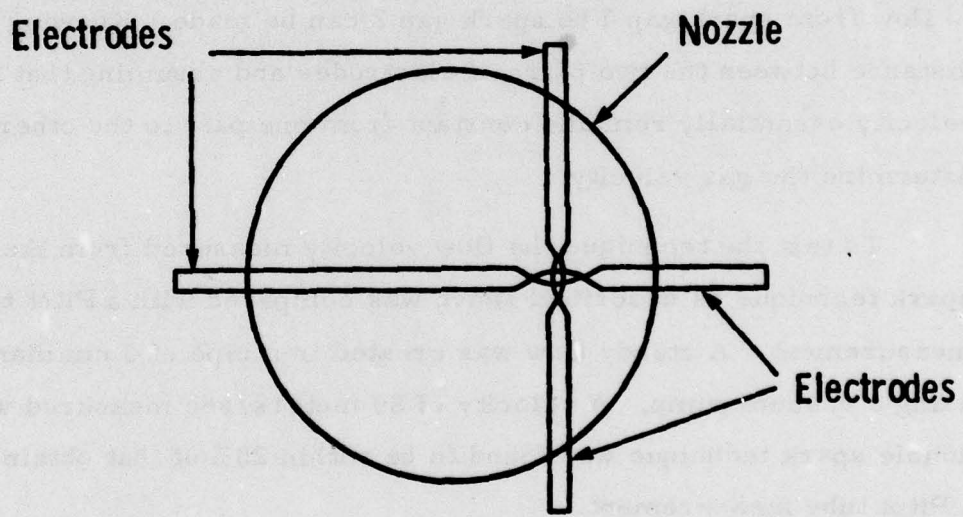


Fig. A. 2 Perpendicular Electrode Configuration.

It would be illuminating to list conditions under which the velocity measurements using the double spark technique will work. Let h_1 and h_2 be the electrode gaps in spark gap 1 and 2 and d the distance between the two sets of electrodes. To prevent electrical interference between the two pairs (i.e., jumping of the spark from one set to the other), the following condition should be satisfied

$$d > h_1, h_2 .$$

Ideally, one would like to keep d as small as possible. This means that both h_1 and h_2 should be minimized. This can be accomplished by using very thin electrodes. In our case, we used pointed graphite electrodes 1.5 mm in diameter made from a soft pencil lead. Typically, the spark gap was 2 mm while d was 5 mm. Of all the electrode materials tested, including aluminum and copper, the life of the graphite electrodes was found to be the longest.

The two triggered electronic circuits schematically shown in Figs. A. 3 and A. 4 use Krytron tubes EG & G#KN-6B. One square trigger pulse (width $\sim 2 \mu\text{sec}$ and ~ 30 volts) from the delay generator triggers both these circuits. The circuit shown in Fig. A. 3 cannot be used for the second pair as it is not designed to apply the voltage for an extended period of time while the circuit in Fig. A. 4 could be used for both sets of electrodes, if desired. In our case, we have used the circuit in Fig. A. 3 to trigger spark gap 1 and the circuit in Fig. A. 4 to apply voltage to the second set of electrodes.

The location of the electrodes with respect to the rocket nozzle is shown in Fig. A. 2. To ensure that the electrodes do not block the laser beam, the electrodes were placed to one side of the nozzle as shown.

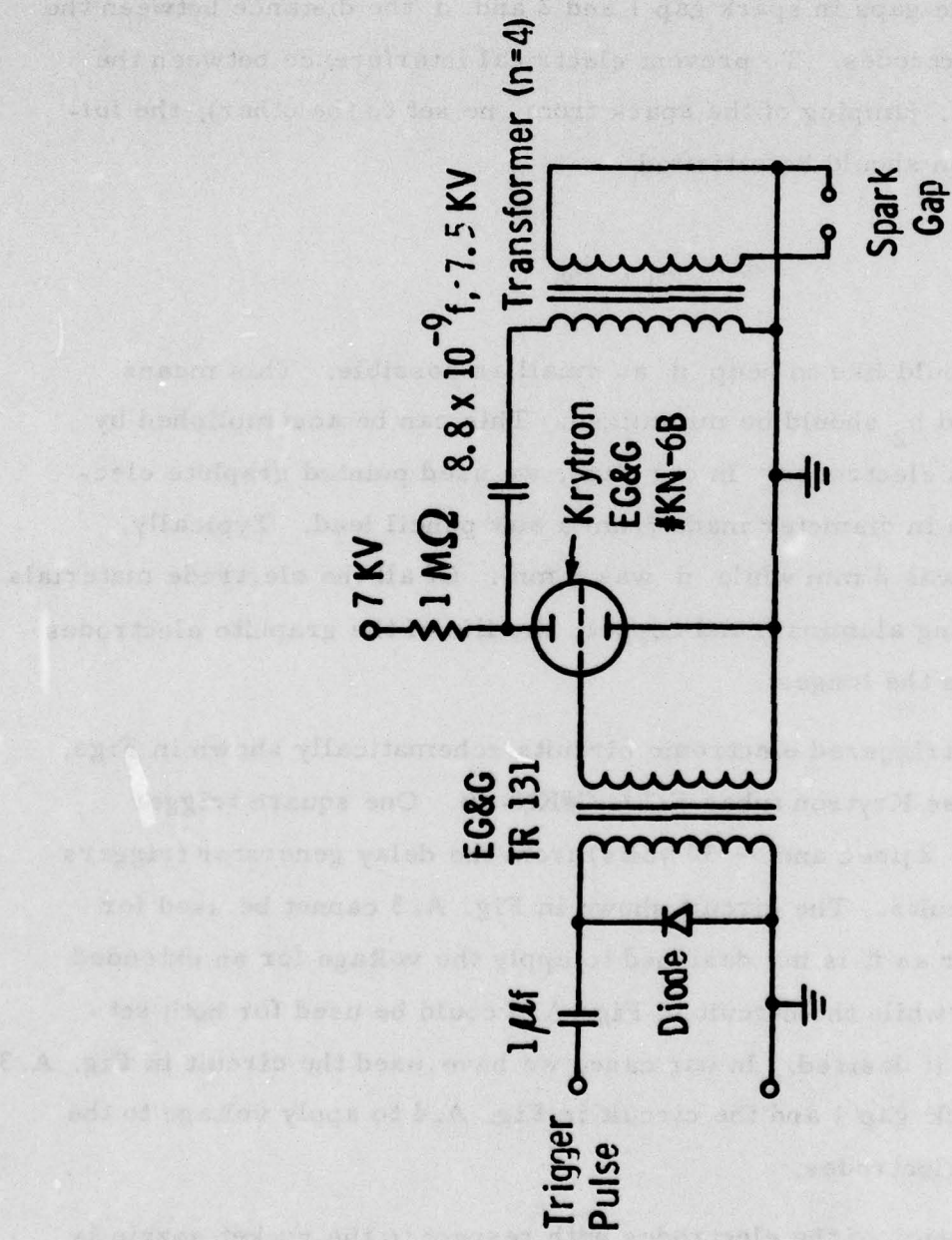


Fig. A.3 Electronic Schematic for Triggering Spark Gap.

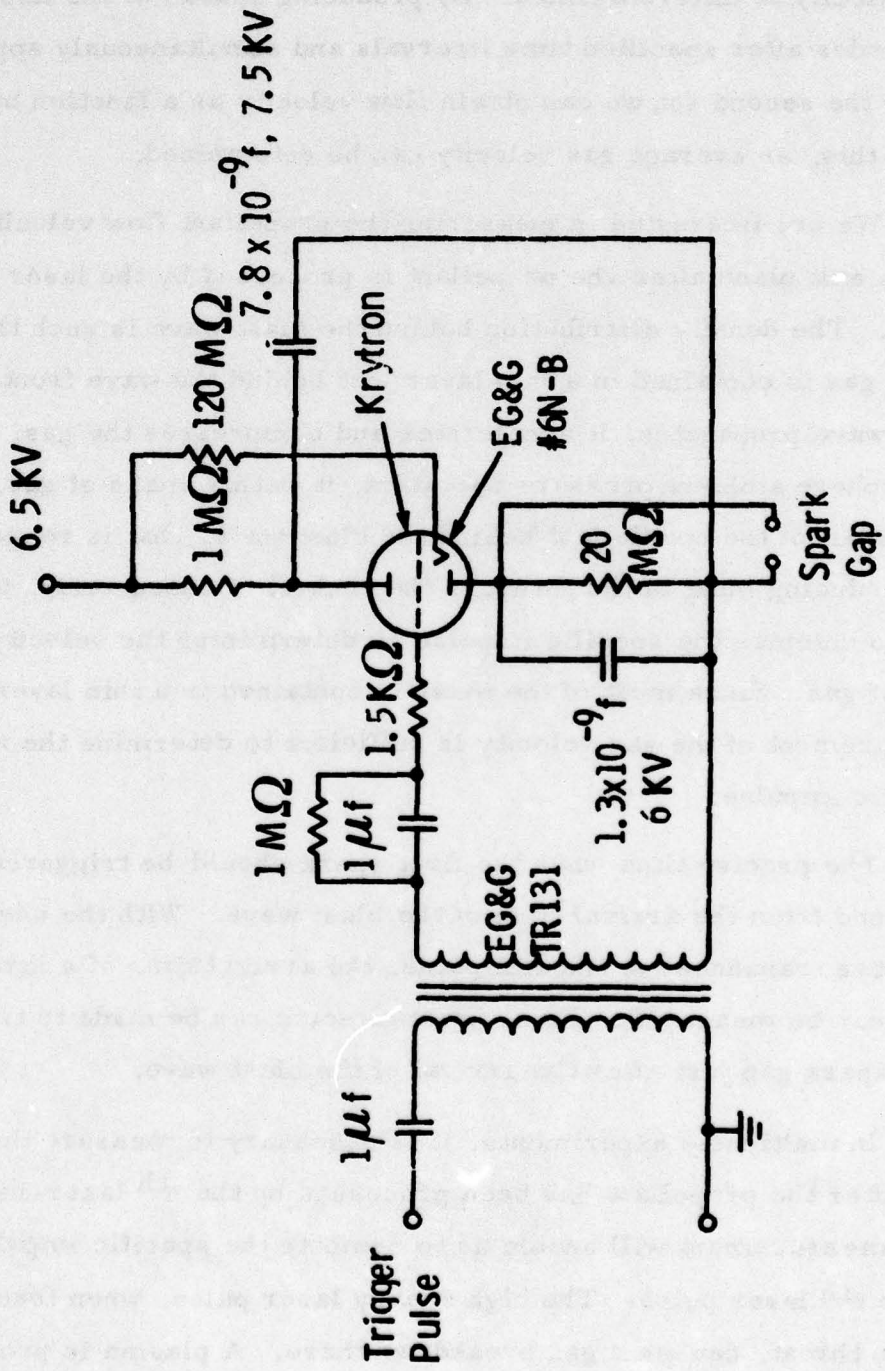


Fig. A. 4 Electronic Schematic For Switching Voltage on Gap.

The double spark scheme, in principle, can be used to measure the gas velocity at different times. By producing sparks at the first set of electrodes after specified time intervals and simultaneously applying voltage at the second set, we can obtain flow velocity as a function of time. From this, an average gas velocity can be determined.

We are interested in measuring the propellant flow velocity at the nozzle exit plane after the propellant is processed by the laser initiated shock. The density distribution behind the blast wave is such that most of the gas is contained in a thin layer just behind the wave front. As the blast wave propagates, it accelerates and compresses the gas. In one atmosphere ambient pressure operation, it is this mass of gas, which comes out of the nozzle just behind the blast wave, that is responsible for producing most of the thrust in the rocket. Consequently, it is reasonable to compute the specific impulse by determining the velocity of this slug of gas. Since most of the mass is contained in a thin layer, one time measurement of the gas velocity is sufficient to determine the average specific impulse.

The precise time when the first spark should be triggered is determined from the arrival time of the blast wave. With the use of a pressure transducer at the exit plane, the arrival time of a laser blast wave can be measured. Thus, arrangements can be made to trigger the first spark gap just after the arrival of the blast wave.

In multipulse experiments, it is necessary to measure the gas velocity after the propellant has been processed by the n^{th} laser-initiated shock. This measurement will enable us to compute the specific impulse produced by the n^{th} laser pulse. The high energy laser pulse, when focused at the nozzle throat, causes a gas breakdown there. A plasma is produced, and

the ionized gas flows out of the nozzle behind the blast wave. Since the double spark scheme is based upon ionizing the gas at the first set of electrodes and subsequent movement of this ionized gas to the second set, it is necessary to determine if the residual ionization due to the proceeding laser pulse will interfere with the velocity diagnostics in the multi-pulse experiments.

In order to obtain an understanding of the interference problem, one should consider the following:

- (i) What is the motion of the ionized gas initially produced at the nozzle throat as a function of time? For this an x-t diagram describing the motion of the blast wave and the gas is required.
- (ii) What is the electron density (i. e., the degree of ionization of the gas) that is required to trigger the spark gap at 2? Coupled to this is the issue: Is the recombination process in the ionized gas fast enough that the residual ionization in the gas is incapable of triggering the second spark?

The details of the motion of the blast wave as a function of time are illustrated in the x-t diagram of Fig. A. 5. This map is prepared assuming a constant density helium flow in the nozzle at S. T. P. The blast wave solutions, modified to account for the solid angle of the nozzle, are assumed to be applicable. Even though the laser pulse of energy 8.7 Joules is focused at the throat, the shape of the wave front is such that for large propagation distances (propagation distances \gg throat dia) it would appear to have originated from a virtual source which is 0.93 cm upstream of the throat. Since it takes only a fraction of a microsecond

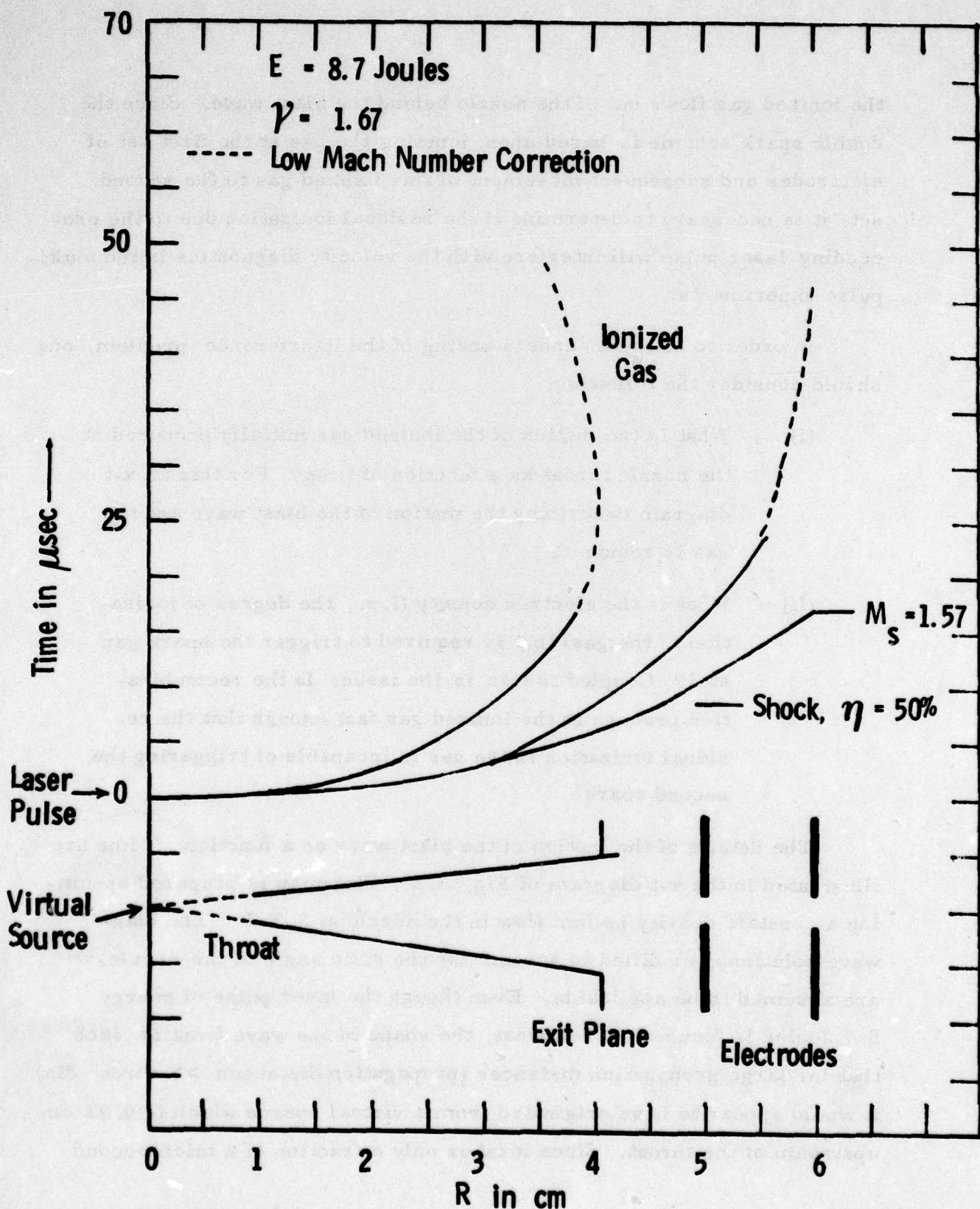


Fig. A. 5 x - t Diagram for Single Pulse in He.

for the blast wave to move from the virtual source to the throat, in the computation of the propagation times, the origin of time has also been shifted to that for the virtual source.

The open shutter pictures of the plasma produced by a high energy laser pulse in one atmosphere ambient pressure show that on the average the length of the plasma is 2 cm. Consequently, we assume that the initial breakdown, produces charged particles for a distance of 2 cm downstream of the throat. Our aim is to determine the motion of these charged particles as a function of time and space.

The well known equations for a blast wave for constant density will now be used to determine an x-t diagram for fluid elements.²¹ The velocity profile of the gas behind the blast wave is weakly dependent upon γ , the ratio of specific heat at constant pressure to specific heat at constant volume. If U is the gas velocity at a distance r from the source and U_1 is the gas velocity just behind the blast wave which is at a distance R_s ($R_s > r$) from the source, the blast wave calculations show that U/U_1 is a function of r/R_s . For strong blast waves and for $r/R_s \geq 0.5$, U/U_1 is a linear function of r/R_s . From this we can determine the motion of a slug of gas as a function of time as follows:

$$\frac{U}{U_1} = \frac{r}{R_s} \text{ for } r \leq R_s . \quad (\text{A. 1})$$

if $D (= d R_s / dt)$ is the blast wave velocity, then

$$U_1 = \left(\frac{2}{\gamma + 1} \right) D . \quad (\text{A. 2})$$

The blast wave velocity is related to time, ambient density, and energy by

$$D = \xi_0 \frac{2}{5} \left(\frac{E}{\rho_0} \right)^{1/5} t^{-3/5} \left(\frac{4\pi}{\Omega} \right)^{1/5} \quad (A. 3)$$

where E is the blast wave energy, ρ_0 is the ambient density and ξ_0 is a numerical constant though a function of γ . Therefore,

$$U = \frac{r}{R_s} \quad U_1 = \frac{r}{R_s} \frac{2}{\gamma + 1} \xi_0 \frac{2}{5} \left(\frac{E}{\rho_0} \right)^{1/5} \left(\frac{4\pi}{\Omega} \right)^{1/5} t^{-3/5} \quad (t > 0). \quad (A. 4)$$

Also

$$R_s = \xi_0 \left(\frac{E}{\rho_0} \right)^{1/5} t^{2/5} \left(\frac{4\pi}{\Omega} \right)^{1/5}, \quad (A. 5)$$

$$\therefore U = \frac{r}{t} - \frac{4}{5(\gamma + 1)} \quad r < R_s \quad (A. 6)$$

or

$$U = \frac{dr}{dt} = \frac{4}{5(\gamma + 1)} - \frac{r}{t} .$$

On integration we get

$$t = C_1 r^\alpha \quad (A. 7)$$

where $\alpha = [4/5 (\gamma + 1)]^{-1}$ and C_1 is the integration constant.

For helium $\gamma = 1.67$ and, therefore, $\alpha = 3.34$, thus we have

$$t = C_1 r^{3.34} .$$

An x-t diagram has been computed and is shown in Fig. A.5. We present the path of two slugs of gas, one which starts from the throat and the other which starts 2 cm downstream of the throat, as a function of time. The relation $t = C_1 r^{3.34}$ was used and the following boundary conditions were applied:

$$t = 0.193 \mu\text{sec} \text{ at } r = 1 \text{ cm}$$

for a slug of gas starting from the throat, and

$$t = 3.00 \mu\text{sec} \text{ at } r = 3 \text{ cm}$$

for a slug of gas starting from 2 cm downstream of the throat.

At large propagation distances from the virtual source, the blast wave becomes weak. When the blast wave has propagated 6 cm the virtual source, at an energy conversion efficiency of 50%, its Mach number is only 1.57. In the same time the slug of gas which started from the throat propagates 3.9 cm in the map of Fig. A.5. Consequently, for further determination of the motion of the slug of gas, the assumption of a strong blast wave is not valid and it is necessary to incorporate a low Mach number correction to the gas motion.

For air ($\gamma = 1.4$), Back and Lee²³ have obtained the velocity profile (U/U_1) as a function r/R_s for different shock Mach numbers [M_s].

Their numerical results are also valid for low shock Mach numbers. Since the velocity profile is weakly dependent upon γ , it is appropriate to use their numerical results to obtain a qualitative understanding.

In Fig. A. 6, U/U_1 is plotted as a function of r/R_s . Within 5%, this curve is valid for $M_s^2 = 2.5$ and is taken from Back and Lee.

Thus,

$$\frac{U}{U_1} = -1.5 + 2.5 \left(\frac{r}{R_s} \right). \quad (\text{A. 8})$$

From Eqs. (A. 2 - A. 4) we get

$$U = \frac{dr}{dt} = \left(\frac{2}{\lambda + 1} \right) \left[-1.5 + 2.5 \left(\frac{r}{R_s} \right) \right] \xi_o \frac{2}{5} \left(\frac{E}{\rho_o} \right)^{1/5} \left(\frac{4\pi}{\Omega} \right)^{1/5} t^{-3/5}. \quad (\text{A. 9})$$

On integration,

$$r = A t^{K_1} - \frac{K_2}{\left(\frac{2}{5} - K_1 \right)} t^{2/5} \quad (\text{A. 10})$$

where

$$K_1 = \left(2 / (\gamma + 1) \right)$$

$$K_2 = \left(1.2 / (\gamma + 1) \right) \xi_o \left(E / \rho_o \right)^{1/5} \left(4\pi / \Omega \right)^{1/5}.$$

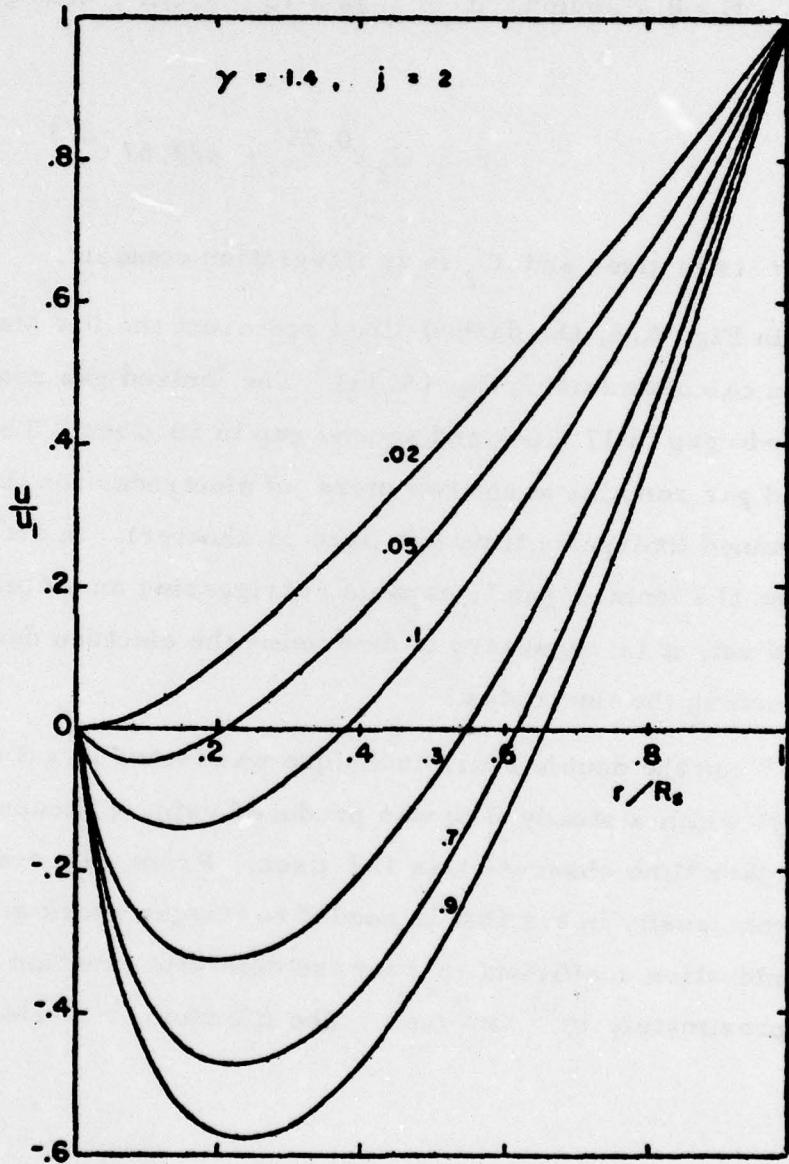


Fig. A. 6 The Particle Velocity Distributions
Behind Spherical Blast Wave of
Various Shock Strengths η , $\gamma = 1.4$.

For helium flow, with $\gamma = 1.67$, the energy conversion efficiency = 50%, $E = 8.7$ Joules, $\rho_0 = 1.62 \times 10^{-4} \text{ g/cm}^3$, and $\xi_0 = 1.112$, we obtain

$$r = C_2 t^{0.75} + 622.57 t^{2/5} \quad (\text{A. 11})$$

when t is in μsec and C_2 is an integration constant.

In Fig. A. 5, the dashed lines represent the low Mach number correction calculated using Eq. (A. 11). The ionized gas reaches the first electrode gap in 17 μsec and second gap in 50 μsec . Thereafter, the ionized gas remains at the two pairs of electrodes for times longer than the planned interpulse time (60 μsec or shorter). In order to determine whether the ionized gas is capable of triggering an untimely spark at the second set, it is necessary to determine the electron density in the gas surrounding the electrodes.

When the double spark technique was tested in a 3 cm diameter tube, through which a steady flow was produced using a vacuum pump, the longest interspark time observed was 162 μsec . From this, we can estimate the electron density in air that is needed to trigger spark gap 2. In air the recombination coefficient (ρ_e) for the dominant reaction $N_0^+ + e \rightarrow N_0$ is approximately $10^{-7} \text{ cm}^3/\text{sec}$. The life time τ of electrons is given as

$$\tau = \frac{1}{\rho_e N_e} = 1.62 \times 10^{-4} \text{ sec.}$$

Therefore, in air, the electron density required to trigger the spark gap 2 is $6 \times 10^{10} \text{ electrons/cm}^3$. In helium, the recombination rate is slower;

consequently, an electron density of 6×10^{10} electron/cm³ or more would persist for at least 162 μ sec. If the first spark is triggered after 17 μ sec and before 179 μ sec from the laser pulse, the spark will be produced in the ionized gas surrounding the first electrode, thereby increasing the degree of ionization of the gas. Since the ionized gas is capable of triggering the second spark, even when the first spark is not produced, it is difficult to determine an unambiguous, meaningful correlation between the flow velocity and the instant the second spark is triggered.

From this analysis, we draw the following conclusions:

- (i) The double spark scheme for velocity measurement can be used to measure gas velocity and indeed was tested for single pulsed experiments. This is possible when the first spark is triggered just after the arrival of the blast wave and before the arrival of the ionized gas at the first electrode.
- (ii) In the multipulse experiments, the residual ionization caused by the preceding laser pulse would interfere with velocity measurement and may trigger either an untimely second spark or may cause the spark to jump to the wrong electrode. Therefore, the double spark technique cannot be used to measure gas velocity in the multipulse experiments if the interpulse time is going to be less than about 162 μ sec. Since the planned interpulse time is much less than 162 μ sec, it appears that this scheme is not useful for our application.

In Fig. A. 7, an open shutter picture of the spark technique is presented. Only one laser pulse is fired. The picture shows the plasma that

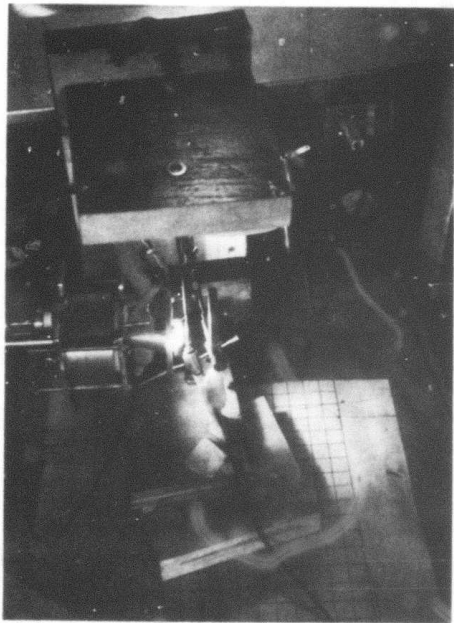
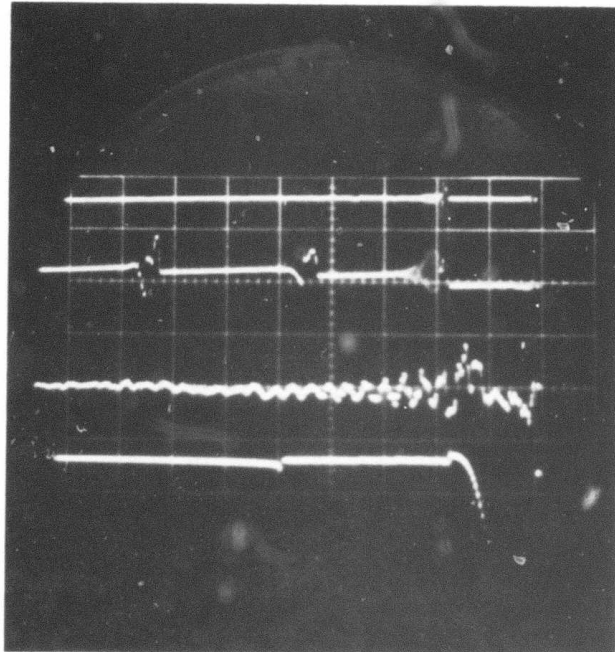


Fig. A.7 Open Shutter.

has come out of the exit plane and two sparks at the two sets of electrodes. The first spark is vertical, as expected, while the second is convex upstream. The convex shape of the second spark shows that the spark is triggered by the flowing electrons. (In unionized air at rest, the spark is generally straight.) The precise timings of the occurrence of events are presented in the oscilloscope trace of Fig. A. 8. The arrival time of the blast wave at the pressure transducer placed at the first pair of electrodes indicates that a substantial portion of the conical nozzle is filled with air. The photodiode signal indicates that the second spark occurred 64 μ sec after the first spark. The x-t diagram in air also predicts long interspark times (Fig. A. 9). It is also clear that in air the assumption of constant gas velocity between the two pairs of electrodes introduces large errors while this is not so in helium (Fig. A. 5).



} Current Pickups
Pressure
← Transducer
← Photodiode

← t

Fig. A.8 Oscilloscope Trace.

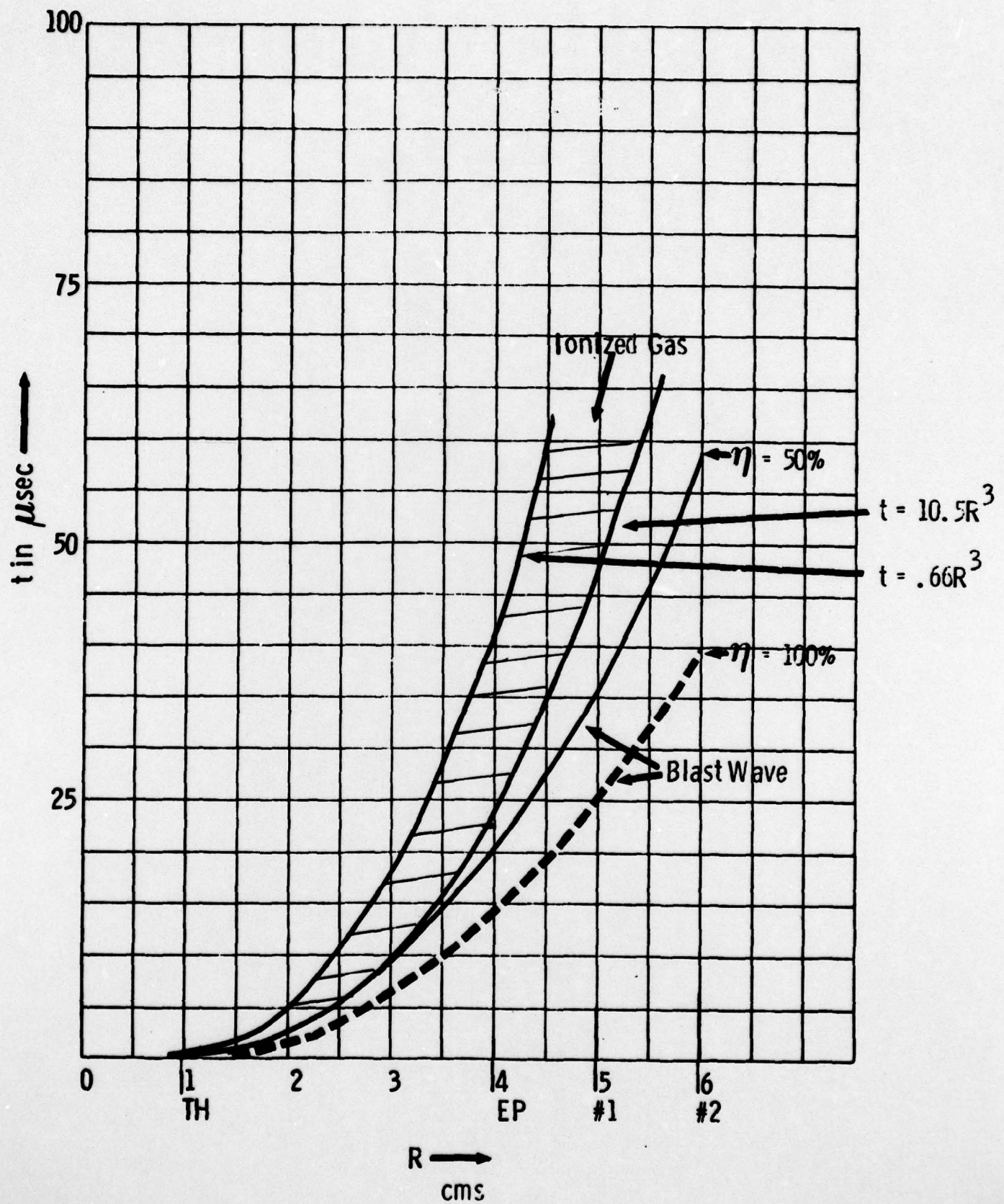


Fig. A. 9 x - t Diagram for Single Pulse in Air.

DISTRIBUTION LIST
FOR
FINAL REPORT

Contract No. N00014-76-C-0738

Scientific Officer Office of Naval Research 495 Summer Street Boston, MA 02210 ATTN: Dr. Al Wood	1 copy
Scientific Officer c/o Physical Sciences Division Office of Naval Research 800 N. Quincy Street Arlington, VA 22217 ATTN: Dr. W. J. Condell (Code 421)	3 copies
Defense Contract Administration Services District, Boston 666 Summer Street Boston, MA 02210 ATTN: Mr. Robert D. Wholey Administrative Contracting Officer	1 copy
Director, Naval Research Laboratory Washington, D.C. 20375 ATTN: Code 2627	6 copies
Defense Advanced Research Projects Agency 1200 Wilson Boulevard Arlington, VA 22209 ATTN: DOD Code HX1241 M. O'Neill R. Sepucha J. Mangano	1 copy 1 copy 1 copy 1 copy
HQ Electronics Systems Division (ESL) L. G. Hanscom Field Bedford, MA 01730 ATTN: Mr. Alfred E. Anderson (XRT) Technical Library	1 copy 1 copy

Air Force Rocket Propulsion Laboratory 1 copy
ATTN: Vince Benham (LKDH)
Edwards AFB, CA 93523

Department of the Air Force 1 copy
Foreign Technology Division
ATTN: TQTD (Fiene)
Wright Patterson AFB, OH 45433

Defense Intelligence Agency 1 copy
ATTN: Mr. Seymour Berler (DTIB)
Washington, D. C. 20301

Central Intelligence Agency 1 copy
ATTN: Mr. Julian C. Nall
Washington, D. C. 20505

Aerospace Corporation 1 copy
ATTN: Dr. G. P. Millburn
P. O. Box 92957
Los Angeles, CA 90009

AVCO Everett Research Laboratory 1 copy
2385 Revere Beach Parkway
Everett, MA 02149
ATTN: Dr. George Sutton

Boeing Company 1 copy
ATTN: Mr. M. I. Gamble (2-, 460, MS 8C-88)
P. O. Box 3999
Seattle, WA 98124

Hughes Research Labs 1 copy
ATTN: Dr. D. Forster
3011 Malibu Canyon Road
Malibu, CA 90265

Institute for Defense Analyses 1 copy
ATTN: Dr. Alvin Schnitzler
400 Army-Navy Drive
Arlington, VA 22202

Lawrence Livermore Laboratory
P. O. Box 808
Livermore, CA 94550
ATTN: Dr. R. E. Kidder 1 copy
 Dr. E. Teller 1 copy
 Dr. Joe Fleck 1 copy

Los Alamos Scientific Laboratory 1 copy
ATTN: Dr. Keith Boyer
P. O. Box 1663
Los Alamos, NM 87544

Lockheed Palo Alto Research Laboratory 1 copy
ATTN: L. R. Lunsford
 Orgn. 52-24, Bldg. 201
3251 Hanover St.
Palo Alto, CA 94303

Mathematical Sciences Northwest, Inc. 1 copy
ATTN: Dr. Abraham Hertzberg
P. O. Box 1887
Bellevue, WN 98009

Massachusetts Institute of Technology
Lincoln Laboratory
P. O. Box 73
Lexington, MA 02173
ATTN: Dr. S. Edelberg 1 copy
 Dr. L. C. Marquet 1 copy

Mc Donnell Douglas Research Laboratories 1 copy
ATTN: Dr. D. P. Ames
Dept. 220, Box 516
St. Louis, MO 63166

MITRE Corp 1 copy
ATTN: N. Harmon
P. O. Box 208
Bedford, MA 01730

Northrop Corp. 1 copy
ATTN: Dr. Gerard Hasserjian
Laser Systems Department
3401 West Broadway
Hawthorne, CA 90250

RAND Corp. 1 copy
ATTN: Dr. C. R. Culp/Mr. G. A. Carter
1700 Main Street
Santa Monica, CA 90406

Raytheon Company 1 copy
ATTN: Dr. F. A. Horrigan (Res. Div.)
28 Seyon Street
Waltham, MA 02154

Riverside Research Institute 1 copy
ATTN: (HPEGL Library)
80 West End Street
New York, NY 10023

R & D Associates, Inc. 1 copy
ATTN: Dr. R. E. LeLevier
P. O. Box 3580
Santa Monica, CA 90431

SANDIA Corp. 1 copy
ATTN: Dr. Al Narath
P. O. Box 5800
Albuquerque, NM 87115

Science Applications, Inc. 1 copy
ATTN: L. Peckam
1911 N. Ft. Meyer Drive
Arlington, VA 22209

Science Applications, Inc. 1 copy
ATTN: R. E. Meredith
P. O. Box 328
Ann Arbor, MI 48103

TRW Systems Group 1 copy
ATTN: Mr. Norman Campbell
One Space Park
Bldg. R-1, Rm. 1050
Redondo Beach, CA 90278

United Technologies Research Center 3 copies
ATTN: Mr. G. H. McLafferty
400 Main Street
East Hartford, CT 06108

Westinghouse Research Laboratories 1 copy
ATTN: Dr. E. P. Riedel
Beulah Road, Churchill Boro
Pittsburgh, PA 15235

United Technologies Research Center 1 copy
ATTN: A. J. DeMaria
East Hartford, CT 06108

General Electric R & D Center 1 copy
ATTN: Dr. Donald White
Schenectady, NY 12305

EXXON Research and Engineering Company 1 copy
ATTN: D. Grafstein
P.O. Box 8
Linden, NJ 07036

Massachusetts Institute of Technology 1 copy
ATTN: Prof. A. Javan
77 Massachusetts Avenue
Cambridge, MA 02138

Office of the Director of Defense 1 copy
Research and Engineering
Information Office Library Branch
The Pentagon
Washington, D.C. 20301

U. S. Army Research Office 1 copy
Box CM, Duke Station
Durham, NC 27706

Defense Documentation Center 12 copies
Cameron Station
Alexandria, VA 22314

Defender Information Analysis Center 1 copy
Battelle Memorial Institute
505 King Avenue
Columbus, OH 43201

Air Force Office of Scientific Research 1 copy
Department of the Air Force
Washington, D.C. 22209

Office of Naval Research Branch Office 1 copy
ATTN: Dr. Robert Behringer
1030 East Green Street
Pasadena, CA 91106

Defense Advanced Research Projects Agency 1 copy
ATTN: Strategic Technology Office
1400 Wilson Blvd.
Arlington, VA 22209

Office Director of Defense 1 copy
Research and Engineering
ATTN: Assistant Director
(Space and Advanced Systems)
The Pentagon
Washington, D.C. 20301

Office of the Assistant Secretary of Defense 1 copy
ATTN: Mr. Gerald R. McNichols
System Analysis (Strategic Programs)
Washington, D.C. 20301

National Aeronautics and Space Administration 1 copy
Marshall Space Flight Center
ATTN: Mr. Lee Jones EP24
Marshall Space Flight Center, AL 35812

National Aeronautics and Space Administration 1 copy
Code RR, FOB 10B
600 Independence Ave., SW
Washington, D.C. 20546

National Aeronautics and Space Administration 1 copy
Ames Research Center
ATTN: Dr. Kenneth W. Billman
Moffett Field, CA 94035

U. S. Army Missile Command 2 copies
Research and Development Division
ATTN: Army High Energy Laser Programs
Redstone Arsenal, ALA 35809

Director
Ballistic Missile Defense Advanced Technology Center
P.O. Box 1500
Huntsville, AL 35807
ATTN: ATC-O 1 copy
 1 copy
ACT-T

Department of the Navy 1 copy
Office of the Chief of Naval Operations
ATTN: (OP 982F3)
The Pentagon 5C739
Washington, D.C. 20350

Office of Naval Research Branch Office 1 copy
ATTN: Dr. Fred Quelle
495 Summer Street
Boston, MA 02210

High Energy Laser Project Office 1 copy
Department of the Navy
Naval Sea Systems Command
ATTN: CAPT A. Skolnick, USN (PM 22)
Washington, D.C. 20360

Navy Radiation Technology 1 copy
Air Force Weapons Laboratory (NLO)
Kirtland AFB, NM 87117

Naval Surface Weapons Center 1 copy
ATTN: Dr. Leon H. Schindel (Code 310)
White Oak
Silver Spring, MD 20910

U. S. Naval Weapons Center 1 copy
ATTN: Technical Library
China Lake, CA 93555

Department of the Air Force 1 copy
Air Force Materials Laboratory (AFSC)
ATTN: MAJ Paul Elder (LPS)
Laser Window Group
Wright Patterson AFB, OH 45433